University of Stavanger

FACULTY OF SCIENCE AND TECHNOLOHY

MASTER'S THESIS

Study program / Specialization:	Spring semester, 2021
MSc. in Petroleum Engineering / Natural gas engineering	Open

Author:	*A. Abaza*
Ahmed Abaza	.... (Author signature)

Supervisor:	Prof. Zhixin Yu

Master thesis title:	Direct air capture of CO_2 by adsorption on zeolites

Credits: 30 ECTS

Keywords: Direct air capture, zeolite 13X, packed beds, column efficiency, Thomas model, breakthrough curve fitting, mass transfer zone, sensitivity of pressure drop.	Number of pages: 82 Stavanger, 15.06.2021

Acknowledgements

Throughout the writing of this dissertation, I have received a great deal of support and assistance.

Foremost, I wish to express my sincere appreciation to my supervisor and mentor, Professor Zhixin Yu, whose expertise was a milestone in the completion of this project. He convincingly guided and encouraged me to be professional and to do the right thing even when the road got tough. Without his persistent help, the goal of this project would not have been realized. I am so grateful to you Professor for your tremendous guidance.

The physical and technical contribution of Green-Cap solutions company is truly appreciated. This project could not have reached its goal, without their support and funding. I am gratefully indebted to all the employees there, for the continuous guidance and valuable comments during the experimental work.

Finally, my deep and sincere gratitude to my family for their continuous and unparalleled love, help and support. I am grateful to my older brothers for always pushing me to be better and excel at the highest of my abilities. I am forever indebted to my parents for giving me the opportunities and experiences that have made who I am. They selflessly encouraged me to explore new directions in life and seek my own destiny. This journey would not have been possible if not for them. I dedicate this dissertation to you, Mom and Dad.

Abstract

Greenhouse gases have become a consequential global issue. Carbon dioxide (CO_2) is the most abundant greenhouse gas, that is significantly contributing to disastrous changes in the global climate. The escalating levels of carbon dioxide emissions in atmosphere have incited the implementation of breakthrough technologies to lessen its impact on the atmosphere.

In this work, CO_2 capture from the atmosphere (i.e., direct air capture) was studied and investigated by using three commercial adsorbents of the zeolite type 13X (MSC-544, MSC-542, and SP-564), with average particle diameter of 0.00205, 0.00375, and 0.006 m, respectively. The breakthrough behavior was predicted as a function of the flowrate by keeping both inlet concentration and the temperature constant at 400 ppm and 19℃, respectively and operating at atmospheric pressure. The flowrates investigated were, 25.3, 31.6, and 38 m^3/hr, which were equivalent to superficial velocities of 0.2, 0.25, and 0.3 m/sec, respectively.

The breakpoint time reduced significantly with increased flowrate. The longest breakpoint observed was 11.6 hrs for MSC-544 at the flowrate of 25.3 m^3/hr. whilst the shortest breakpoint time was 3.5 hrs for SP-564 at a flowrate of 38 m^3/hr. The adsorption capacity increased relatively with lowering the flowrate. However, the percentage of increase in the adsorption capacity was not of great significance, based on the operating flowrates employed in the project. The highest adsorption capacity of (31.5 g CO_2/Kg adsorbent) was observed for MSC-544 at the flowrate of 25.3 m^3/hr. In this case, it has the smallest width of mass transfer zone of 0.045 m, and the highest column efficiency of 87.81%, which indicates efficient utilization of the bed capacity.

Optimizing the bed capacity by varying the flowrate during the same experimental run was found to be highly effective in terms of reducing the adsorption time. By employing that strategy, the time saved for MSC-544, MSC-542, and SP-564 was 1.00, 1.26, and 1.7, hrs respectively.

Thomas model was used to fit the experimental breakthrough curves by using linear and nonlinear regression analysis. Both models performed well in predicting the adsorption capacity. However, the nonlinear method was more effective in predicting the behavior of the breakthrough curve, with R^2 higher than 0.99.

It was observed that the pressure drop was highly sensitive to slight variations in the estimation of the void fraction. large deviations between the measured and the predicted pressure drop values was observed remarkably due to inaccurate estimation of the void fraction of the given adsorbents. 1% error in the estimation of the void fraction causes error of 5.15%, 4.33%, and 4.88% in the predicted pressure drop of MSC-544, MS-542, and SP-564, respectively. The effect of decreasing the particle diameter was of more significance than the effect of increasing the flowrate on the pressure drop. The highest pressure drop measured was 0.445 KPa for MSC-544 at a flowrate of 38 m^3/hr. While the lowest pressure drop was 0.054 KPa for SP-564 at a flowrate of 25.3 m^3/hr.

Acronyms & Abbreviations

DAC   Direct air capture

GHGS   Greenhouse gases

FOLU   Forestry and other land use

CO₂   Carbon dioxide

CCS   Carbon capture and sequestration

CCU   Carbon capture and utilization

MOFS   Metal organic frameworks

MTZ   Mass transfer zone

TSA   Temperature swing adsorption

PSA   Pressure swing adsorption

VSA   Vacuum swing adsorption

PLC   Programmable logic controller

FIC   Flowrate indicator controller

PIT   Pressure indicator transmitter

TIT   Temperature indicator transmitter

AIT   Analyzer indicator transmitter

PCV   Pressure control valve

SAE   Sum of the absolute errors

SSE   Sum of the squares of errors

SRS   Sum of the relative squares of errors

Table of Contents

Table of Figures

List of Tables

1   Introduction

During the last decades, direct air capture (DAC) has a gained a lot of interest and aroused many commentaries and analyses. There have been many discussions and debates about the benefits and necessity of applying DAC as a viable option for climate change mitigation. Now, DAC is growing rapidly as environmental technology that imposes itself to be an effective solution for decreasing the emissions. An increasing number of academics are shifting their attention and conducting research to develop materials and processes applicable for this technology. Many start-up companies are attempting seriously to push this technology from the lab scale to the pilot or commercial scale. **Green-Cap Solutions** company managed during the last two years to develop and optimize this process. The process efficiency is increased by 50% reduction in energy consumption, using smart energy distribution with the aid of heat pump technology, and 0% use of fossil fuel or chemicals. Recently, a significant amount of research and scientific work about capturing the carbon dioxide (CO_2) by adsorption on zeolites has been performed in order to accomplish an effective, economic approach to implement such a process. However, before going through the technicality of the process in detail, the reasons for the necessity of capturing the carbon dioxide and its implications on the environment will be highlighted. Unequivocally, it is a threatening issue to our life.

1.1   Climate change and the implications of GHG on the atmosphere

It is not a secret that nowadays, the main concern of the whole world has been directed to combat the climate change (global warming). Since the early beginnings of the industrial revolution in the 19th century, the exhaust gases due to burning of fossil fuels (oil, natural gas, coal, etc.), along with some industrial processes such as: cement & steel production, beside deforestation, have contributed to unprecedented concentrations of greenhouse gases (GHG) in the atmosphere. These ultimately will cause an increase in the earth's temperature, that is well known as greenhouse gas effect. The main greenhouse gases are: carbon dioxide, methane, nitrous oxides and fluorinated gases. [1]

Greenhouse effect is a natural process that warms up the earth's surface. It is mostly due to the interactions of the solar energy with greenhouse gases contained in the earth's atmosphere, as illustrated in Figure 1.1. When the solar energy reaches the earth's surface, some of this energy is reflected back to the space while the other is absorbed and picked by the greenhouse gases and reradiated again to the earth. [2]

CO_2 is the major constituent of the greenhouse gases. It is made up of carbon atom attached to oxygen atom from each side. As the atoms are tightly bounded to each other, the carbon dioxide molecule can absorb infrared radiation (IR) and that will cause the vibration of the whole molecule. Consequently, the vibrating molecule will emit the radiation again which is most likely to be absorbed by another greenhouse gas molecule. This absorption-emission-

loop will serve as insulation for the earth's surface from the outer cold space. In some texts, the GHG are described as a blanket that grip the infrared radiation and preventing it from passing to the outer space. Therefore, the result is continuous warming up the earth's atmosphere surface[3].
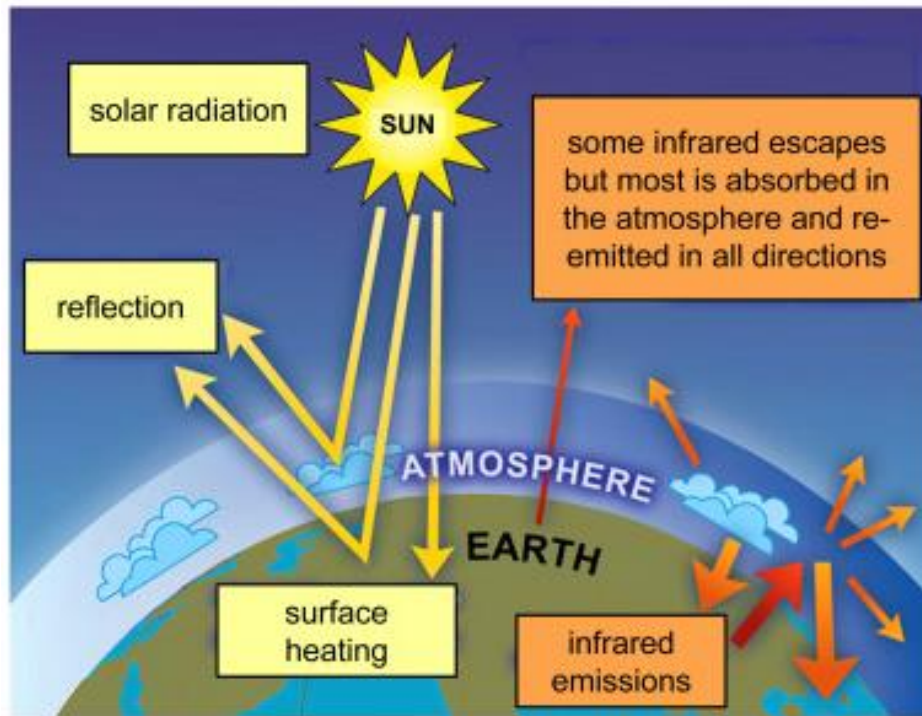
Figure 1.1 Illustration of the greenhouse effect [4]

The extensive increase of the CO_2 emissions into the atmosphere has disastrous implications on the environment. As it would result in increasing the sea levels and changing the pattern of the environment due to the expanse of the desert regions. Moreover, it would lead to changes in the production of the agriculture crops, glacier retreat, extinction of some species and spread of diseases. It is also important to consider, that increase in the global temperature is accompanied by changes in weather conditions such as severe heat waves and changes in the rainfall, resulting in more floods or droughts. [5]

1.2 Total CO_2 and other GHG emissions in the atmosphere

Obviously, it can be observed from Figure 1.2 that CO_2 is the main contributor of the greenhouse gases. CO_2 emissions from fossil fuel combustion and industrial processes contributed to about 78% increase in the total GHG emission during the periods from 1970 to 2010, and from 2000 to 2010. Also, it is depicted in the graph, that the CO_2 emissions from fossil fuel combustion is much higher than that from Forestry and other land use (FOLU). As a conclusion, CO_2 remains the major anthropogenic GHG among the other non-CO_2 gases of the total GHG emissions.[6] [7]
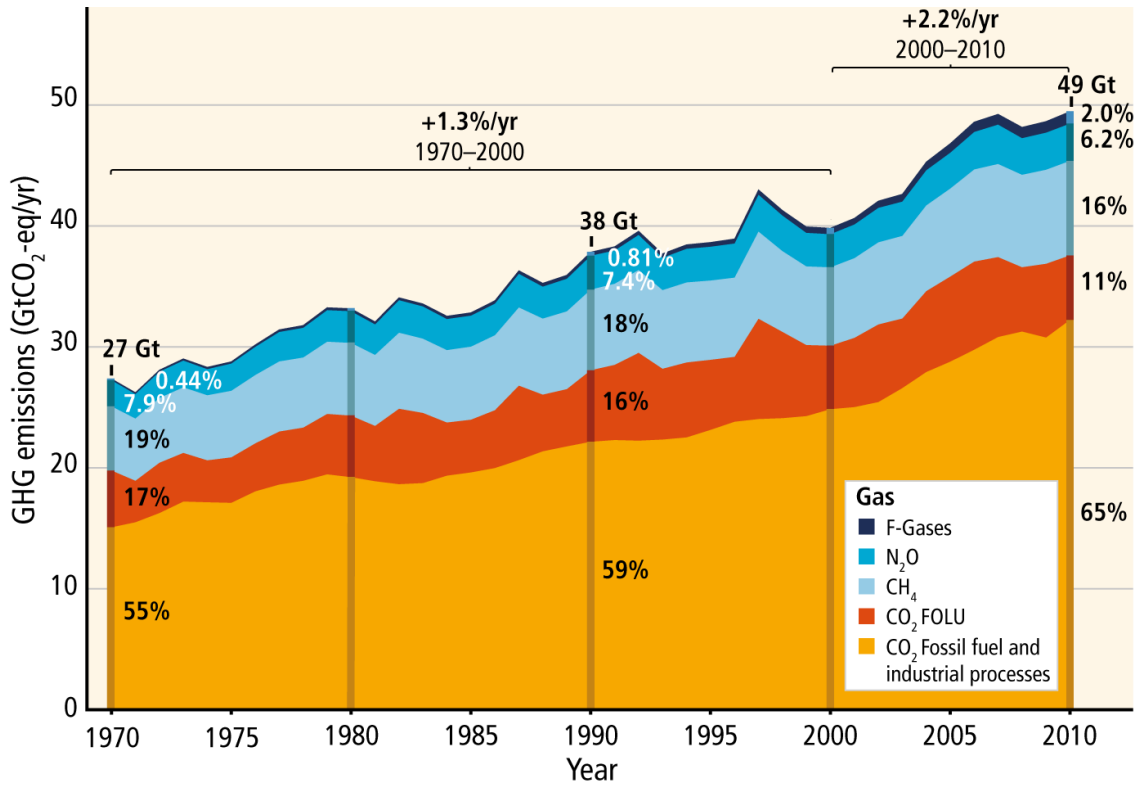
Figure 1.2 Total annual anthropogenic GHG emissions (GtCO₂eq/yr) by groups of gases 1970–2010 [6]

1.3   Carbon management and GHG mitigation pathways

As discussed in the previous sections, the human activities and the rapid industrial development have boosted the concentration of CO_2 in the atmosphere and increased the average global temperature significantly. Concerns over the climate change have triggered the alarm towards mitigating the increased emissions in the atmosphere. As a result, global warming has become as a global agenda that lead to growing scientific, economic, and political debates related to the CO_2 management. In order to implement a sustainable carbon management plan, some general and experimental aspects have to be considered such as: (a) reducing the emissions, (b) recycling the CO_2 and the possibility of storing and reuse it, (c) making our technologies more efficient by switching towards low carbon containing fuels, (d) utilize the captured CO_2 into valuable products that causes a net reduction in the total amount of CO_2 in the atmosphere [8].

Figure 1.3 shows the different approaches for CO_2 mitigation. Generally, the captured CO_2 from large point sources is transported, then it is either stored or utilized as will be discussed in the next two sections.

3
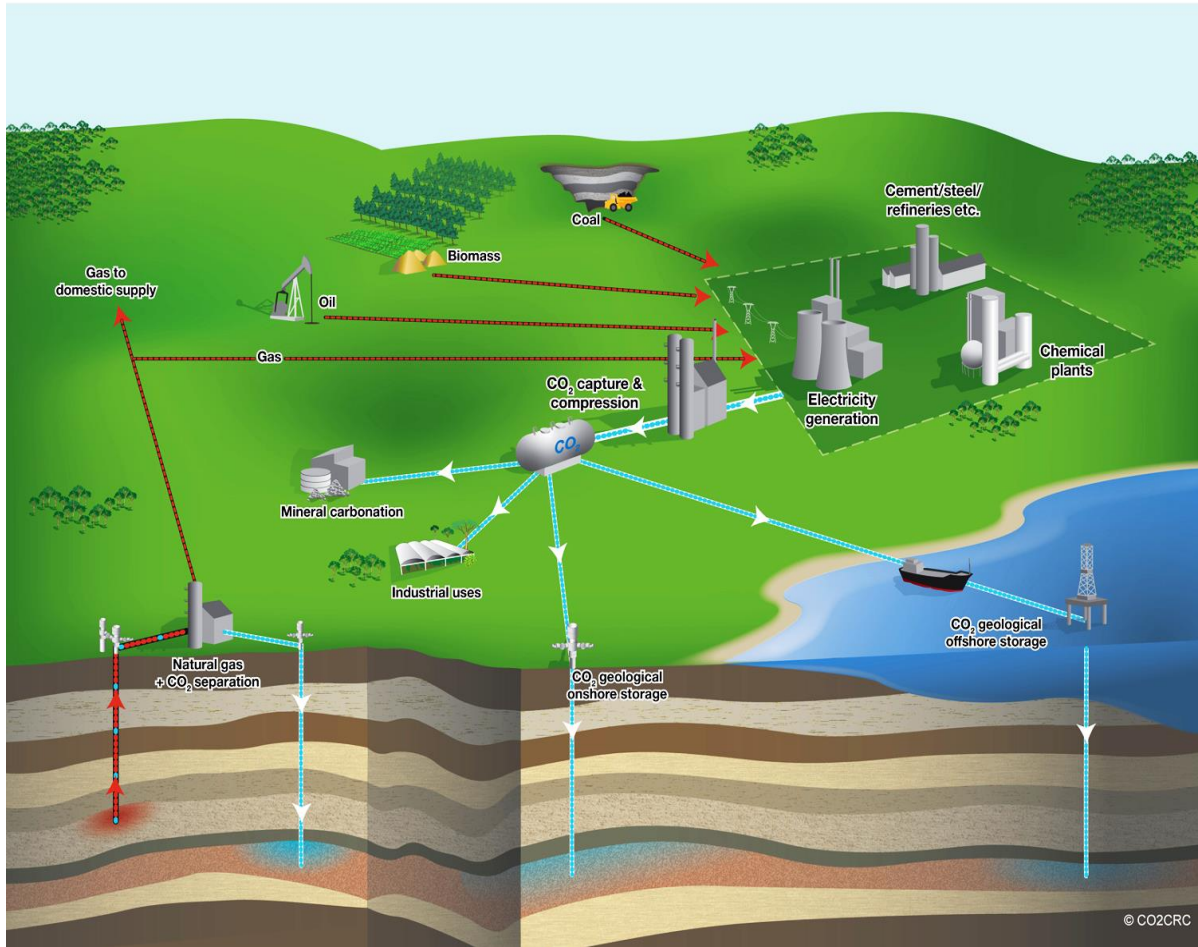
Figure 1.3 Carbon dioxide mitigation (source CO₂CRC)

1.3.1 Carbon Capture and Storage (CCS)

Carbon capture and storage imposes itself strongly as a technical solution, that is capable of reducing the global emissions of GHG to the atmosphere. The term CCS is often used for capturing the CO_2 released from large point sources such as burning of fossil fuels in power generation plants. CCS involves three main steps as follow: [9]

  I.   Capturing the CO_2 released from the exhaust gases produced by the combustion of fossil fuel in power generation plants or from other chemical industries. This could be achieved by different approaches such as: cryogenic distillation, membrane purification, absorption in liquids or adsorption on solid sorbents.
 II.   The captured CO_2 is pressurized to 100 bar or even more, then transported through pipelines to the geological storage site.
III.   Eventually, the captured CO_2 is injected into stable geological storage and trapped for long term storage, to prevent its subsequent emission into the atmosphere.

1.3.2 Carbon Capture and Utilization (CCU)

Carbon capture and utilization follows the same path of CCS. However, CCU not only seeks for limiting the volume of emissions in the atmosphere, but it also takes the advantage of using the captured CO_2 into various industrial process and valuable products such as: biofuel production, synthetic fuels, mineral carbonation, polymers synthesis, dry cleaning, food industry and other diverse uses (Figure 1.4). In other words, it makes the carbon capture project more profitable and economic. [10]

For instance, in Norway, Yara company produces more than 200000 tons/annum of CO_2 for use in the food grade industry from their ammonia production, which seems to be promising operation towards efficient utilization of CO_2 and decreasing the emissions.[11]
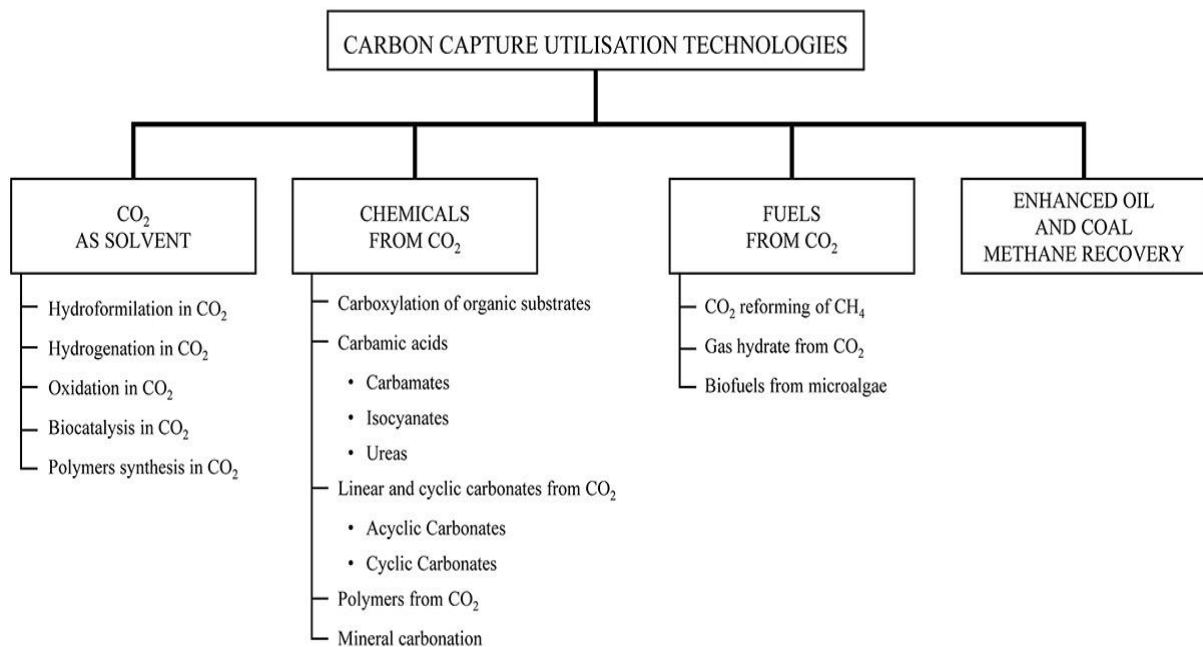
Figure 1.4 Carbon capture utilization technologies [10]

1.4 Aim of the thesis

Capturing CO_2 directly from air by adsorption on zeolites sounds to be a promising and novel technology. This shall be done by flowing air stream that contains CO_2 over a packed bed of zeolite beads. The CO_2 will diffuse into the zeolite pores and selectively attach to the active sites within the pores. The CO_2 will be initially captured at the bed inlet. As the capture process progresses, the zeolite beads near the packed bed inlet will be saturated with CO_2 and the adsorption process will progress further into the bed, till the entire bed comes to equilibrium with the incoming air feed.

The scope of the study is to investigate the effect of varying the inlet flowrate of air (i.e., superficial velocity) to the packed bed of zeolites on the breakthrough curve. That will provide information about the adsorbent CO_2 storage capacity and the rate of CO_2 uptake. Those are crucial information for the design of CO_2 capture processes using adsorption.

This shall be implemented by keeping both the inlet air temperature and concentration constant at 19℃ and 400 ppm, respectively and operating at atmospheric pressure. The air flowrates shall be tentatively at 25.3, 31.6, and 38 m³/hr, which are equivalent to superficial velocities of 0.2, 0.25, and 0.3 m/s, respectively. Three different commercial adsorbents of the zeolite type 13X will be investigated. The adsorbents are MSC-544, MSC-542, and SP-564. The same procedures will be carried out for each sorbent.

The following evaluations shall be made:

I. Studying the effect of varying the inlet flowrate on the shape and the behavior of the breakthrough curves, by evaluating the saturation capacity (loading) of the adsorbent, the length of the mass transfer zone, and the length of the unused portion of the bed. That will give an indication about the bed removal efficiency based on the fraction of the bed capacity that is efficiently utilized.

II. The obtained experimental breakthrough data shall be compared and verified by one of the well-known adsorption models used for predicting the behavior of fixed packed beds, in order to check the validity of the experimental data and to verify the kinetics of the adsorption process. That will be done by means of regression analysis.

III. Assessment and discussion of the pressure drop over the packed bed, and comparison of the measured pressure drop values with known theoretical models or equations.

IV. Discussion of the capture process and improvements that could be implemented for the capture facility, in order to enhance the process efficiency based on the observations and results obtained during the experimental work.

2   Literature Review

In the introduction, we described both background and the motivation for capturing the CO_2. We shall now proceed to go through the theoretical basis and the technicality related to CO_2 capture. At the beginning we will give a brief overview about the different approaches to capture CO_2 from large source point (i.e., exhaust gases from burning fossil fuel). Then we will focus on the state of art of the thesis which is direct air capture by adsorption on zeolites. We will try to cover, as much as possible, different aspects related to the adsorption process in packed beds by elaborating the physics behind the adsorption process, mass transfer between the bulk and solid phases, difference between chemisorption and physisorption, different adsorbents used for capturing the CO_2, characteristics of zeolites, adsorption isotherms, isosteric heat of adsorption, pressure drop in packed bed, and the design of fixed packed bed columns.

2.1 CO_2 Capture technologies from large source point

The CO_2 released from the combustion processes of fossil fuel from power plants and the nature of the combustion process itself play an important role in determining the appropriate capture technology. The selection is based on the advantages and disadvantages of each process as illustrated in Table 2.1. Generally, the capture technologies represent around 70-80 % of the total cost of full CCS project. Therefore, care must be taken when choosing the appropriate technology to enhance the economy of the project. Essentially, there are three main capture systems for removal of CO_2 released from combustion processes, as shown in Figure 2.1 : (a) Post-combustion (b) Pre-combustion (c) Oxy-fuel combustion.[12]
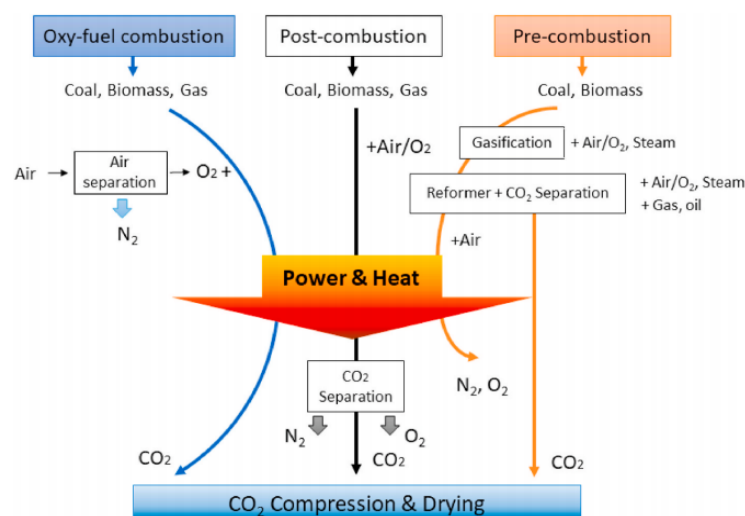
Figure 2.1 Different capture technologies of CO2 from burning of fossil fuel [13]

7

2.1.1 Post-Combustion Capture

Post - combustion capture refers to capturing the CO_2 released from the exhaust gases due to the combustion of fossil fuels in power plants. It is always described as a preferred option for retrofitting existing power plant [14]. However, the main challenge in post-combustion is the energy penalty and associated costs for the capture facility. As the CO_2 concentration is relatively low in the flue gases, which makes the separation process for CO_2 is more complicated to reach higher percentage of purification. [15].

2.1.2 Pre-Post Combustion Capture

Pre-Post combustion process refers to capturing the carbon dioxide as undesired product from a reaction or conversion process. For instance, burning of coal in power plants requires a gasification process prior to burning. Another example is the CO_2 produced with hydrogen during steam reforming in the ammonia synthesis process. In comparison to post-combustion, we can conclude that the high CO_2 concentration in the pre-post facilitates the CO_2 separation.[15] [16]

2.1.3 Oxyfuel Combustion

As the name would suggest, in oxyfuel combustion the fuel is burned with a pure oxygen instead of air. Consequently, that will increase the concentration of the carbon dioxide and reduces the amount of nitrogen present in the flue gases and makes the separation process easier compared to both post and pre-post combustion. Moreover, the reduction in NO_x emissions is another advantage. Using such a process seems to be efficient as the major constituent of the flue gases is CO_2, with concentration around 80-90%. However, the cost of the process will be increased due the consumption of large amounts of oxygen which requires cryogenic separation of air.[17] [18]

Table 2.1 Advantages & disadvantages of different CO_2 capture technologies [12]

Capture process	Application area	Advantages	Disadvantages
Post-combustion	Coal-fired and gas-fired plants	Technology more mature than other alternatives; can easily retrofit into existing plants;	Low CO_2 concentration affects the capture efficiency;
Pre-combustion	Coal-gasification plants	High CO_2 concentration enhance sorption efficiency; fully developed technology, commercially deployed at the required scale in some industrial sectors; opportunity for retrofit to existing plant;	Temperature associated heat transfer problem and efficiency decay issues associated with the use of hydrogen-rich gas turbine fuel; high parasitic power requirement for sorbent regeneration; inadequate experience due to few gasification plants currently operated in the market; high capital and operating costs for current sorption systems;
Oxyfuel combustion	Coal-fired and gas-fired plants	Very high CO_2 concentration that enhances absorption efficiency; mature air separation technologies available; reduced volume of gas to be treated, hence required smaller boiler and other equipment;	High efficiency drop and energy penalty; cryogenic O_2 production is costly; corrosion problem may arise;
Chemical looping combustion	Coal-gasification plants	CO_2 is the main combustion product, which remains unmixed with N_2, thus avoiding energy intensive air separation;	Process is still under development and inadequate large scale operation experience;

2.2   Direct Air Capture

Direct air capture (DAC) is a concept that was first introduced to mitigate the emissions and global warming by Lackner in 1999 [19]. It seems to be controversial technology and arouses the question whether it is effective and viable alternative for decreasing the greenhouse gas emissions. The main difference between DAC and other conventional CO_2 capture technologies mentioned in section 2.1, is that DAC processes capture the carbon dioxide from ambient air nearly at a concentration of 400 ppm which is roughly 350 times lower than that from the coal-based flue gas.[20]

2.2.1   Advantages of Direct Air Capture

The advantages of DAC can be briefly summarized as follow: [21]

   I.   The predominant advantage of DAC technology is that it has the potential to address emissions from distributed sources as well as point sources.
   II.   Moreover, DAC processes are not location-specific, allowing capture facilities to be set up anywhere. Furthermore, the processes do not have to deal with the high concentrations of contaminants in flue gas (SO_x, NO_x, mercury, etc.), which lead to degradation in performance of the sorbents used in flue gas capture processes.
   III.   DAC is supposed to extract CO_2 from the atmosphere while flue gas capture is meant to purify CO_2 from an exhaust gas mixture.

2.2.2   DAC through sorbent-based processes

Generally, DAC is based on technologies that employ reversible sorbents either in the form of solution (i.e., absorption) or solid materials (i.e., adsorption), in order to regenerate the spent sorbent used for CO_2 capture. Various sorbent materials are known for their ability to capture the CO_2 from air [22] [23]. However, it is logical to elaborate the main features should be existed in those sorbents for CO_2 capture. The characteristics of the sorbent materials can be summarized as follow: [24]

   I.   High selectivity to the CO_2 compared to other gases present in air [25] [26].
   II.   High CO_2 loading or capacity to make the process efficient [27].
   III.   Stable under the presence of moisture which is one of the main challenges in DAC processes [28].
   IV.   Since the DAC process is normally carried out close to room temperature, the sorbent material should have fast kinetics at ambient conditions (high sorption rate) [29].
   V.   In order to utilize the captured CO_2 and to regenerate the sorbent material, it should not bind CO_2 strongly, otherwise the energy requirement for regeneration will be very high and the process will not be economically feasible [30].

2.2.2.1 DAC processes through aqueous solutions (Absorption)

One of the most common processes for capturing the CO_2 through absorption in caustic solutions is, the Kraft process (Fig. 2.2). The high binding energy between CO_2 and the caustic solutions gives a high loading for those solutions. However, the main disadvantage is the energy cost penalty required for regeneration through the calcination process (calciner). The CO_2 is captured by an aqueous solution of sodium hydroxide (NaOH) to give a highly soluble solution of sodium carbonate (Na_2CO_3) through exothermic reaction (absorber). In order to regenerate the sodium hydroxide, the Na_2CO_3 solution is precipitated in the precipitator through the reaction with calcium hydroxide ($Ca(OH)_2$) to give sodium hydroxide and calcium carbonate ($CaCO_3$), as depicted in the chemical reactions below. Then, the calcium carbonate is decomposed into quick lime (CaO) and CO_2 through highly endothermic process at temperature > 800℃ in order to utilize the captured CO_2.[31]
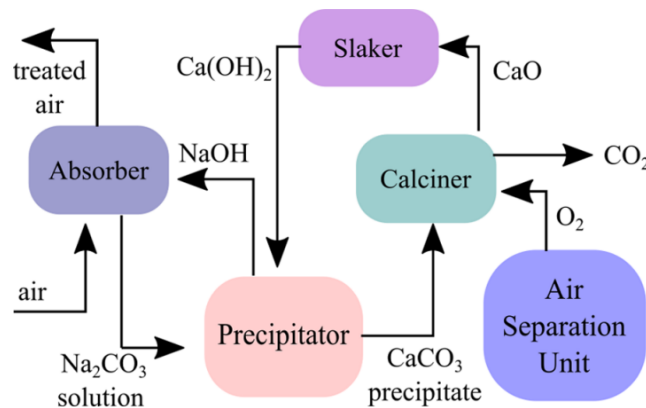
Figure 2.2 DAC through Kraft process [31]

<u>Absorber</u>: $2NaOH + CO_2 \rightarrow Na_2CO_3 + H_2O$ $\qquad$ ΔH° = -109.4 kJ/mol

<u>Precipitator</u>: $Na_2CO_3 + Ca(OH)_2 \rightarrow 2NaOH + CaCO_3$ $\qquad$ ΔH° = -5.3 KJ/mol

<u>Calciner</u>: $CaCO_3 \rightarrow CaO + CO_2$ $\qquad$ ΔH° = +179.2 KJ/mol

<u>Slaker</u>: $CaO + H_2O \rightarrow Ca(OH)_2$ $\qquad$ ΔH° = -64.5 KJ/mol
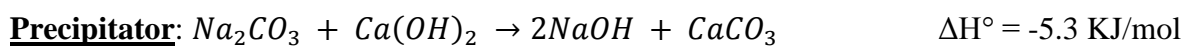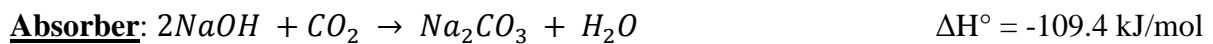
2.2.2.2 DAC through solid sorbents (Adsorption)

Various solid sorbents have been reported in the literature for their capability of capturing CO_2 from air [32] [33] [34] [35]. Generally, the solid sorbents are either classified as physical adsorbents such as zeolites, activated carbon and MOFs, or chemical adsorbents such as solid amines-based adsorbents. We will focus mainly on the physical adsorbents which are employed in this project, more specifically, zeolites. However, it is important to elaborate the main differences between physical adsorption (Van Der Waals forces) and chemical adsorption (chemical bond) to have better understanding of the different adsorption processes and how they work, as shown in the Table 2.2.

Table 2.2 Comparison between physical and chemical adsorption [36]

Physical Adsorption	Chemisorption
Low heat of adsorption ($<$2 or 3 times latent heat of evaporation.)	High heat of adsorption ($>$ 2 or 3 times latent heat of evaporation.)
Non specific	Highly specific
Monolayer or multilayer	Monolayer only
No dissociation of adsorbed species	May involve dissociation
Only significant at relatively low temperatures	Possible over a wide range of temperature
Rapid, non-activated, reversible	Activated, may be slow and irreversible
No electron transfer although polarization of sorbate may occur	Electron transfer leading to bond formation between sorbate and surface

2.3   Physisorbents used in DAC processes

As mentioned in the previous section that the physical adsorbents used for capturing the CO_2 are mainly zeolites, activated carbons and MOFs. Those candidates seem to be promising and effective due to their low cost, high surface area per unit mass of adsorbent, high porosity, high thermal stability and their ease of regeneration [37]. Basically, physical adsorption depends on Van der Waals forces and electrostatic interactions between the adsorbent and the adsorbate. Figure 2.3 depicts different adsorbents used for capturing CO_2 directly from air.
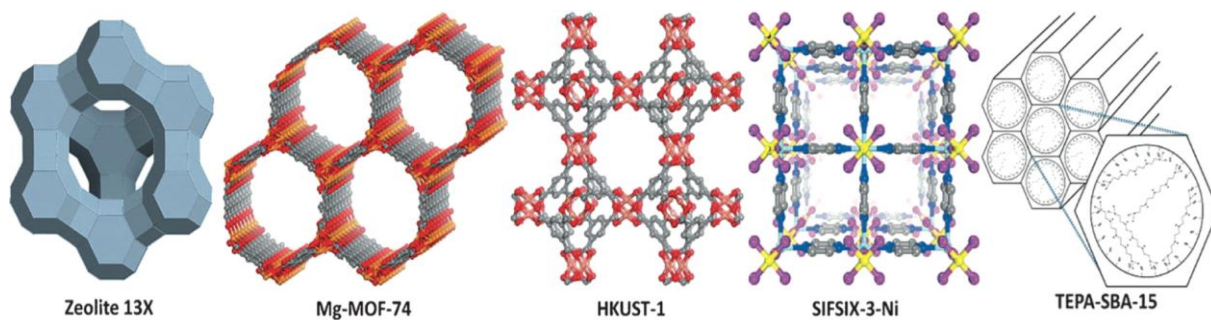
Figure 2.3 Range of physisorbents used in DAC processes [38]

2.3.1   Zeolites

Zeolite molecular sieves are crystalline, highly porous medium which belong to the family of aluminosilicates. Those crystals are characterized by three-dimensional pore system along with pores of defined diameter. Their framework is formed by tetrahedrons of SiO_4 and AlO_4 joined together in different regular arrangements through shared oxygen atoms, which are the basic building blocks of various zeolite structures. Due to the presence of alumina, zeolites exhibit a negatively charged framework which is balanced by positive cations such as (Na^+, K^+, Ca^{2+}, Mg^{2+}) that exist in the channels and cavities throughout the zeolite structure[39]. The adsorption properties of zeolites are strongly dependent on the size, charge density, and distribution of the cations in the porous structure [40].

The mechanism of CO_2 adsorption has been investigated by different groups of zeolites. It has been observed that the physical adsorption between the zeolites and the CO_2 takes place in a linear orientation by an ion-dipole interaction as explained by the following reaction: [41] [42].

$$(metal\ ion)^{x+} \dots \dots\ ^{\delta-}O = C = O^{\delta+}$$
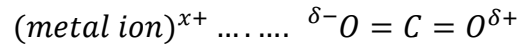
Adsorption of gases on zeolites mainly depends on three important parameters: structure and composition of the framework, cationic form, and zeolite purity [43]. Various types of zeolites which are highly crystalline with high specific surface area and have 3-D pore structure distribution have been investigated, such as: X, Y, A, β, ZSM, CHA [44] [45] [46]. The most common commercial types are type A and X, as illustrated in Figure 2.4.

For instance, the sodium form of zeolite A has a pore opening approximately 4Å which is denoted as zeolite 4A. If this sodium ion is replaced with larger potassium ion, a reduction in the pore size will happen and the pore size become approximately 3Å to give what is known as (3A molecular sieve). In case one calcium ion replaces two sodium ion, the pore size will increase to 5Å which is known as (5A molecular sieve) [47]. Moreover, the sodium form of the zeolite type X has pore size approximately 8Å which is known as 13X [48]. As a conclusion, the cations can be exchanged to adjust the pore size, where it allows passing of molecules smaller than the pore diameter and excluding the larger molecules. Hence, it got the name of molecular sieves.
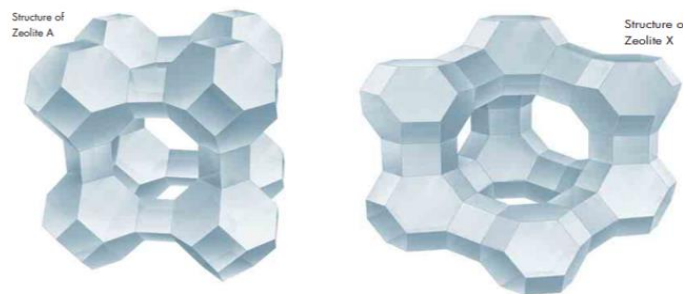
Figure 2.4 Structure of zeolite type A and X (source Grace Davison)

2.3.2 Activated Carbons

Activated carbons are one of the earliest examples of adsorbents used in adsorption processes. Owing to their low cost, high surface area, flexibility in modifying the pore structure, surface functionalization and their ease of regeneration. The naturally occurring carbonaceous materials seems to be promising for capturing the CO_2. In producing the activated carbons any carbonaceous materials such as wood, coal, coconut shells, could be used (Fig. 2.5). However, they should possess high carbon content, low ash content, as well as significant amounts of volatile components. Since the release of those volatile components during the thermal treatment will help in creating and tuning the pore structure [49].

The structure of the activated carbons is rather complex and composed of an amorphous structure and a graphite-like microcrystalline structure. The graphitic structure is basically important for determining the capacity. As it provides channels or space to accommodate the adsorptive molecules in the form of slit-shaped channel. The arrangement of the carbon atoms in the activated carbons is similar to that of pure graphite. It is composed of layers of condensed regular hexagonal rings held approximately 0.335 nm apart by Van der Waals forces, such that the carbon atoms in any plane lie above the centers of the hexagons. The distance between two adjacent carbon atoms in one layer is 0.142 nm. Due to the high level of structural imperfections in activated carbons, there are many possibilities for reactions with carbon atoms at the edges of the planar layers. As a consequence, oxygen-containing organic functional groups (Fig. 2.6), which are located mainly at the edges of broken graphitic ring systems, are present on the surface of the carbon [50].
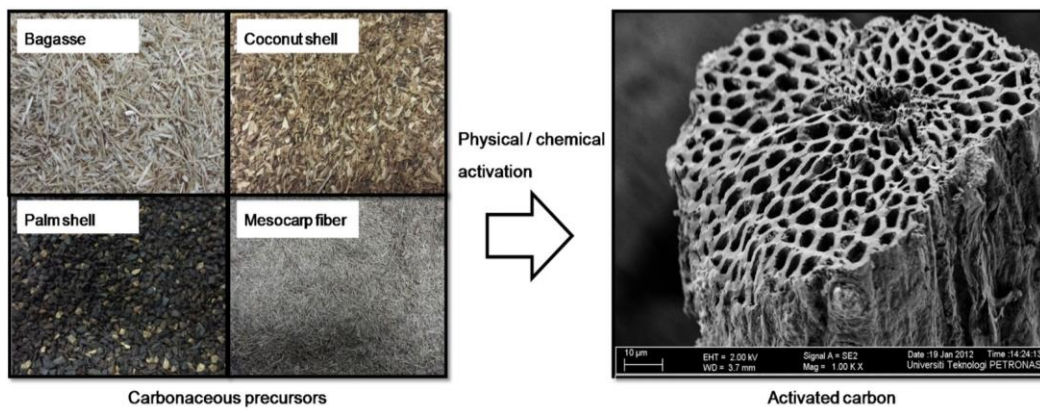
Figure 2.5 Different carbonaceous materials for activated carbons synthesis [51]

The chemical composition of the activated carbon surface is more complex than the pore structure. That depends on several factors such as, the source of the carbon and the method of activation either chemically or physically (Fig. 2.5). Generally, activated carbon is made of raw materials which are usually rich in oxygen and hence, many functional groups in activated carbon have oxygen atom. The oxygen functional groups can be classified as either acidic or basic groups. Therefore, the functional groups of an activated carbon can be increased by treating with oxidizing agents, or decreased by exposing the activated carbon to a vacuum at high temperatures. [52]
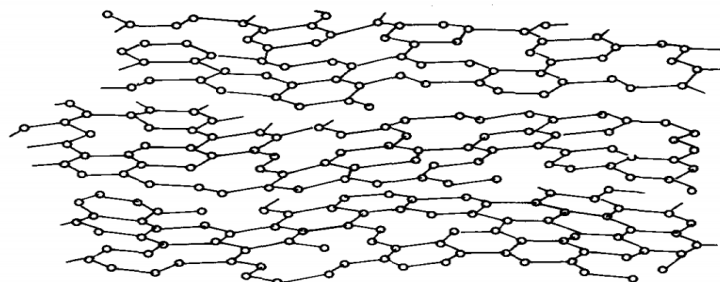
Figure 2.6 Schematic representation of the activated carbon structure, Oxygen-containing functional groups are located on the edges of broken graphitic ring systems [46]

13

2.3.3 Silica gel

One of the main desiccants used in DAC processes is silica gel. It is important to mention that silica gel has no selectivity towards CO_2 capture. Nevertheless, it is used for removing the water vapor from air prior to treating that the air with zeolites or any other CO_2 desiccants. As most of those desiccants show high selectivity towards the water vapor as well as the carbon dioxide, which consequently will reduce the adsorption capacity of the sorbents for capturing the CO_2. The co-adsorption of water vapor with CO_2 is one of the main challenges in CO_2 capturing processes from wet stream on solid desiccants which causes a reduction in the capacity or the loading of those desiccants.[53]

Silica gel ($SiO_2.xH_2O$) is a porous amorphous form of silica that is processed in the form of granules or beads. It is prepared from pure silica and contains chemically bounded traces of water (nearly about 5%). When it is overheated it loses the adsorbed water and consequently loses its capacity. Therefore, it is used at temperatures below 200°C. [54]

It has a unique internal structure and is available in various pore sizes with a specific surface area around 650 m^2/gm. The most two common commercial types used are: type (A) and type (B). Type (A) has pore size ranges from 2 nm to 3 nm, while type (B) ranges from 0.7 nm to 2 nm. Type (B) is used for high relative humidity above 50% as it has narrower pore sizes which means it has higher surface area and thus, will give high adsorption capacity. The heat of adsorption of water vapor on silica gel is mainly due to the condensation of water which is around 2800 KJ/Kg of adsorbate.[55] [56]. Also, some investigations have showed that many silica gel based composed materials have better performance than pure silica gel.[57]
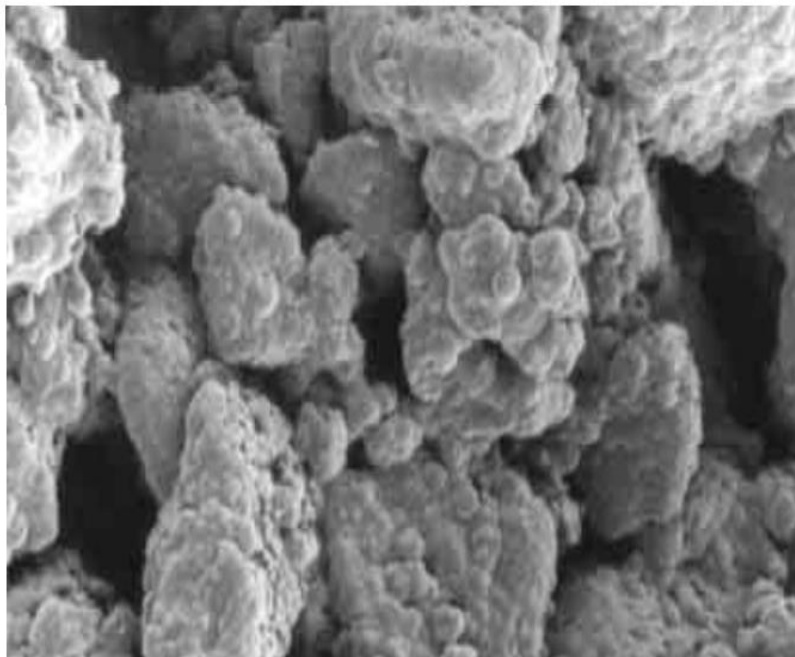
Figure 2.7 Silica gel particle (Scanning Electron Microscope picture) (source Grace Davison)

2.4 The basics of adsorption

As mentioned by many authors in the literature (Ponec [58], Ruthven [36], Duong [52]), adsorption is a surface phenomenon that takes place at the interface between two phases where cohesive forces including Van der Waals act between the molecules of the two phases (solid/fluid). Which is unlike absorption, in which the solute molecules diffuse and migrate from the bulk gas phase to the bulk liquid phase. During adsorption, the molecules diffuse from the bulk of the fluid (gas or liquid) to the surface of solid (adsorbent) that has affinity to specific molecules in the fluid phase (adsorbate). Most adsorbents are highly porous, where adsorption primarily occurs on the walls of the pores at specific active sites inside the particle. Since the pore size is generally very small, the adsorbent has internal surface area in the range of 500 to 1000 m^2/g. Separation of species occurs due to differences in molecular weight, shape, size, or polarity that makes specific molecules to be held more strongly on the surface than others. Bonding energies in physical adsorption range from 10 to 70 KJ/mol which is much lower than the energy of covalent bond. As mentioned earlier, the bonding energy should not be high enough in order to regenerate the adsorbent. Also, it shouldn't be low enough in order to have a good binding between the adsorbent surface and the adsorbate.[59]

2.4.1 Mass transfer in fixed bed adsorbers

For a specific species or molecule to be adsorbed, the molecule has to find its way to the adsorbent particle by convection. Then, it diffuses through the fluid film at the interface surrounding the particle and travel by diffusion along the length of the pore till it finds a vacant active site to be adsorbed, as depicted in Figure 2.8. Generally, in any transport process, the mass transfer steps are driven by departure from equilibrium [60].
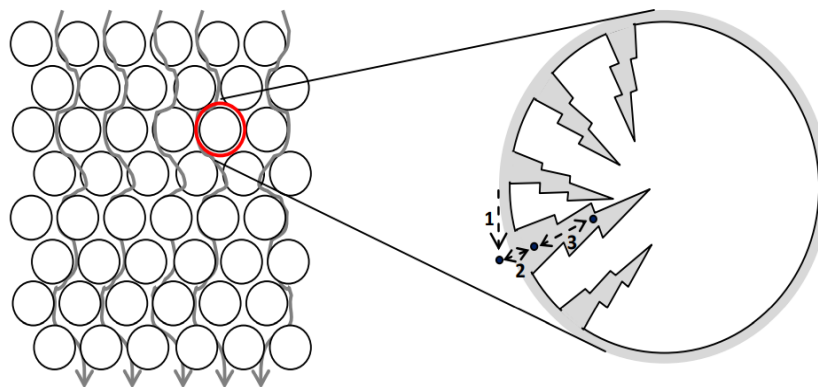
Figure 2.8 Schematic diagram of diffusion and mass transfer phenomena experienced by a molecule in a gas phase, while travelling in and out of the porous particle [61]

Equations for mass transfer in fixed-bed adsorption are based on making material mass balance of the adsorbate for a section dL of the bed as shown in Figure 2.9. The rate of accumulation in the fluid and in the solid phases is equal to difference between the input and output streams, with the assumption that the change in the superficial velocity is neglected. The material balance equation is given as Eq. 2.1: [60]

$$\varepsilon \, dL \, \frac{\partial c}{\partial t} + (1 - \varepsilon) \, dL \, \rho_p \, \frac{\partial W}{\partial t} = u_0 c \, - \, u_0(c + dc) \tag{2.1}$$

by grouping the terms of the right-hand side of Eq. 2.1, it can be written as follow:

$$\varepsilon \, \frac{\partial c}{\partial t} + \, (1 - \varepsilon) \, \rho_p \, \frac{\partial W}{\partial t} = \, -u_0 \, \frac{\partial c}{\partial L} \tag{2.2}$$

Where the term ε is the external void fraction of the bed, and solute dissolved in the pore fluid is included with the particle fraction $(1 - \varepsilon)$. For adsorption from a gas or dilute solutions, the first term in Eq. 2.2, which is the accumulation in the fluid phase $\left(i.e., \, \frac{\partial c}{\partial t} \right)$ is usually neglected compared to the accumulation in the solid phase $\left(i.e., \frac{\partial W}{\partial t} \right)$.

The mechanism of transfer to the solid by convection and diffusion is illustrated by Figure 2.9. It is important to take into consideration, that the physical adsorption process is practically instantaneous, and the equilibrium is assumed to occur between the surface and the fluid at each point inside the particle. Thus, the overall transfer process is given and approximated using an overall volumetric coefficient (K_c) and an overall driving force:

$$\rho_p \, (1 - \varepsilon) \, \frac{\partial W}{\partial t} = \, K_c \, a \, (c - c^*) \tag{2.3}$$

The mass transfer area (a) in the previous equation is taken as the external surface of the particles, which is approximately equals to $6(1 - \varepsilon)/D_p$ for spheres. The concentration c^* is the value in equilibrium with the average concentration W in the solid. (ρ_p) is the particle density. [60]
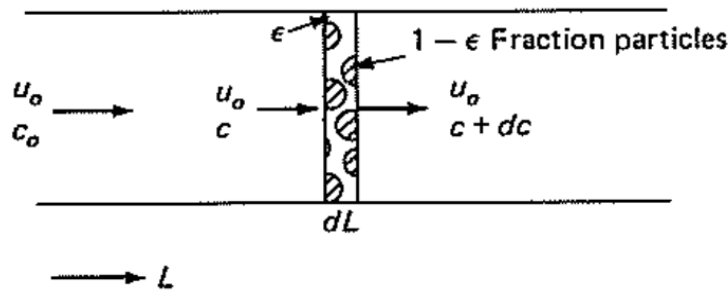
Figure 2.9 Mass balance for a section of a fixed bed [60]

A common industrial approach in adsorption processes, is to pass the fluid to be treated through a column packed with adsorbent., in order to allow transport from the fluid to the adsorbent to take place. The mechanism of mass transfer of such an operation is illustrated in Figure 2.10.

16

The figure shows the concentration profile along the length of fixed bed of a given adsorbent at four different times. By assuming the adsorbent is fresh (i.e., free from adsorbate) or fully regenerated, mass transfer occurs immediately once upon introduction of the incoming feed. That leads to a decrease in the concentration of adsorbate in the feed along the bed length till it becomes nearly zero. Continuously fresh feed enters the column, so that the portion of the bed which the feed contacts initially is continually exposed to the fluid at the feed concentration.[62]

Eventually, that part of the bed will become in equilibrium with the incoming feed (i.e., becomes fully saturated and cannot adsorb more) and no additional net mass transfer occurs. Therefore, the feed will move longer distance to encounter a new section of the bed that has not reached equilibrium with the feed. Mass transfer resumes and the fluid concentration starts to decrease again till it nearly reaches zero and so on. The length over which the concentration drops or changes is called mass transfer zone (MTZ). Consequently, as the process continues, the feed must travel farther and farther along the bed to encounter new sections that haven't reached equilibrium yet, and the mass transfer zone progresses along the bed until the entire bed becomes fully equilibrated and saturated with adsorbate.[63]
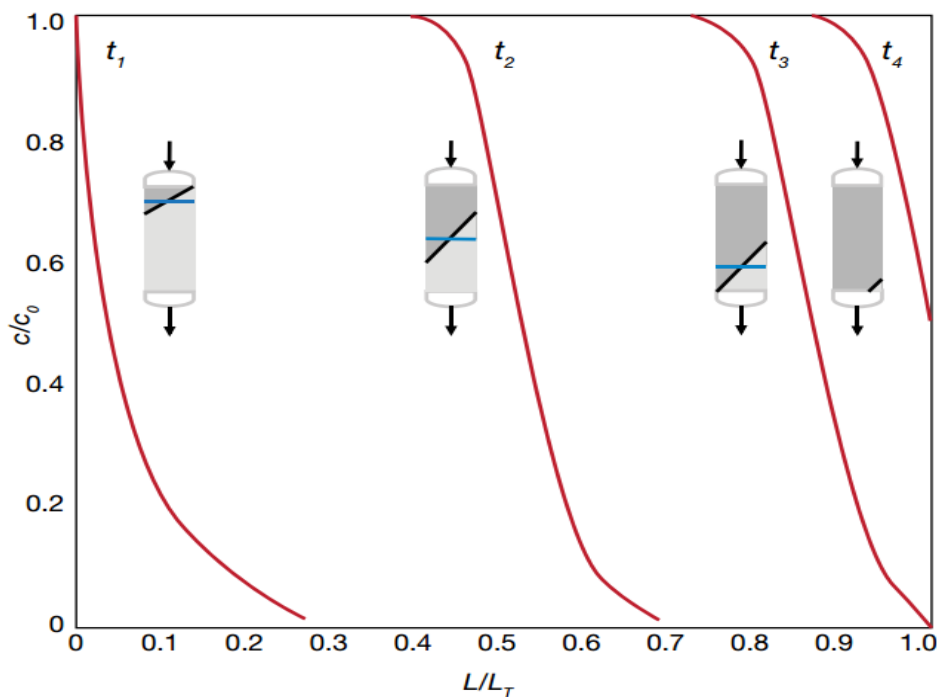
C = concentration of the adsorbate in the effluent.

C_0 = Concentration of the adsorbate in the incoming feed.

L = Length of the bed along the bed.

L_T = Total bed length.

t = Time.

Figure 2.10 Mass transfer zone progress along fixed bed of adsorbent [64]

17

2.4.2 Breakthrough curves

As discussed in the previous section, the mass transfer zone progresses along the bed length with time until some adsorbate starts to be detected in the stream exiting the column and the relative concentration (C/C_0) increases above zero at a given time. This time is referred to as breakthrough time. The concept is explained by breakthrough curve which is a plot between the adsorbate concentration in the effluent stream as a function of time [60] [65], as shown in Figure 2.11.
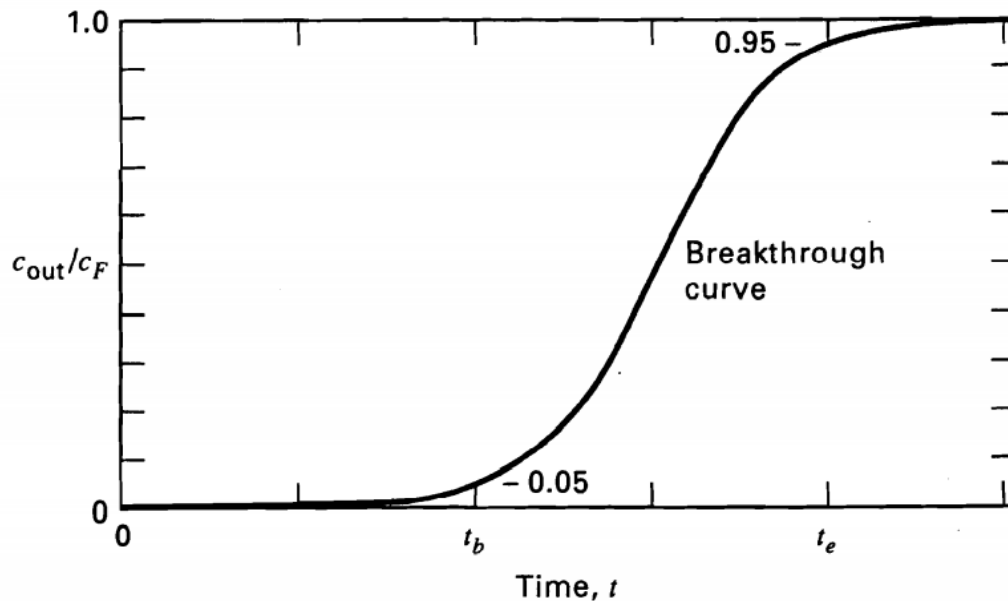
Figure 2.11 breakthrough curve in fixed bed adsorber [66]

2.4.3 Adsorption Equilibria

Adsorption equilibrium is the most important piece of information for understanding the adsorption process. It does not matter how many components are present in the system. The adsorption equilibrium of pure components is the main parameter that describes the affinity of those components to be accommodated or adsorbed by a specific solid sorbent. Hence, that will allow to study the adsorption kinetics of pure component as well as the adsorption kinetics of multicomponent system. If solid and fluid are placed in contact with each other for a period of time, a state of dynamic equilibrium will be established between the two phases, as illustrated by Figure 2.12. At equilibrium, the rate of adsorption of the fluid species onto to the solid equals to the rate of desorption from that surface.[67]
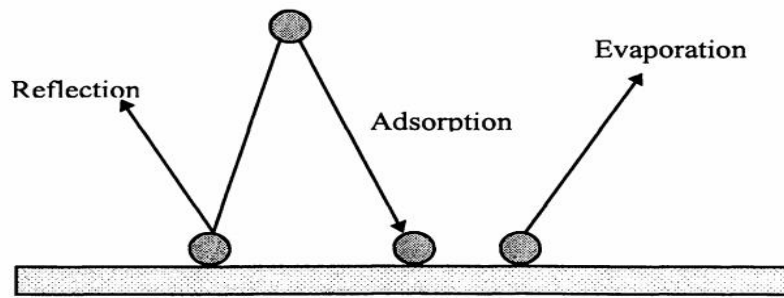
Figure 2.12 Schematic diagram of adsorption mechanism on a flat surface [52]

Equilibrium behavior is described by expressing the amount of adsorbate adsorbed on the adsorbent at equilibrium as a function of the partial pressure (in case of gases) or concentration (in case of liquids) at a constant temperature. Such an equilibrium model is well known as adsorption isotherm. This is a common approach in the branch of adsorption engineering. As shown in Figure 2.13, there are three types of isotherms. A favorable isotherm has a convex shape, which indicates a large capacity or loading for the adsorbent at low partial pressure. Conversely, unfavorable isotherm has a concave shape which means that a high relative pressure is required in order to achieve economic adsorption process. The last one is the irreversible isotherm, where the maximum adsorption capacity can be achieved practically at low partial pressure. However, this type of isotherms is favorable in terms of adsorption not for desorption or regeneration. As the energy requirement for desorption will be very high, and the regeneration process is practically so difficult. [60] [68]
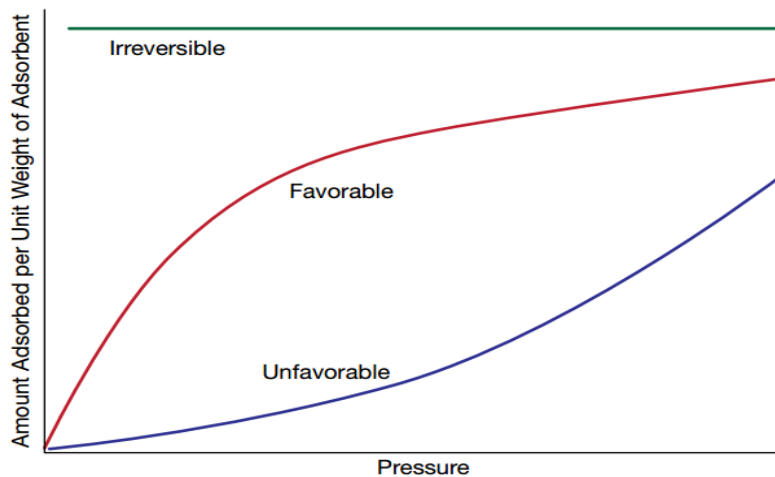
Figure 2.13 Different types of isotherms [64]

Many isotherm models have been proposed for describing the adsorption equilibrium. Each one is based on specific assumptions and criteria to have a better description for such an adsorption system. Some of them are complementary or modification to previous work. We are going to focus on Langmuir, Toth isotherms, as they can well describe the adsorption of CO_2 on zeolites.

19

2.4.3.1 Langmuir isotherm

In 1918 Langmuir was the first who proposed a coherent model for describing the adsorption onto flat surface, based on purely kinetic point of view. Where the rate of adsorption equals to the rate of desorption from the surface at maximum surface coverage as shown in Figure 2.14 [69, 70]. He proposed a model based on three fundamental assumptions as follow:[71]

I.   Surface is homogenous, such that the adsorption energy is constant all over the sites and there are no intermolecular interactions between the adsorbed molecules (i.e., they behave ideally).
II. Each site can accommodate only one molecule or atom.
III. Adsorption on surface is localized, such that adsorbed atoms are adsorbed at definite, localized sites.

Combined altogether, he could yield the following expression for the equilibrium fractional occupancy of adsorption sites (θ) under gas phase at pressure P:

$$\theta = \frac{KP}{1+KP} \tag{2.4}$$

Where (K) is the Langmuir constant, which is independent of the pressure (P) and depends only on the temperature. So, when the temperature is invariant, the isotherm can be measured and (K) could be determined experimentally. It has the units of inverse pressure.
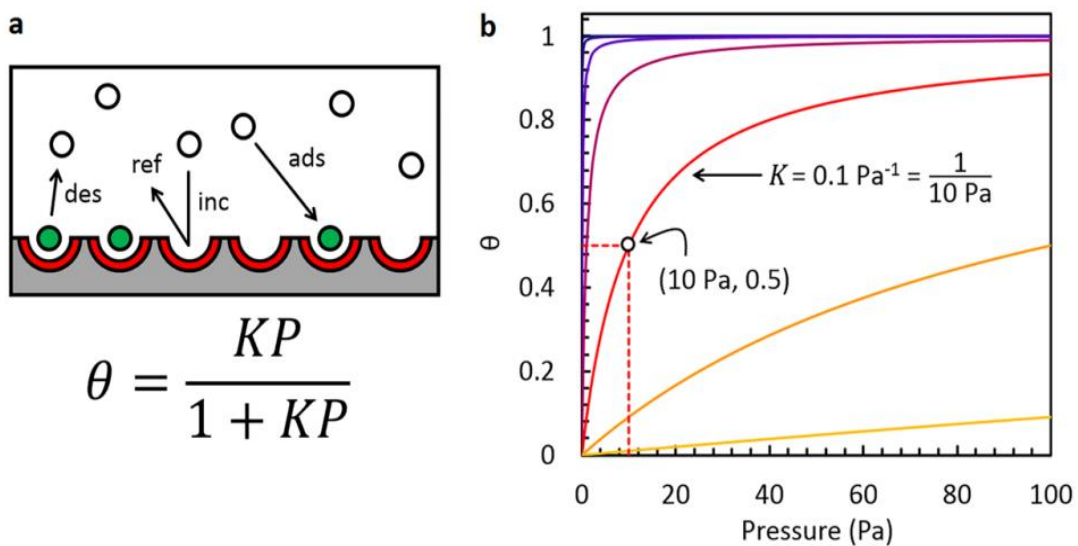
Figure 2.14 (a) Langmuir kinetic model of adsorption. (b) Graphical representation of Langmuir isotherm [72]

2.4.3.2 Toth isotherm

Toth model is one of the most successful isotherms that was found in predicting and describing the adsorption of gases at both low and high pressure on heterogeneous surfaces. It assumes a quasi-Gaussian energy distribution. Toth model takes the following form:[73, 74]

$$q_e \; = \; \frac{q_m b p}{(1 + (bp)^t)^{1/t}} \qquad\qquad (2.5)$$

Where (q_e) is the equilibrium capacity or loading of the adsorbent (mmol/g), (q_m) is the maximum adsorption capacity (mmol/g), (b) is a constant related to the binding or adsorption affinity and (t) is a parameter that characterizes the heterogeneity of the adsorbent. When the surface is homogeneous (i.e., $t = 1$) the Toth isotherm reduces to Langmuir isotherm. The parameters b and t are specific for adsorbate-adsorbent pairs and temperature dependent.

In general, Toth isotherm model has advantages of fewer parameters and high predictive ability for the loading of many adsorbents over a wide range of temperature. Toth isotherm is recommended as the first choice of isotherm equation for fitting adsorption data of many adsorbates such as hydrogen sulfide, alcohols, hydrocarbons, and carbon dioxide on zeolites and activated carbons as encountered in the literature (Fig. 2.15), due to its simplicity and accuracy at low and high pressures regions.[52, 75]
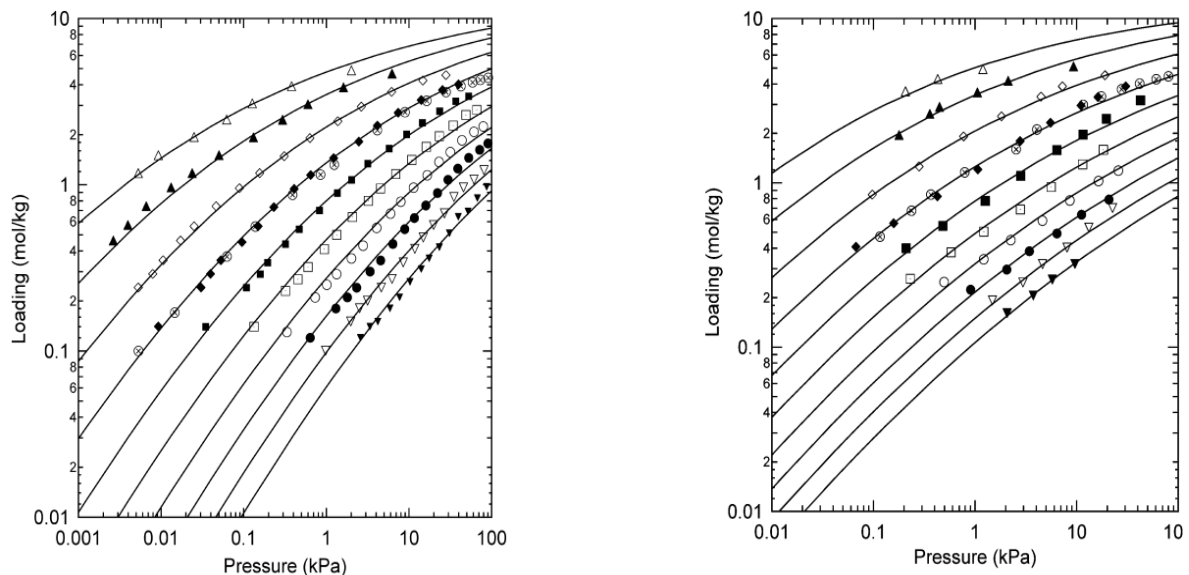
Figure 2.15 Adsorption isotherms of pure CO2 on zeolite 5A (left) and zeolite 13X (right) at different temperatures, solid curves are Toth isotherm [75]

2.4.4 Isosteric heat of adsorption

Isosteric heat of adsorption is one of the most important key design variables in any gas adsorption process. When adsorption process takes place, heat is liberated due to the exothermic nature of the adsorption process. Part of this heat will be absorbed by the adsorbent and the other will be dissipated to the surrounding. The portion absorbed by the solid particle will increase the temperature of the adsorbent surface. Which will slow down the adsorption process, because the mass uptake is controlled by the rate of cooling of the particle in the latter course of adsorption.[52, 76]

Accurate estimation of the isosteric heat of heat of adsorption is a crucial parameter for energy balance calculations in adsorption processes [77]. Isosteric heat of adsorption (q_{st}) measures the difference in enthalpy when adsorbate species are adsorbed from the bulk gas phase to the solid phase [56]. Moreover, it provides an indication about the surface heterogeneity. For an energetically heterogeneous surface, the heat of adsorption decreases with the surface loading [78]. Generally, the isosteric heat of adsorption can be measured by two ways, either by (i) direct measurements using calorimeter or (ii) indirect measurements from experimental adsorption isotherms at different temperatures [79]. The isosteric heat of adsorption is calculated theoretically from the Clausius-Clapeyron equation:[68, 80]

$$q_{st} = RT^2 \left(\frac{\partial \ln P}{\partial T} \right)_n \tag{2.6}$$

Where, (R) is the universal gas constant, (T) is the system temperature, (P) is the system pressure and (n) is the capacity or the amount adsorbed. It should be noted that the Clausius-Clapeyron equation is based on two assumptions:[81]

I. Bulk gas phase is assumed to behave ideally.
II. The volume of the adsorbed phase on the solid is negligible compared to that of the gas phase.

As mentioned above the isosteric heat of adsorption can be estimated from pure component adsorption isotherm, complementary with the use of the Clausius-Clapeyron equation. So, the choice of the isotherm model will greatly affect the estimated heat of adsorption. For instance, Langmuir isotherm is based on the assumption of monolayer coverage on an energetically homogeneous surface (as mentioned in section 2.4.3.1). Thus, the estimated isosteric heat of adsorption based on Langmuir model will be constant and independent of the surface capacity which makes it insufficient in representing most of the experimental data.

On the other hand, Toth isotherm is accurately describing the pure component isotherm by involving the surface heterogeneity parameter (as mentioned in section 2.4.3.2). However, the isosteric heat of adsorption estimated from Toth model has unrealistic infinite negative value at the saturation capacity as shown in Figure 2.16(b). Furthermore, we can see from this figure when the heterogeneity parameter (*f*) becomes unity (i.e., homogeneous surface), the Toth isotherm reduces to Langmuir and therefore, and the heat of adsorption becomes constant.[52, 76]
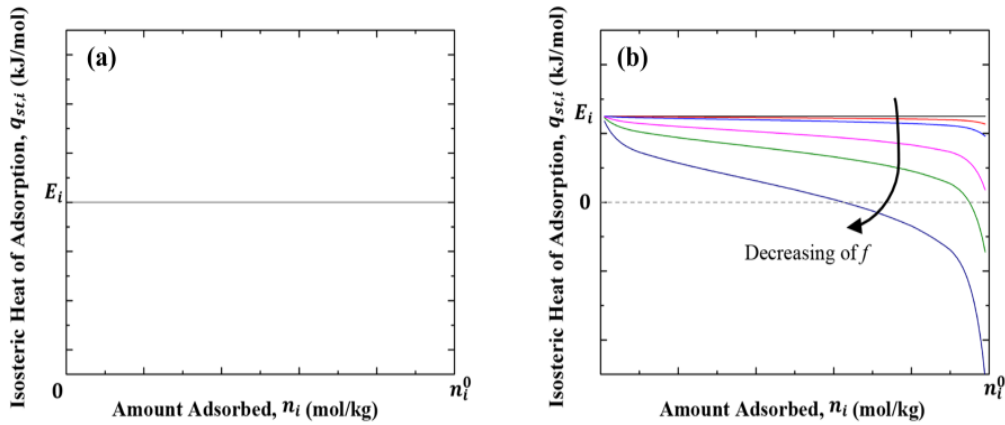
Figure 2.16 Estimation of isosteric heat of adsorption (a) Langmuir (b) Toth [76]

2.4.5   Regeneration

Once the breakthrough occurs and the fixed bed becomes saturated, the process must be shifted to desorption mode, in order to regenerate the spent sorbent and to remove the adsorbed species. Clearly, regeneration process is the decisive parameter for the economy of CO_2 capture systems by adsorption. As the type and the source of energy used for regeneration will play an effective role in the overall operating cost.

Significant reduction in the energy consumption used in the regeneration process in CO_2 capture processes remains one of the main challenges in implementing an effective capture system[82]. Generally, there are two common basic techniques used for regeneration in cyclic adsorption systems using fixed beds: (a) temperature-swing adsorption (b) pressure-swing adsorption, as illustrated in Figure 2.17. Those techniques are normally operated with two or three fixed bed working in parallel, where one column in adsorption cycle while the other one or two in desorbing cycle, in order to have continues operation.[65]
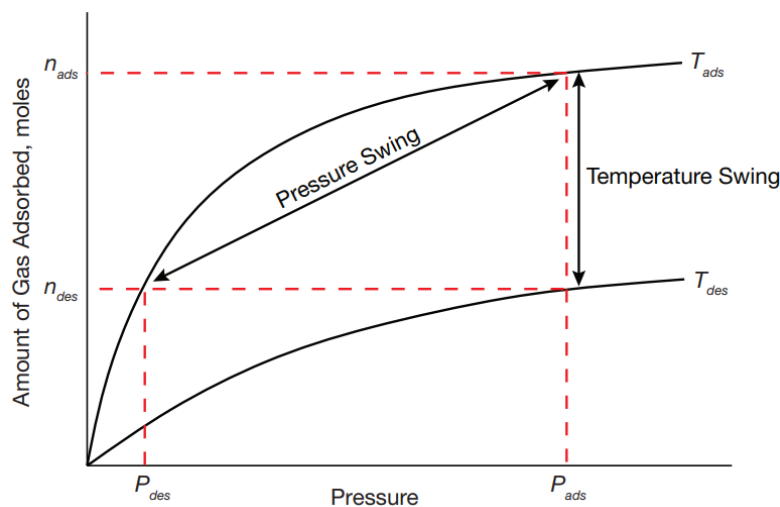
Figure 2.17 difference between the mechanism of regeneration by PSA and TSA [83]

2.4.5.1 Temperature-swing adsorption (TSA)

Essentially TSA takes the advantage of the exothermic nature of the adsorption process. Where increasing the temperature will shift the adsorption equilibrium in a direction that desorb the adsorbed components according to Le Chatelier principle. In conventional TSA applications such as air and natural gas drying, the regeneration of the adsorbent is normally carried out by direct purge with hot nonadsorbing gas or steam [36]. whilst in CO_2 capture systems, the adsorbate CO_2 is the required product, and its purity is important factor. The large volume of gases required for heating the bed (due to the low specific heat capacity of purge gases) would cause a sharp dilution in the concentration of the desorbed CO_2. [84] Therefore, the regeneration of the spent adsorbent is often employed by indirect heating of the bed first to the required regeneration temperature, by using diverse techniques such as: heating jackets, or electric heating coils wrapped around the adsorber (Fig. 2.18). Then the purge gas (mainly N_2 or hot air) is applied for a short period as sweep gas to recover the desorbed species. [85] [86]
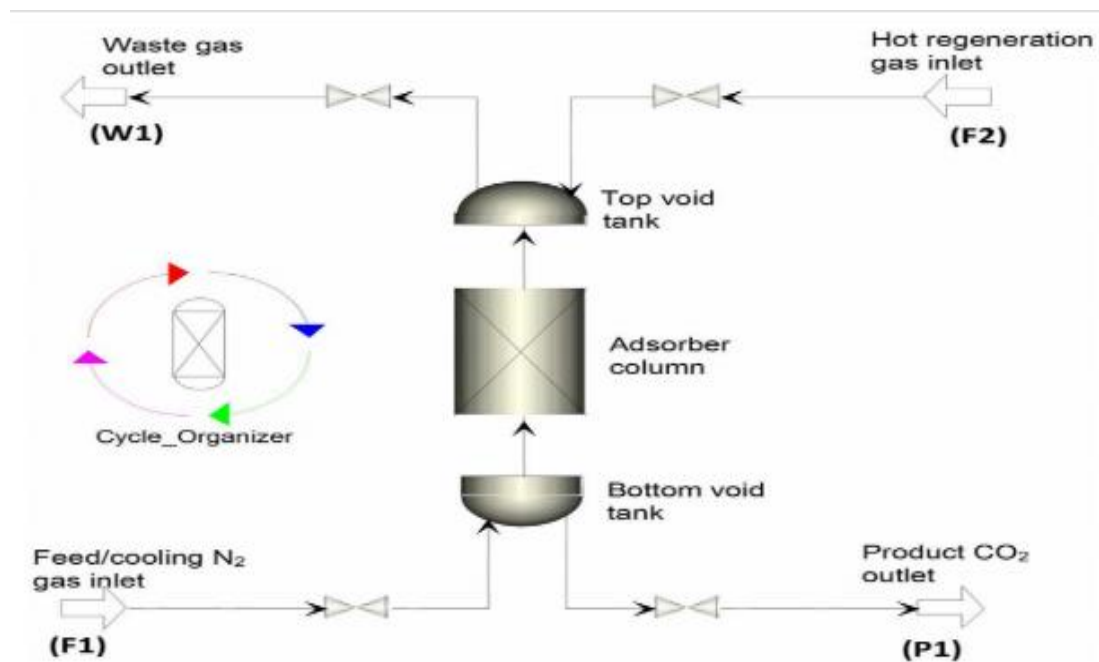
Figure 2.18 Adsorption flowsheet for simulating TSA [82]

2.4.5.2 Pressure-swing adsorption

In PSA the bed is basically regenerated by reducing the bed pressure at constant temperature, followed by purging the bed at this reduced pressure with a small fraction of the desorbed stream. As mentioned in TSA, the desorption or the regeneration process is generally based on Le Chatelier principle, therefore the reduction in pressure will favor the adsorption equilibrium in a direction that causes desorption of the adsorbed species from the adsorbent [87-90]. A special case of PSA applications, where the desorption takes place below atmospheric, is referred to as 'vacuum swing adsorption' (VSA) [91].

Generally, The PSA cycle consists of four steps as illustrated in Figure 2.19 :[87]

- **I.** Pressurization with adsorption product.
- **II.** High-pressure adsorption.
- **III.** High-pressure purge.
- **IV.** Countercurrent expansion to atmospheric or sub-atmospheric pressure.
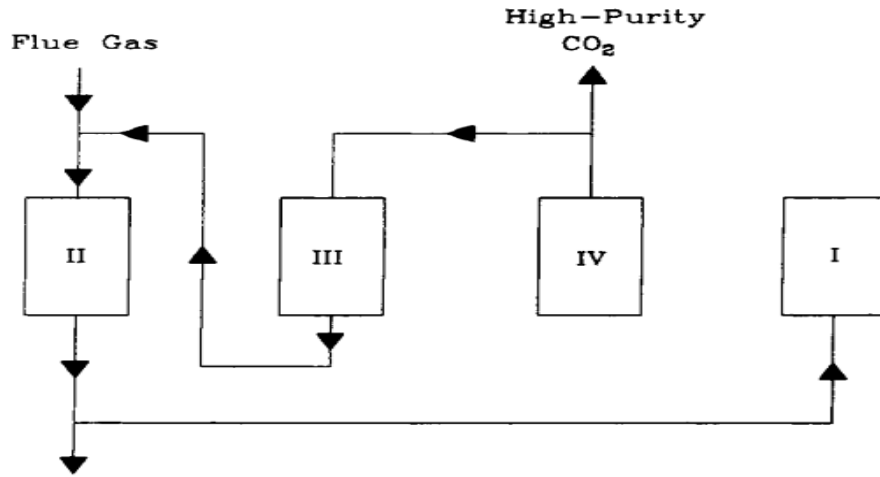
Figure 2.19 Schematic diagram of PSA cycle in CO2 capture system [87]

2.5 Pressure Drop in Packed beds

Pressure drop in fixed packed bed columns is one of the essential key parameters in the design of adsorption process. As the fluid passes through a packed bed, it experiences a pressure loss in its energy due to friction. Basically, the resistance to the flow of fluid through a porous medium is due to the total drag forces in all particles in the bed, depending on many factors such as: Reynolds number, type of the flow (i.e., laminar or turbulent), the void fraction and the irregularity of the surface. Most of the pressure drop is contributed to the kinetic energy losses caused by changes in channel cross section and flow direction.[60]

The most common practical approach for calculating the pressure drop through a packed bed of solid particles, is based on estimates of total drag on the solid boundaries of the tortuous (i.e., nonuniform) channels and pores through the bed. It is important to consider that the actual channels or pores are irregular in shape and not uniformly distributed. Thus, they have a variant cross section and orientation, and they are highly interconnected. However, for simplicity it is assumed that the bed has a set of uniform circular pores whose total surface area and void volume match those of the bed in order to calculate an equivalent channel diameter. Also, it is more convenient and accurate to base the calculations on the surface area/volume ratio for the fraction of the solid particles. This ratio in case of spherical particles equals to $6/D_p$, as $s_p = \pi D_p^2$ and $v_p = \frac{1}{6} \pi D_p^3$. In case of irregular shape, (i.e., non-

spherical) this ratio will include a term called sphericity (Φ_s) through the following equation:[60]

$$\frac{s_p}{v_p} = \frac{6}{\Phi_s D_p} \tag{2.7}$$

Where, (s_p) is the surface area of the solid particle, (v_p) is the volume of the particle and (D_p) is the particle diameter.

On performing calculations for the pressure drop it is important to consider the average velocity of the fluid in the pores ($\bar{V}$) which is directly proportional to the empty-tower superficial velocity ($\bar{V}_0$) and inversely proportional to the porosity or the void fraction (ε):

$$\bar{V} = \frac{\bar{V}_0}{\varepsilon} \tag{2.8}$$

The pressure drop is calculated from equations initially presented for channel flow by Darcy. To apply them in a porous media, the same characteristics quantities must be introduced for correlation of the pressure drop in packed bed of solid particles.[92]

For flow at low Reynolds number (i.e., Laminar flow) which is also known as Darcian flow, there is a linear relationship between the pressure drop and the mass flow rate, as the pressure drop varies with the first power of the velocity (i.e., $\Delta P \propto \bar{V}_0$). The pressure drop in this case is given by the Kozeny-Carman equation: [93]

$$\frac{\Delta P}{L} = \frac{150\bar{V}_0\mu}{\Phi_s^2 D_p^2} \frac{(1-\varepsilon)^2}{\varepsilon^3} \tag{2.9}$$

The Kozeny-Carman equation is applicable to flow through packed beds at particle Reynolds number up to 1. The constant 150 accounts for the tortuosity of the surface particle.

As the flow rate increases (i.e., the superficial velocity increases), the flow will become turbulent, and the inertial effects will contribute to an increasing role in the pressure drop, as the pressure will vary with the 2nd power of the superficial velocity ($\Delta P \propto \bar{V}_0^2$). In this case the pressure drop is given by the Bruke-Plummer equation which is applicable for flow of particle Reynolds number higher than 1000: [94]

$$\frac{\Delta P}{L} = \frac{1.75\rho\bar{V}_0^2}{\Phi_s D_p} \frac{1-\varepsilon}{\varepsilon^3} \tag{2.10}$$

An equation that is covering the entire range of flow rates is the Ergun equation. It assumes that the viscous losses and the kinetic energy losses are additive. The equation takes the following form:[95, 96]

$$\frac{\Delta P}{L} = \frac{150\bar{V}_0\mu}{\Phi_s^2 D_p^2} \frac{(1-\varepsilon)^2}{\varepsilon^3} + \frac{1.75\rho\bar{V}_0^2}{\Phi_s D_p} \frac{1-\varepsilon}{\varepsilon^3} \tag{2.11}$$

Where, (ΔP) is the pressure drop, (L) is the bed length, ($\bar{V}_0$) is the fluid superficial velocity, (Φ_s) is the sphericity, (D_p) is the particle diameter, (μ) is the fluid viscosity, (ρ) is the fluid density and (ε) is the void fraction.

The Ergun equation can describe and fit the data of spheres, cylinders, and crushed solids over a wide range of flowrates. Moreover, Ergun varied the packing density for some materials in order to verify the term $(1 - \varepsilon)^2/\varepsilon^3$ for the losses due to viscosity and the term $(1 - \varepsilon)/\varepsilon^3$ for the kinetic energy losses[97]. It can be concluded from the previous equation (Eq. 2.11) that a small change in ε will cause a dramatic change on the value ΔP, which in turn makes it difficult to predict the pressure drop accurately. Therefore, it is important to take into consideration the importance of estimating the void fraction of the particles accurately to interpret reasonable results for the pressure drop. Generally, the void fractions for spherical and cylindrical packings range from 0.3 to 0.6 depending on the ratio of the particle diameter to the tube diameter (D_P/D_t) as shown in the Table 2.3. [98]

Table 2.3 Void fractions for dumped packings [60]

D_P/D_t	ε for spheres	ε for cylinders
0	0.34	0.34
0.1	0.38	0.35
0.2	0.42	0.39
0.3	0.46	0.45
0.4	0.50	0.53
0.5	0.55	0.60

There is a strong dependency of the pressure drop on the void fraction which causes a nonuniform distribution of the velocity across the packed bed. As the disturbance of the statistical particle arrangement adjacent to the wall generates a higher void fraction than the average value in the bed. That causes a near-wall bypass flow as the velocity near the walls of the column will be higher.[92, 99]

Figure 2.20 shows the radial void fraction distribution in a packed bed column at different radial positions from the wall. It can be observed that the void fraction (ε) decreases from unity at the wall (i.e., r/d = 0) till it reaches a minimum value of $\varepsilon = 0.2$ at a distance of half sphere diameter from the wall (i.e., r/d = 0.5). Then the void fraction value fluctuates till it reaches a constant value at distance nearly equals to four sphere diameters (i.e., r/d = 4) from the wall. [100, 101]
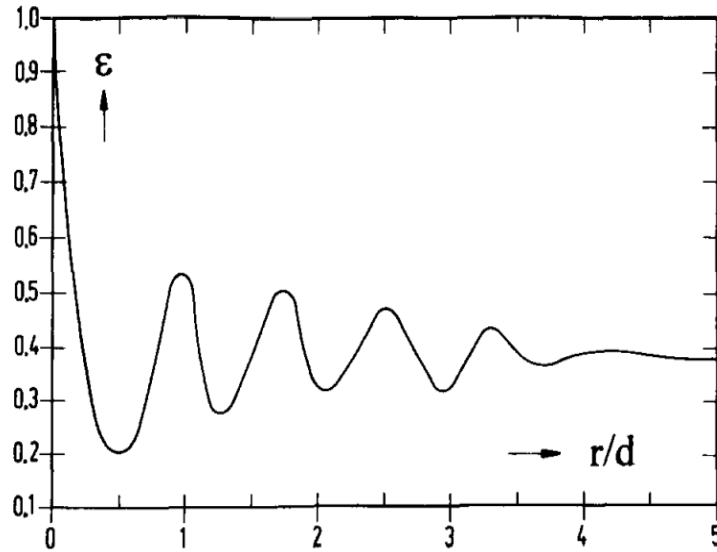
Figure 2.20 Radial void fraction distribution [92]

Therefore, the effect of the bypass is one of the main contributors for the severe deviations of the predicted pressure drop results from the actual values. That can be illustrated in Figure 2.21, which reflects the response of the pressure drop in packed bed due to void fraction changes. Also, the higher the ratio of sphere or particle to tube diameter (d_p /d_t), the stronger the influence of the bypass effect on the pressure drop. As a result, in order to interpret reasonable calculations for the pressure drop in packed beds, a correction factor for the bypass effect is required.[102-104]
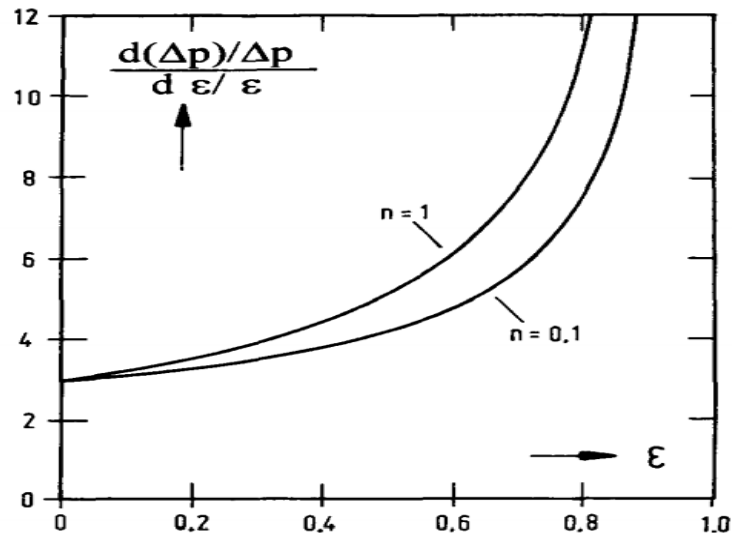
Figure 2.21 Sensitivity of the pressure drop to changes in the void fractions [92]

2.6   Design of fixed bed adsorbers

Figure 2.22 illustrates the typical configuration of gas adsorption system employing dual fixed beds of adsorbents. Meanwhile one bed is in adsorption mode, the other is in regeneration. The bed height ranges from 0.3 to 1.5 m. Where the adsorbent particles are supported on a screen or perforated plate. Mostly, downflow of the gas stream in adsorption is preferred as the upward flow at high rates may cause fluidization, attrition, and loss of the particles. However, in desorption the flow is upward to have higher efficiency[66]. The bed depth is normally about 5-10 times the mass transfer zone to have economical operation[105].
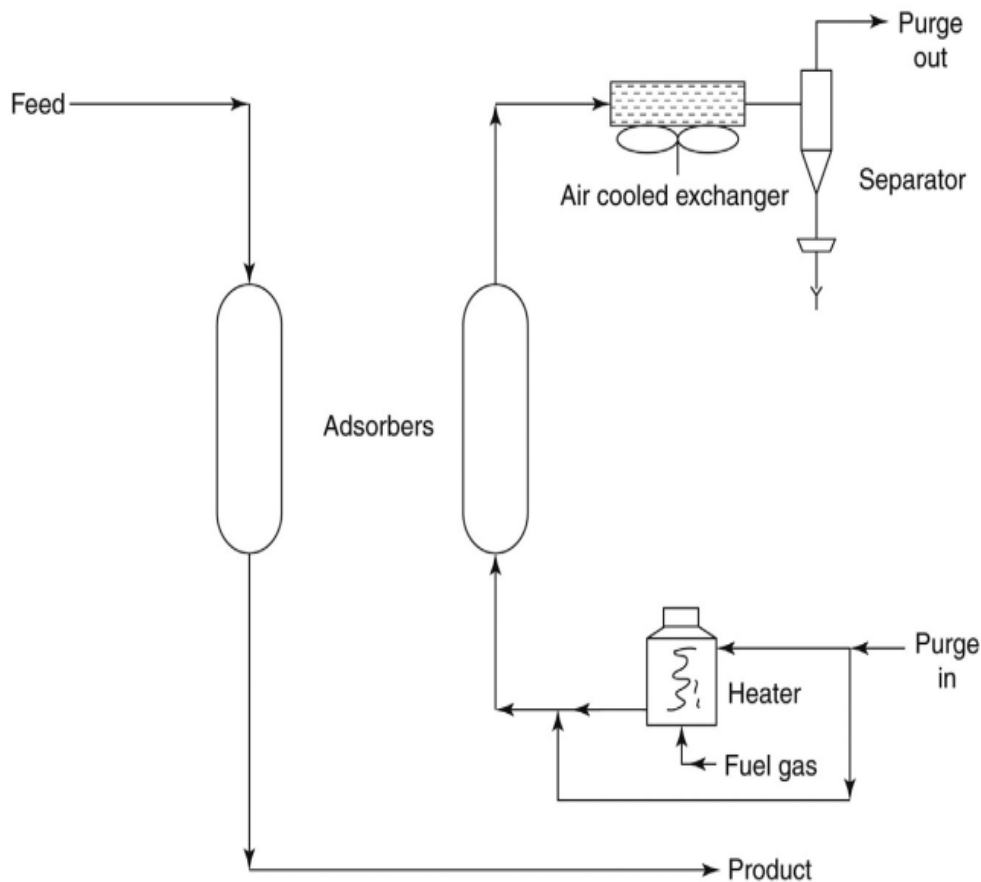
Figure 2.22 Dual fixed bed adsorption system [106]

The size (cross sectional area) of the bed is chosen to give a low gas superficial velocity ranges from 0.15 to 0.45 m/sec, to avoid higher pressure drop. In case of large flow rates, a rectangular bed may be installed in the middle of a horizontal cylinder instead of vertical tank with a diameter much greater than the bed height. The adsorption cycle time takes about 0.5 up to 8 hrs.[60, 65]

One common configuration that is used in most large volume operations of fixed bed adsorption system can be seen in Figure 2.23. The system employs three columns in series. Two columns are operating in adsorption mode, while the other is regenerating or desorbing. This configuration is usually used when the mass transfer zone is wide or large, as the adsorption till equilibration takes place in 2 columns instead of one column. Throughout this configuration, column 1 will reach saturation faster than column 2, so the adsorption cycle will continue with column 2 and the standby column 3. While column 1 will shift to desorption mode and column 2 reaches saturation. Then, the adsorption cycle continues with both column 3 and the regenerated column 1, and column 2 will shift to the regenerating mode, and so on. In this manner each column cycles between adsorption and desorption without interruption for regeneration that would be required for a process with a single column.[106]
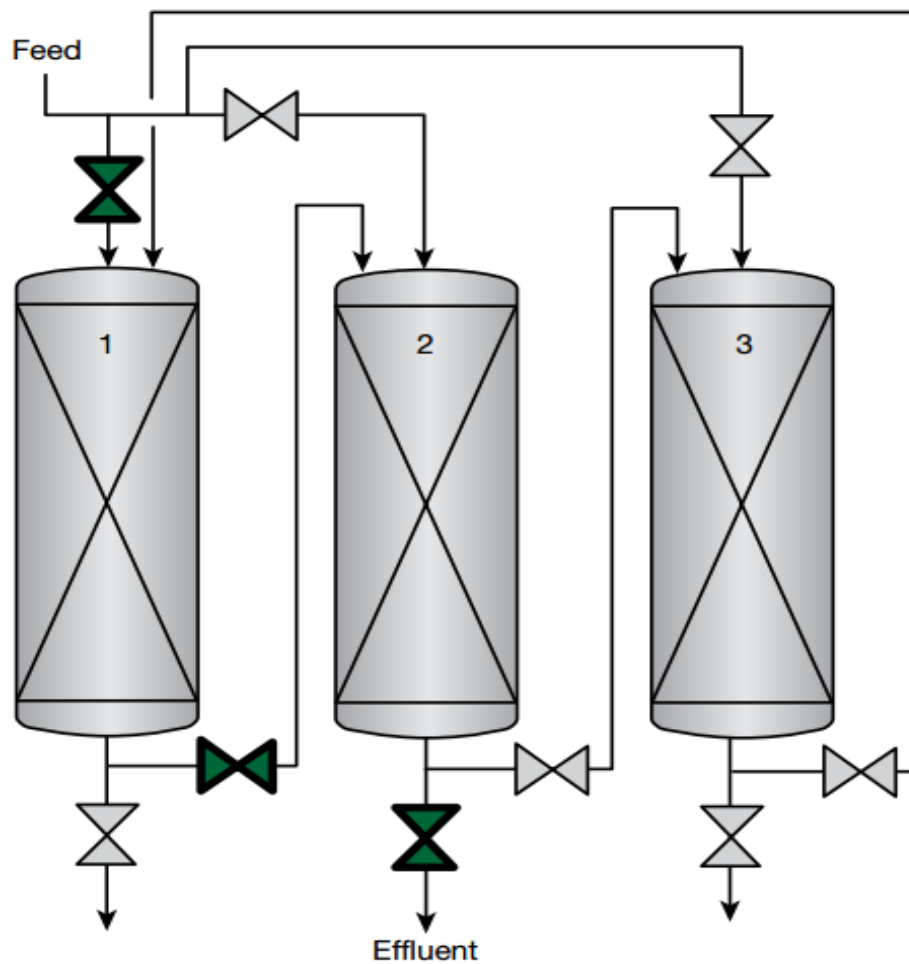
Figure 2.23 Three fixed bed columns arrangement [64]

3 Experimental Part

The objective of this chapter is to present the materials and equipment used for conducting the experimental work during this project. Also, the setup of the adsorption facility used will be described by showing the procedures and the methodology applied to implement the required assessments. In addition, the theoretical models used for predicting the experimental results to check the validity of the obtained results, and findings will be reviewed.

3.1 Materials

Three commercially available adsorbents for the adsorption of CO_2 from air were used in this study. The adsorbents were, MSC-544, MSC-542, and SP-564 with average particle diameter of 0.00205, 0.00375, and 0.006 m, respectively. They are all zeolites of the type 13X, that has pore size of 10Å. They are highly porous, crystalline aluminosilicate in beaded form. Silica gel (SG-W 127) with very high purity (approximately 99.6% of SiO_2) in beaded form with average particle diameter 0.0032 m was used for drying the air (i.e., removal of humidity), prior to treatment with the zeolites. All the adsorbents were supplied by Grace Davison company. They were stored and kept in air-tight tanks after drying and before charging to adsorption columns. It should be noted that the given void fraction value of the zeolite adsorbents was 0.4, however this value was based on inaccurate estimation and needed further correction, as it will be discussed thoroughly in section 4.5.1.

The following table summarizes the characteristics and specifications of the used adsorbents in the project.

Table 3.1 Characteristics and specifications of the adsorbents used in the project

Adsorbent	Average particle diameter (m)	Bulk density (kg/m³)
MSC-544	0.00205	675
MSC-522	0.00375	640
SP-564	0.006	615
SG-W 127	0.0032	620

3.2 Setup of the adsorption facility

The experimental work was carried out at Z8.1 test facility at Green-Cap solutions company, located in Stavanger, Norway. The facility consists of three cylindrical fixed packed bed, stainless steel columns (C-101, C-102, and C103) as shown in Figure 3.1. Each column has effective length of 1.5 m, and internal diameter of 0.212 m. The column is made of steel and jacketed all around to control the bed temperature.

The column bypass is incorporated for calibration and sampling purposes. There exist 6 sampling points for the whole facility. Each column has two sampling points at the top and bottom of the column (HA-122 to HA-127). The sampling points are connected to sampling bottle (i.e., collector) by using quick-fit connector (solenoid valve), for easy coupling and uncoupling. The sampling points are used for measuring the CO_2 concentration and pressure drop across the column.

The flow controller (FIC-101) was used to adjust the required flowrates of air flow by using the PLC display. The self-regulating control valve (PCV-101) was used to regulate the inlet pressure of the incoming air flow to the adsorption columns. Solenoid valves XV-103 and XV-104 are used for controlling the flow direction in the adsorption and desorption cycles.

There exist 9 temperature sensors for the whole facility (TIT-108 to TIT-116). Each column has three temperature sensors located at the top, middle, and bottom of the column. The sensors are located inside the column at definite central positions along its length to record the temperatures profile. All the temperature sensors are insulated type-K thermocouples. Six pressure sensors were used for the whole facility to record the pressure profile across the columns (PIT-102 to PIT-107). Each column has two pressure sensors located at the top and the bottom. Similarly, six humidity sensors were incorporated for the facility in order to measure the relative humidity of the air flow at the top and the bottom of each column (AIT-106 to AIT-111).

Regeneration of the spent sorbents was carried out by utilizing hot air through three electric heaters. H-101 and H-102 are used for the desorption of humidity from columns C-101 and C-103, respectively. While H-103 is used for the desorption of CO_2 from C-102.

The outlet CO_2 concentration from C-102 was measured by connecting internal probes of KIMO device (HQ210 version) to the bottom sampling port of the column (HA-124). The device measures the concentration at regular time interval of 5 min, using a data logger. While the pressure drop across column C-102 was measured by connecting differential pressure manometer to the top and bottom sampling ports (HA-124 and HA-125). Figure 3.2 depicts a schematic representation of the devices used for measuring the CO_2 concentration and the pressure drop.

	Adsorption cycle	Desorption cycle
Flow direction	———	———
XV-103	Open	Closed
XV-104	Closed	Open
H-101	Off	On
H-102	On	Off
H-103	Off	On
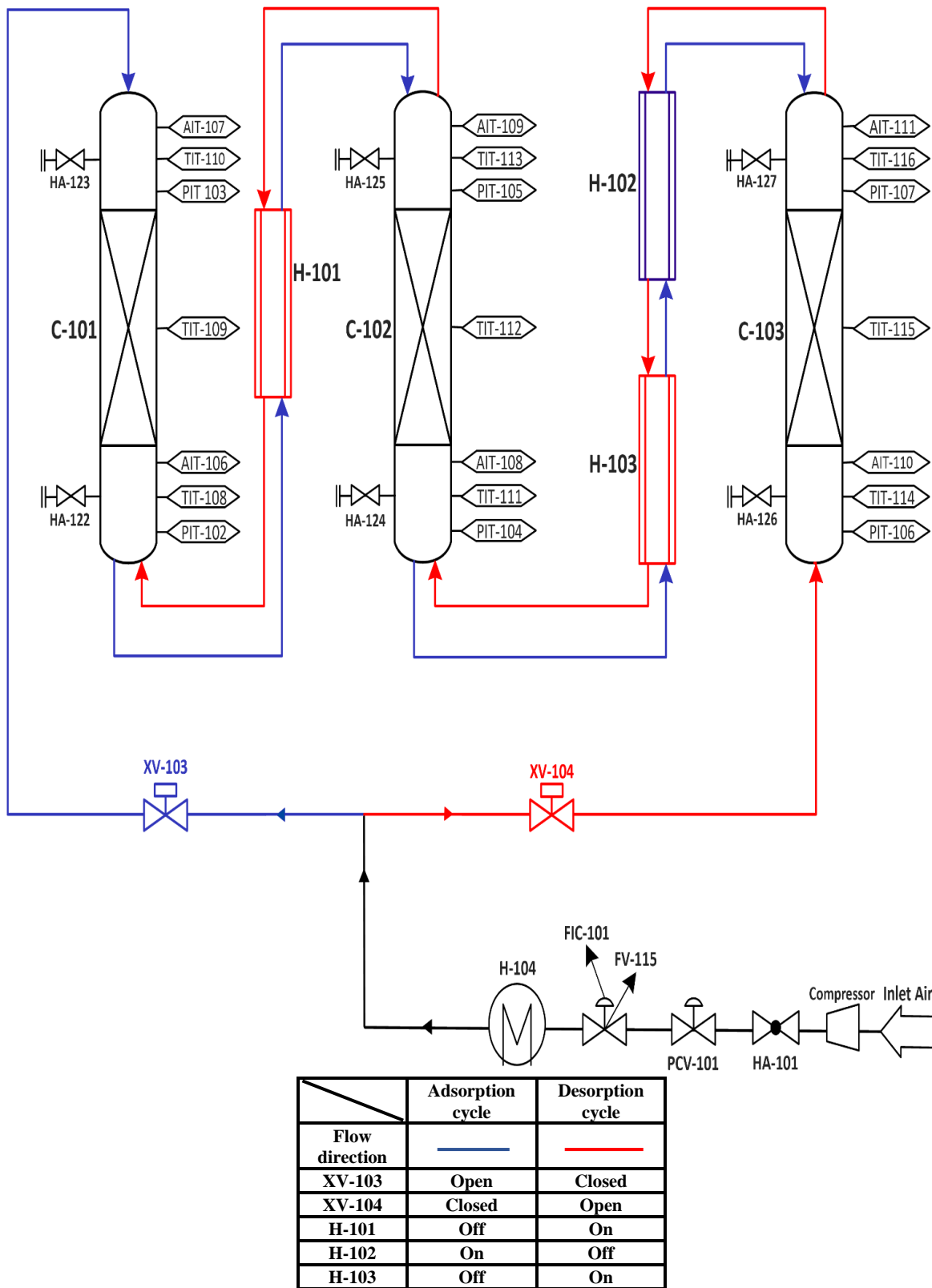
Figure 3.1 Process flow diagram of adsorption facility Z8.1 used in the project

(a) **(b)**

**Figure 3.2 (a) KIMO datalogger for measuring the outlet CO₂ concentration from column C-102
(b) Differential pressure manometer used for measuring the pressure drop across C-102**

3.3 Procedures of the adsorption process

Each run was divided into two phases, the adsorption cycle, and the desorption cycle. Columns C-101 and C-103 are filled with 0.0175 m^3 silica gel, equivalent to packing height of 0.5 m. While C-102 is filled with 0.0123 m^3 zeolites (MSC-544, MSC-542, or SP-564), equivalent to packing height of 0.35 m. Table 3.2 summarizes the volume of the zeolites and silica gel used in the project with the equivalent masses.

Table 3.2 Amount of adsorbents used in the experimental work

C-101 and C-103 (Humidity removal)					C-102 (CO₂ removal)				
Packing material	Column height (m)	Packing volume (m^3)	Packing height (m)	Packing mass (kg)	Packing material	Column height (m)	Packing volume (m^3)	Packing height (m)	Packing mass (kg)
					MSC-544	1.5	0.0123	0.35	8.318
SG-W 127	1.5	0.0175	0.5	10.85	MSC-542	1.5	0.0123	0.35	7.872
					SP-564	1.5	0.0123	0.35	7.564

Adsorption cycle

Atmospheric air was sucked and compressed by using electric mobile air compressor (Atlas Copco H185 VSD). Then it is passed to air cooler (H-104) for adjusting the desired operating temperature using the PLC display. The flowrate of the air to the top of column C-101 is adjusted by flow controller FIC-101 in conjunction with valve FV-115 and setting the self-regulating control valve (PCV-101) to one bar. In adsorption cycle valve XV-103 is open, while valve XV-104 is closed. The type of the flow was downflow (i.e., from top to bottom) to avoid fluidization of the adsorbent particles. Three operating flowrates were employed during the project, 25.3, 31.6, and 38 m^3/hr, which were equivalent to superficial velocities of 0.2, 0.25, and 0.3 m/sec, respectively.

After dehumidifying the air in C-101, it will flow to C-102 (the zeolite column) for adsorbing the CO_2. Then, the treated air shall be heated up into 200℃ (the set temperature for desorbing the water vapor) by the electric heater H-102, to desorb the humidity and regenerate the silica gel bed of column C-103. As column C-103 will be used for drying the hot air that will be utilized in the desorption cycle later. It should be noted that during the adsorption cycle, columns C-101 and C-102 are in adsorption mode, while C-103 is in desorption mode. Therefore, during the adsorption cycle the electric heaters H-101 and H-103 (i.e., the electric heaters of C-101 and C-102) are shut down, while H-102 is turned on. The opposite configuration takes place in the desorption cycle.

Desorption cycle

Several hours after the CO_2 outlet concentration from C-102 was the same as the feed and kept constant, and the 2nd adsorber (C-102) is considered to be saturated with CO_2. The adsorption cycle was stopped, and the process was shifted to the desorption mode. The regeneration of C-101 and C-102 was carried out by utilizing hot air provided by passing the air to the electric heaters H-103 and H-101 to heat the air up to 220 and 200 ℃ respectively, which are the set temperatures of desorbing the carbon dioxide and humidity, respectively. Those temperatures were determined based on preliminary performed tests and calculations. In the desorption cycle the flow direction is reversed (i.e., upward flow). As the valve XV-104 will be open and valve XV-103 will be closed. Where the air enters first C-103, then C-102 and C-101, as depicted in Figure 3.1 by the red color.

It should be noted that, fresh adsorbents were used during each experimental run. That was due the fact that the adsorbents were not fully regenerated during the desorption cycle. Since the set temperatures for desorbing the CO_2 and humidity could not be reached because of insufficient insulation around the towers, piping and heaters which caused heat transfer with the surrounding. Moreover, due to the same reason, the effect of varying the temperature on the adsorption capacity could not be investigated and studied, as temperatures lower than ambient were not able to be achieved.

3.4 Methodology and theoretical basis

All the experimental results that carried out during the project and shall be discussed in the next chapter were focused on the zeolite column (C-102). The main target of the experimental work was to evaluate and study the effect of varying flowrate on the breakthrough curve behavior, the adsorption capacity, the bed efficiency (i.e., mass transfer zone), and the pressure drop across the height of packing. That methodology was applied for each adsorbent utilized in the project, as illustrated in Figure 3.3.
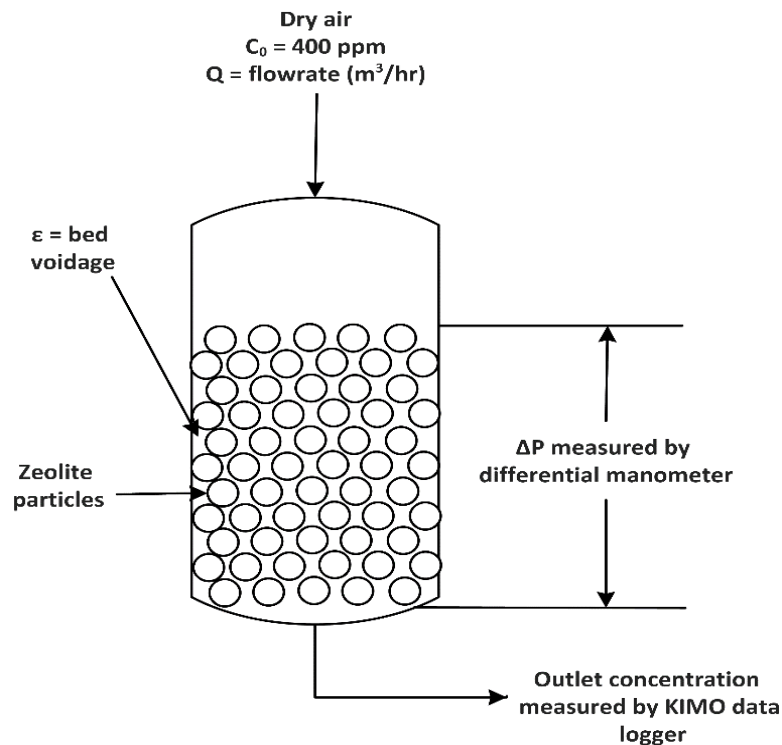
Figure 3.3 Schematic representation of the experimental work implemented on column C-102

3.4.1 Effect of varying the flowrate of the inlet air

The influence of varying the flowrate on the breakthrough curve behavior and the kinetics of CO_2 adsorption on zeolite 13X was studied at flowrates of 25.3, 31.6, and 38 m³/hr, under constant conditions of inlet temperature at 19°C, inlet CO_2 concentration around 400 ppm and atmospheric pressure. The outlet CO_2 concentration from column C-102 was measured by KIMO data logger and plotted against the adsorption time to give the breakthrough curve. It should be mentioned that during some experimental runs, there were fluctuations in the inlet CO_2 concentration below or above 400 ppm. All the calculations that will be presented in the next chapter are based on the actual operating conditions of each run. However, the inlet concentration will be assumed constant at 400 ppm for comparisons. As the fluctuations in the inlet concentration were not of great influence on the results.

3.4.2 Adsorption capacity and column efficiency

The mass transfer zone width and shape basically rely on the adsorption isotherm, flowrate, mass transfer rate to the sorbent particles and diffusion into the pores. Various theoretical models have been published for predicting the mass transfer zone and concentrations profiles along packed beds. The estimated results can be inadequate due to many uncertainties in the flow patterns and correlations for predicting diffusion and mass transfer.

The total stoichiometric capacity of the packed bed tower if the entire bed comes to saturation with the incoming feed, is directly proportional to the area between the curve and a line at $C/C_0 = 1$, which is represented as $(A_1 + A_2)$ in Figure 3.4. The time equivalent to the total or the stoichiometric capacity of the bed (t_{st}) can be calculated from the following equation:[65]

$$t_{st} = \int_0^\infty \left(1 - \frac{c}{c_0}\right) dt \tag{3.1}$$

The saturation capacity of the adsorbent that is corresponding to stoichiometric time (t_{st}) is estimated as follow:[107]

$$q = \frac{m_{CO_2}^0 \, t_{st}}{M} \tag{3.2}$$

$$m_{CO_2}^0 = \frac{Q * C_0 * 10^{-6} * \rho_{air} * M.wt_{CO_2} * 1000}{M.wt_{air}} \tag{3.3}$$

where, $(m_{CO_2}^0)$ is the mass flowrate of CO_2 in the inlet air to the column (g/hr), (t_{st}) is the time equivalent to the stoichiometric capacity (hr), (q) is the saturation capacity or the loading of the adsorbent (g CO_2/Kg adsorbent), (M) is the mass of the adsorbent (Kg), (C_0) is the CO_2 concentration of the incoming air (ppm), (c) is the effluent concentration of CO_2 (ppm), (Q) is the volumetric flowrate of the incoming air (m³/hr), (ρ_{air}) is the air density (1.2 Kg/m³), $(M.wt_{CO_2})$ is the molecular weight of CO_2 (44.01 g/mol) and $(M.wt_{air})$ is the molecular weight of air (28.97 g/mol).

The time equivalent to the usable capacity of the bed up to the break point (t_u) is represented by area A_1 in Figure 3.4, and given by the following equation:[65]

$$t_u = \int_0^{t_b} \left(1 - \frac{c}{c_0}\right) dt \tag{3.4}$$

Where (t_b) is the breakthrough time which is the time corresponding to relative concentration $(C/C_o) = 0.05$. The value of t_u is very close to that of t_b and is normally taken the same as the breakthrough time. Numerical integrations of the equations 3.1 and 3.4 can be done using spreadsheets.

.
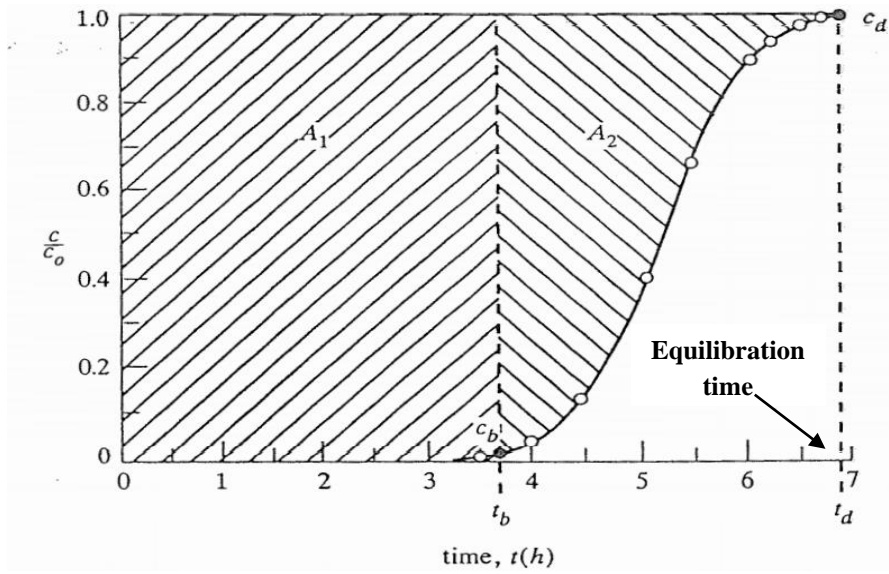
Figure 3.4 Illustrative example of breakthrough curve for determining the bed capacity from the graph [65]

One of the most important parameters in designing and scaling up the adsorbers is to calculate the fraction of the total bed capacity or the length utilized till the break point (H_B) which is given by multiplying the ratio (t_u/t_{st}) with the total bed height (H) as follow:[65]

$$H_B = \frac{t_u}{t_{st}} \times H \qquad (3.5)$$

The ratio of t_u/t_{st} represents the total bed capacity or the portion of the bed that has been utilized up to the break point, which gives an indication on the bed efficiency in capturing the CO_2. Therefore, the column efficiency (η) based on the fraction of the total column capacity that is efficiently utilized can be given as follow:[108]

$$\eta = \frac{t_u}{t_{st}} \times 100 \qquad (3.6)$$

Consequently, the length of the unused part of the bed (H_{UNB}) equals to the fraction of unused part multiplied by the total bed length: [65]

$$H_{UNB} = \left(1 - \frac{t_u}{t_{st}}\right) \times H \qquad (3.7)$$

Basically, the H_{UNB} describes or represents the mass transfer zone which is dependent on many parameters. One of which is the superficial velocity of the fluid to be treated. As shown in Figure 3.5, for a narrow mass transfer zone, the breakthrough curve is steeper and almost most of the bed capacity is used at the break point, which is an indication of efficient use of the adsorbent and hence, makes the regeneration easier. The opposite case is when the mass transfer zone is wide. In that case the breakthrough curve is less steep, and the portion of the unused bed will be higher which indicates inefficient utilization of the bed capacity.[60]
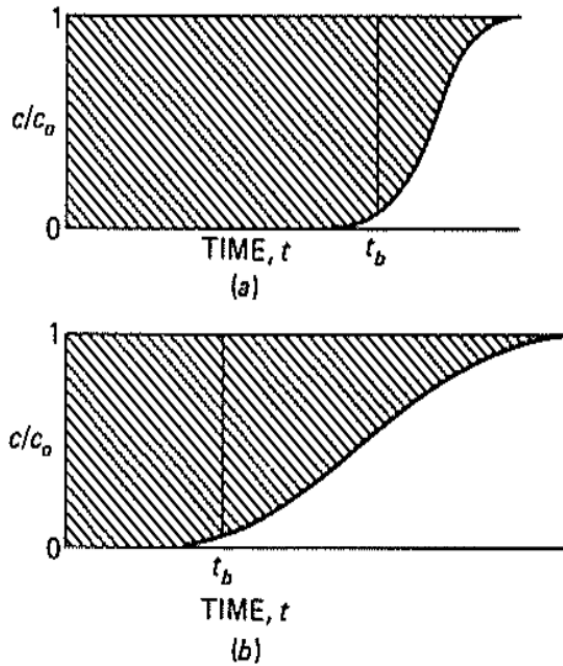
Figure 3.5 Breakthrough curves for (a) narrow and (b) wide mass-transfer zones [60]

Generally, good adsorbent is characterized by having small width or length of mass transfer zone. Steady state pattern for CO_2 adsorption was assumed for evaluating the length of the mass transfer zone, and is given as follow:[108]

$$L_{MTZ} = \frac{2\,H\,(t_{st} - t_b)}{(t_{st} + t_b)} \qquad (3.8)$$

3.4.3   Verification of the breakthrough curves with Thomas model

The experimental breakthrough curves data shall be compared and verified with an appropriate adsorption model, in order to describe and predict the behavior of the fixed packed bed (i.e., column C-102) and to scale it up for industrial purposes. Thomas model is commonly used for fitting fixed packed bed breakthrough curves in environmental sorption and biosorption applications as shown in Figure 3.6. Basically, Thomas model is similar to Bohart-Adams model [109]. The model is based on the Langmuir kinetics [110]. It has a unique feature of being able to describe the effect of the superficial velocity of the feed on the breakthrough curve as it is dependent on the volumetric flowrate (Eq. 3.9 and 3.10). Normally, linear least square analysis is often used for obtaining the parameters of Thomas model [111-113]. In the present study, both linear and nonlinear regressive models were used for predicting the breakthrough curves behavior of the adsorption of CO_2 onto zeolites 13X, as well as the model parameters. Moreover, error analysis for fitting the breakthrough curves was also analyzed.
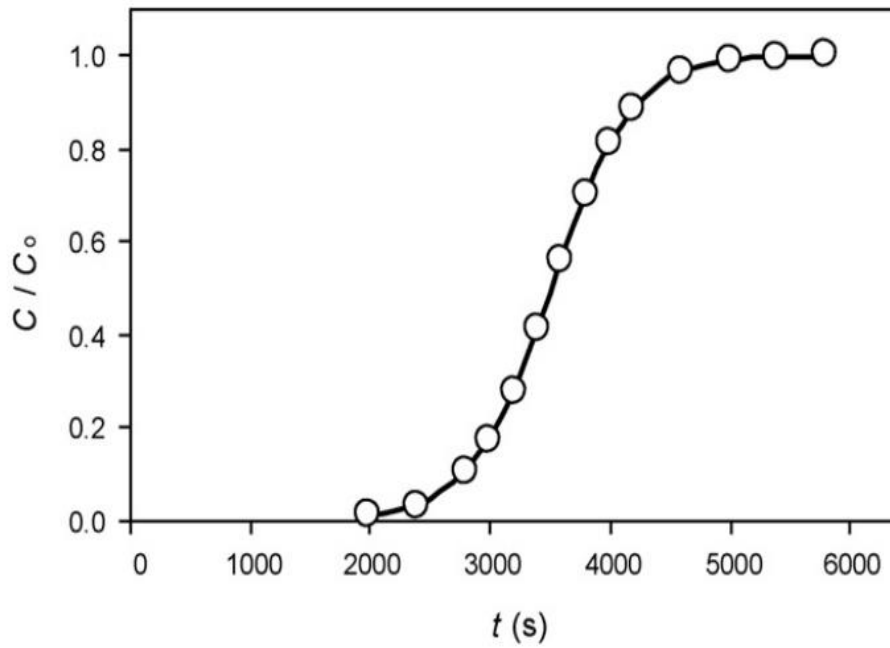
Figure 3.6 Breakthrough curve fitted with Thomas model [109]

3.4.3.1 Thomas adsorption model

The linearized form of Thomas model is given by the following equation:

$$\ln\left(\frac{C_0}{C} - 1\right) = \frac{K_{Th}q_0 M}{Q} - K_{Th}C_0 t \qquad (3.9)$$

Where, (C_0) is the adsorbate concentration in the incoming feed (g/m^3), (C) is the equilibrium sorbate concentration which is the concentration of the adsorbate in the effluent from the bed (g/m^3), (q_0) is the adsorption capacity or the loading of the adsorbent per unit mass of adsorbent (g CO_2/Kg adsorbent), (M) is the mass of the adsorbent (Kg), (Q) is the volumetric flowrate (m^3/hr) , (K_{Th}) is the Thomas rate constant $(m^3/g.hr)$ and (t) is the adsorption time (hr).

The values of (K_{Th}) and (q_0) can be obtained by plotting $\ln\left(\frac{C_0}{C} - 1\right)$ against (t), using least square linear regression analysis. Where the slope is $(K_{Th}C_0)$ and the intercept is $\left(\frac{K_{Th}q_0 M}{Q}\right)$. figure 3.7 illustrates the linearized form of Thomas model for fitting experimental breakthrough data.
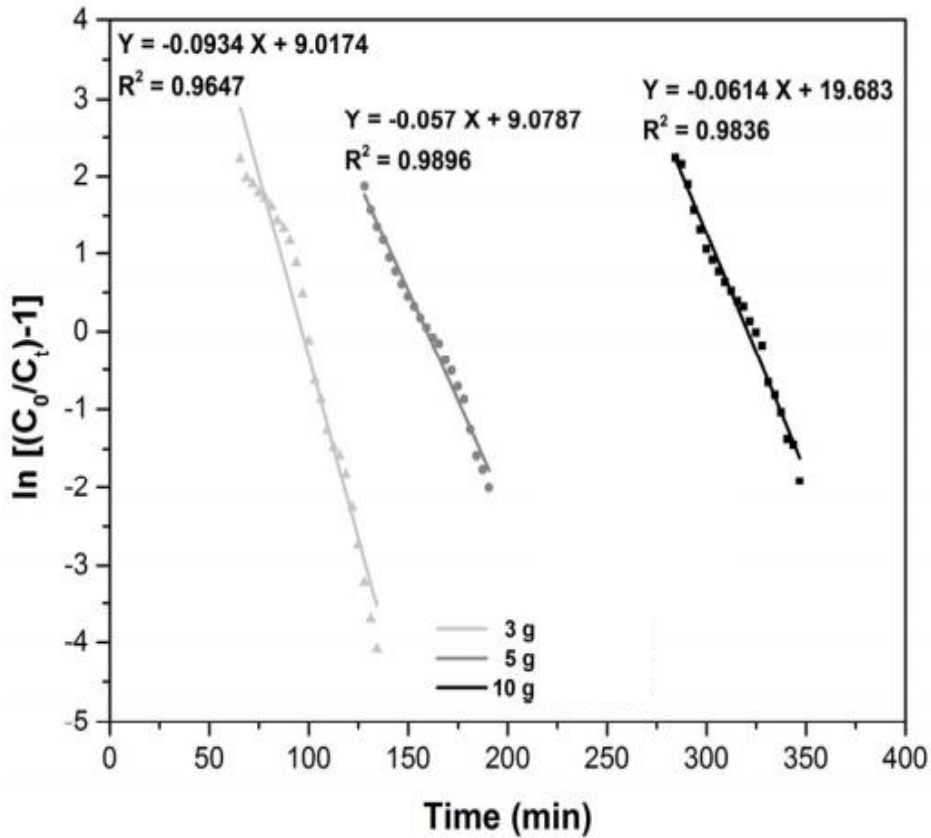
Figure 3.7 Linearized Thomas model plots for fitting breakthrough curve at different amounts of adsorbent [114]

The nonlinear form of Thomas model takes the following form:

$$\frac{C}{C_0} = \frac{1}{1 + exp\left(\frac{K_{Th}q_0M}{Q} - K_{Th}C_0t\right)} \tag{3.10}$$

The nonlinear regression analysis of Thomas model was performed by fitting the experimental breakthrough data to Eq. 3.10. That was implemented by using SOLVER in Excel, which minimizes the sum of the squares of errors by varying the Thomas model parameters (K_{Th}, q_0). Generally, the nonlinear regression analysis is more effective than the linear regression method in predicting the shape and the behavior of the breakthrough curve, as it will be shown in section 4.4.

3.4.3.2 The error analysis

In order to confirm the goodness of fitting the experimental breakthrough data with Thomas model, it is highly important to analyze the data using error analysis in combination with the values of coefficient of determination (R^2) from the regression analysis. The calculated expressions of some functions are given as follow: [115-118]

I. **The sum of the absolute errors (SAE)**

$$SAE = \sum_{i=1}^{n} |(y_e - y_c)_i| \tag{3.11}$$

II. **The sum of the squares of the error (SSE)**

$$SSE = \sum_{i=1}^{n} (y_e - y_c)_i^2 \tag{3.12}$$

III. **The sum of the relative squares of errors (SRS)**

$$SRS = \sum_{i=1}^{n} (y_e - \bar{y})^2 \tag{3.13}$$

$$\bar{y} = \frac{1}{n} \sum_{i=1}^{n} (y_e)_i \tag{3.14}$$

IV. **Coefficient of determination (R^2)**

$$R^2 = 1 - \frac{SSE}{SRS} \tag{3.15}$$

Where, (n) is the number of experimental data points, (y_c) is the predicted or calculated data with Thomas model and (y_e) is the experimental data point. In the previous equations (3.11 – 3.14), (y) represents the ratio $\frac{C}{C_0}$ or $\ln\left(\frac{C_0}{C} - 1\right)$ in case of nonlinear regression or linear regression analysis, respectively.

3.4.4 Pressure drop across column C-102

The pressure drop across the zeolites column (C-102) was measured by connecting the two ports of the differential pressure manometer [Figure 3.2 (b)] to the top and bottom sampling points of the column (i.e., HA-124 and HA-125) as explained in Figure 3.3. The measured pressure drop shall be compared with the theoretical models proposed for predicting the pressure drop across packed beds. As mentioned thoroughly in the literature review in section 2.5, the pressure drop is calculated from equations that originally established for channel flow.

The model used in calculating or predicting the pressure drop in this study is based on the same criteria of the theoretical models mentioned in section 2.5. However, this model was confirmed by many experimental works to be suitable for calculating the pressure drop through packed beds. The model is given as follow:[92]

$$Re = \frac{V\,D_p\,\rho}{\eta} \tag{3.16}$$

$$\Delta P = \frac{\psi\,H\,\rho\,V^2\,(1-\varepsilon)}{2\,D_p\,\varepsilon^3} \tag{3.17}$$

$$\psi = \frac{320}{Re/(1-\varepsilon)} + \frac{6}{[Re/(1-\varepsilon)]^{0.1}} \tag{3.18}$$

Where (Re) is Reynolds number (dimensionless), (D_p) is the average particle diameter of the adsorbent (m), (ρ) is the density of air (1.2 Kg/m^3), (η) is the dynamic viscosity of air (1.8 x 10^{-5} Kg/s.m), (V) is the superficial velocity of the fluid based on empty tower (m/sec), (ΔP) is the pressure drop across the packing height (Pa), (ψ) is the pressure drop coefficient (dimensionless), (H) is the packing height (m) and (ε) is the bed void fraction.

Equation 3.18 was verified and confirmed by experimental results up to $Re/(1-\varepsilon)$ = 5 x 10^5. Further experimental work indicated that for $Re/(1-\varepsilon)$ > 5 x 10^5 the pressure drop coefficient seems to be independent of Re. Therefore equation 3.18 accounts only for $Re/(1-\varepsilon) \leq$ 5 x 10^5. The first term in the equation represents the asymptotic solution for the laminar flow and the second term represents the asymptotic solution of the turbulent flow. Each term can be written as:

$$\psi = A\,((1-\varepsilon))^n\,Re^{-n} \tag{3.19}$$

Where n = 1 represents the low Re range (i.e., laminar flow) and n = 0.1 accounts for the high Re range (i.e., turbulent flow).

For Re < 1, the flow regime is laminar. For Re > 1000, the flow regime is turbulent. While for $1 \leq Re \leq 1000$, the flow regime falls in the transitional region.

3.4.4.1 Correction of the bed void fraction value

One of the common reasons for the deviation of the predicted or calculated pressure drop values from the measured values is the inaccurate estimation of the bed void fraction value (ε) which has a great influence on predicting reasonable values of the pressure drop. The it can be observed from equations 3.17 and 3.18 that slight variations in the estimation of the (ε) can cause a large change in the predicted ΔP values. The sensitivity of equation 3.18 to the influence of variation in (ε) can be expressed as follow: [92]

$$\frac{d(\Delta P)}{\Delta P} = -\frac{3-\varepsilon(2-n)}{1-\varepsilon}\frac{d\varepsilon}{\varepsilon} \tag{3.20}$$

Where (ΔP) is the measured pressure drop value (i.e., experimental), $d(\Delta P)$ is the difference between the calculated and the measured pressure drop values based on the given void fraction (ε) value, $(d\varepsilon)$ is the difference between the actual and the given void fraction value and (n) is the slope of Reynolds number, where it is equivalent to 1 in case of laminar flow, or 0.1 in case of turbulent flow.

The negative sign in equation 3.20 indicates that negative variations in the estimation of ε causes positive variations in estimated or predicted pressure drop value. Which means that if the given ε lower than the actual or the true value, the predicted pressure drop will higher than the measured values and vice versa.

4   Results & Discussion

In this chapter we will present the calculations obtained during the experimental work such as: the breakthrough time at each run, the adsorption capacity, the efficiency of the packed bed column, parameters used for fitting the breakthrough curve with Thomas model and the pressure drop along the zeolite column. Moreover, these results will be discussed, explained, and compared to the theoretical models in order to have a better understanding for the process and to investigate which parameters can have a great effect for optimizing the process.

4.1   Effect of flowrate on the breakthrough curve

The influence of varying the flowrate on the behavior of the breakthrough curve and the adsorption response was investigated by employing three different adsorbents (MSC-542, MSC-544, SP-564). This influence is depicted in Figure 4.1 (a, b, and c) under constant conditions of bed temperature at 19℃ , inlet CO_2 concentration (400 ppm) and operating pressure (1 bar). The data were collected for three different flowrates at 25.3, 31.6, and 38 m^3/hr which are equivalent to superficial velocities of 0.2, 0.25, and 0.3 m/s, respectively.

As shown in Figure 4.1(c), on SP- 564, the breakthrough time was achieved after 7.4 hrs at flowrate of 25.3 m^3/hr, while the breakthrough time decreased to 4.8 and 3.5 hrs with increasing the flowrate to 31.6 and 38 m^3/hr, respectively. The adsorbents MSC-542, and MS-544 followed the same trend. As the breakthrough time for MSC-542 (Figure 4.1(b)) was 7.5, 6.16, and 4.5 hrs at flowrates of 25.3, 31.6 and 38 m^3/hr, respectively. While for MSC-544, the breakthrough time was attained at 11.6, 9, and 7.4 hrs at flowrates of 25.3, 31.6 and 38 m^3/hr, respectively (Figure 4.1(a)).

As a conclusion, as the flowrate increases (i.e., superficial velocity increases) the breakthrough time reduced, and equilibration occurs faster. This is due to the increase in the mass transfer and diffusion rate which leads to faster saturation [119]. However, increasing the flow rate or the superficial velocity leads to reduction in the adsorption capacity and lower the removal efficiency which will be discussed in the next section. Also, it can be observed from Figure 4.1 that for the same adsorbent, as the flowrate decreases, the breakthrough curve becomes steeper which is an indication of higher removal efficiency and is related to the mass transfer zone width.

(a)

(b)
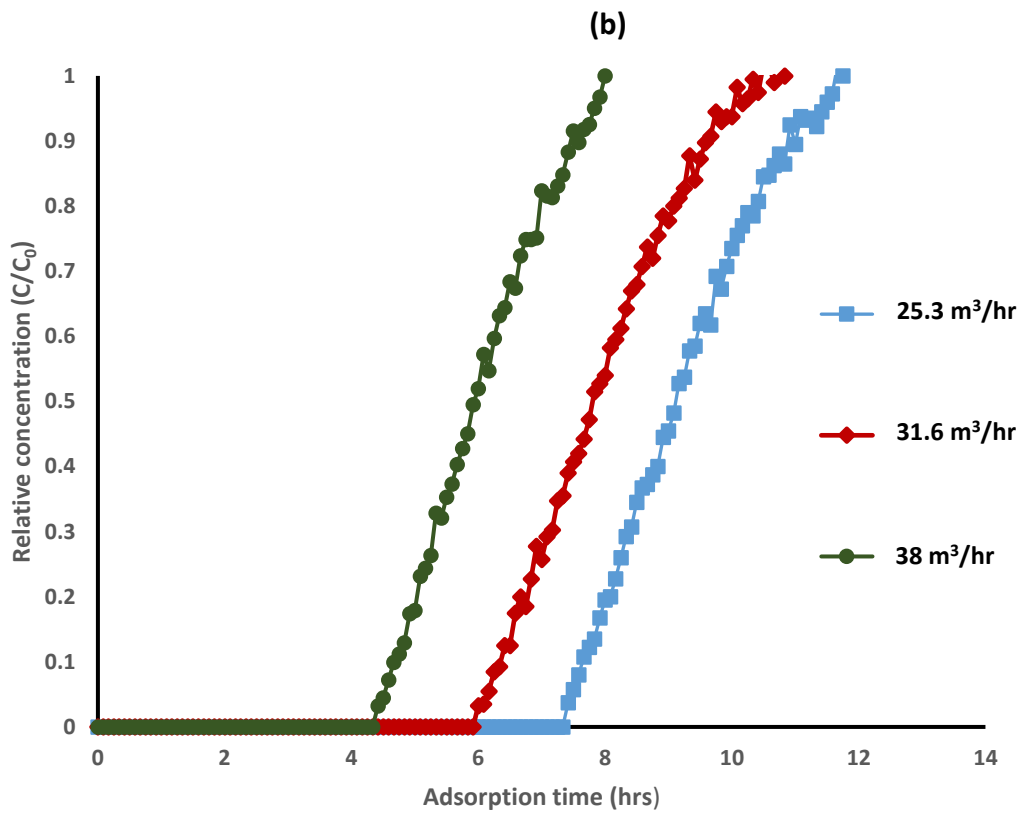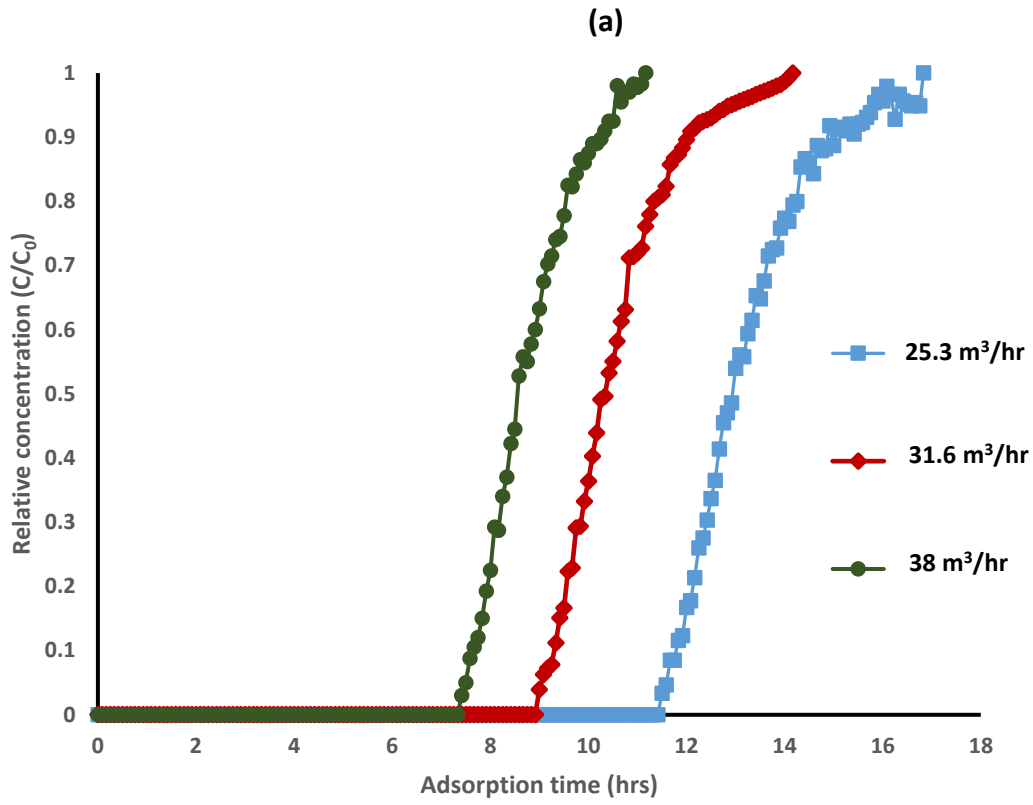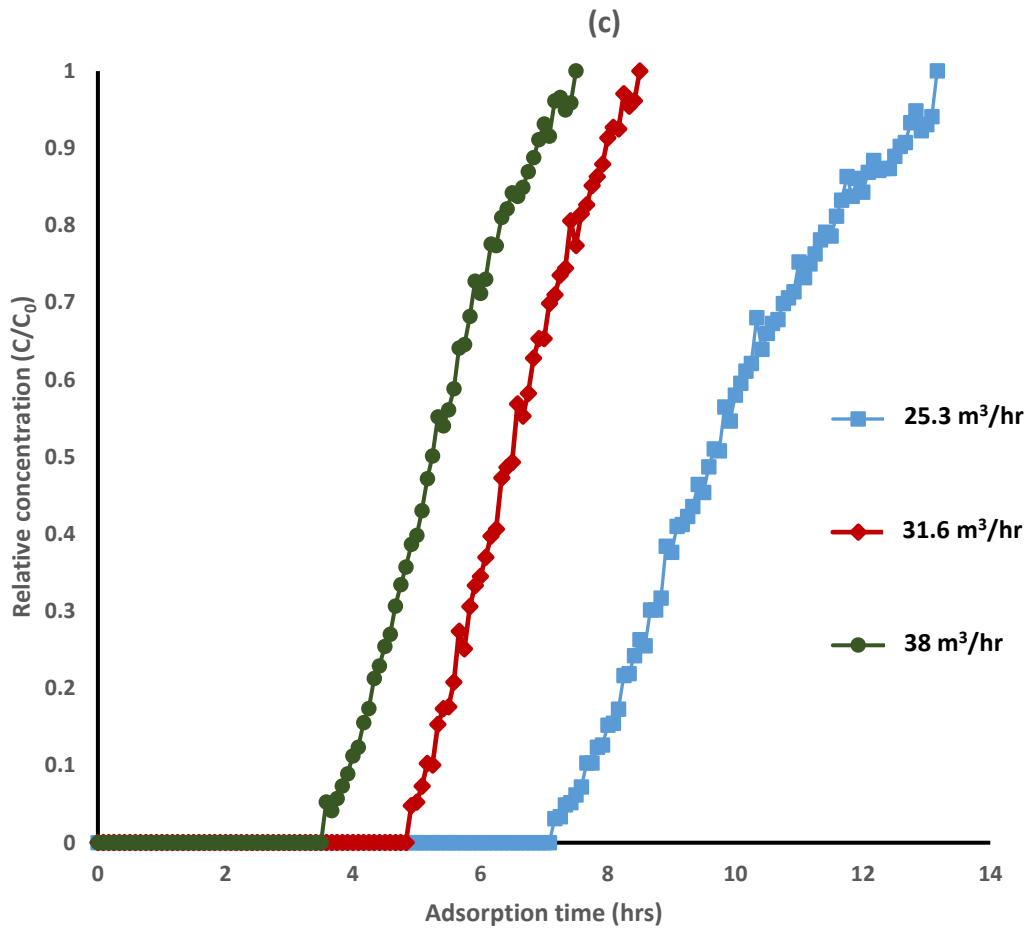
**Figure 4.1 Effect of varying the flowrate on the breakthrough curve at T = 19℃ , C_0 = 400 ppm
(a) MSC-544 (b) MSC-542 (c) SP-564**

It should be noted that the breakthrough curves typify S-shaped curve in an ordinary adsorption process. However, it can be observed that there are some fluctuations in the slope of the breakthrough curves presented in Figure 4.1. Such fluctuations are related to changes in the operating conditions of the experiments, that causes the S-shaped curve to become nearly a vertical line and decreases the saturation time. Generally, those variations have a small effect on the results. Therefore, we will disregard this effect for simplicity.

4.2   Adsorption capacity and column efficiency

Table 4.1 summarizes the parameters used for calculating the adsorption capacity of each adsorbent, and the efficiency of the column based on the length of the mass transfer zone and the portion of the unused bed for each run.

Table 4.1 Experimental conditions and results obtained from breakthrough curves analysis

Adsorbent	Mass of adsorbent (kg)	pressure (bar)	Temp. (°C)	C_0 (ppm)	H (m)	Q (m³/hr)	t_b (hr)	t_{st} (hr)	q (g CO_2/kg zeolite)	L_{MTZ} (M)	H_{UNB} (m)	η (%)
MSC-544	8.318	1	19	430	0.35	25.3	11.6	13.21	31.5	0.045	0.043	87.81
		1	19	420	0.35	31.6	9	10.54	30.66	0.055	0.051	85.39
		1	19	400	0.35	38	7.4	8.9	29.2	0.059	0.055	83.15
MSC-542	7.872	1	19	450	0.35	25.3	7.5	9.21	24.28	0.072	0.065	81.43
		1	19	400	0.35	31.6	6.16	7.9	23.12	0.086	0.077	77.97
		1	19	400	0.35	38	4.5	6.03	21.21	0.102	0.089	74.63
SP-564	7.564	1	19	395	0.35	25.3	7.3	9.85	23.72	0.099	0.087	74.13
		1	19	435	0.35	31.6	4.8	6.52	21.61	0.106	0.092	73.62
		1	19	420	0.35	38	3.5	5.34	20.52	0.146	0.121	65.54

4.2.1 Effect of flowrate on the adsorption capacity

As it can be observed from Table 4.1 the adsorption capacity decreases with increasing the flowrate. This could be explained by the fact that, increasing the flowrate will increase the superficial velocity of the adsorbate which leads to insufficient residence time between the adsorbate and the adsorbent. So, the adsorbate (CO_2) will not have enough time to diffuse between the pores and the channels of the zeolite. Consequently higher flowrate gives rise to faster saturation, which represents reduction in the capacity [120]. This effect is crucial for evaluating the bed efficiency and the mass transfer zone.

By decreasing the flowrate from 38 m³/hr to 25.3 m³/hr, the adsorption capacity of MSC-544 increases from 29.2 to 31.5 g/kg (9 % increase), while, for MSC-542 the adsorption capacity increases from 21.21 to 24.28 g/kg (15% increase), and for SP-564, the adsorption capacity increases from 20.52 to 23.72 g/kg (16% increase). Therefore, it can be deduced that the effect of lowering the flowrate on the adsorption capacity increases as the particle diameter increases (i.e., the percentage of increase in the adsorption capacity is the highest for SP-564). Since the capacity of the larger diameter zeolite is already low due to lower surface area, the effect of varying the flowrate is more significant. The effect for varying the flowrate is graphically represented in Figure 4.2.
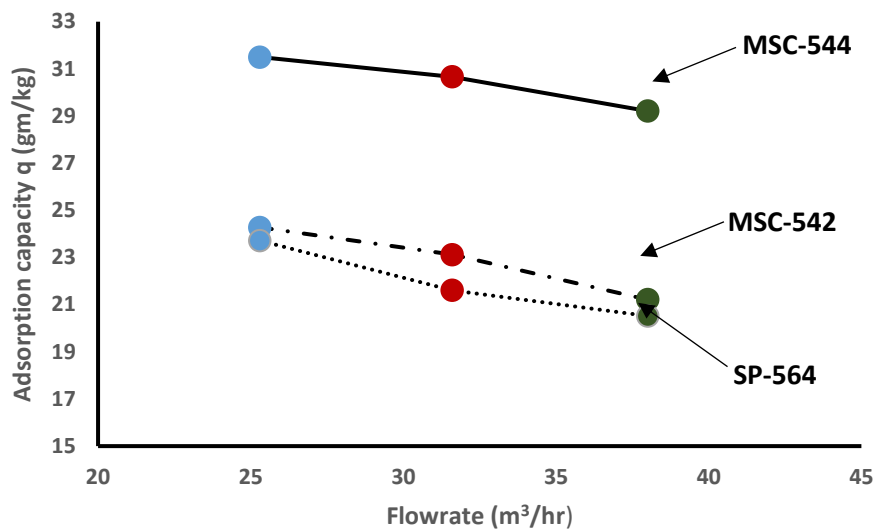
Figure 4.2 Effect of flowrate on the adsorption capacity

4.2.2 Effect of the particle diameter on the adsorption capacity

It is obviously shown in Table 4.1 that for the same flowrate, as the particle diameter decreases the adsorption capacity increases. Decreasing the particle diameter increases the surface area (i.e., more adsorption sites are available for the adsorbate), therefore the adsorption capacity increases. This effect is depicted in Figure 4.3.

For instance, if flowrate of 38 m^3/hr is considered, as the particle diameter decreases from 0.006 m (i.e., SP-564) to 0.00205 m (i.e., MSC-544), the adsorption capacity increases from 20.52 to 29.2 g/kg which represents 42.3% increase in the capacity. Therefore, we can conclude that the effect of decreasing the particle diameter is larger than the effect of decreasing the flowrate on the adsorption capacity (based on the operating flowrates).
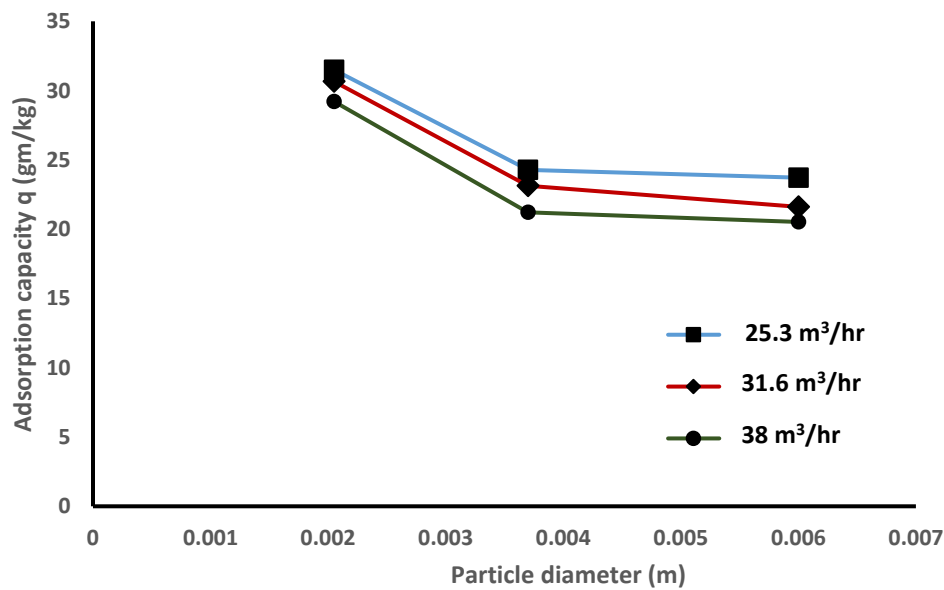
Figure 4.3 Effect of particle diameter on the adsorption capacity

49

4.2.3 The effect of flowrate on the column efficiency

It can be observed from Table 4.1 that the length of the unused bed (H_{UNB}) decreases as the flowrate decreases. Also, the efficiency of the bed capacity (η) increases as the flowrate decreases. Basically, the H_{UNB} is related to the width of the mass transfer zone (L_{MTZ}) which is mainly dependent on the superficial velocity (i.e., flowrate). As the flowrate decreases, the mass transfer zone becomes narrower (i.e., L_{MTZ} becomes smaller) and most of the bed capacity is utilized at the breakthrough point. This is an indication of efficient utilization of the bed capacity which in turn enhances the bed efficiency. Therefore, prolonged breakthrough time at lower flowrates, means smaller mass transfer zone, and consequently reduces the portion of the unused bed length (i.e., higher efficiency). The effect of flowrate on both H_{UNB} and bed efficiency is illustrated in Figure 4.4.
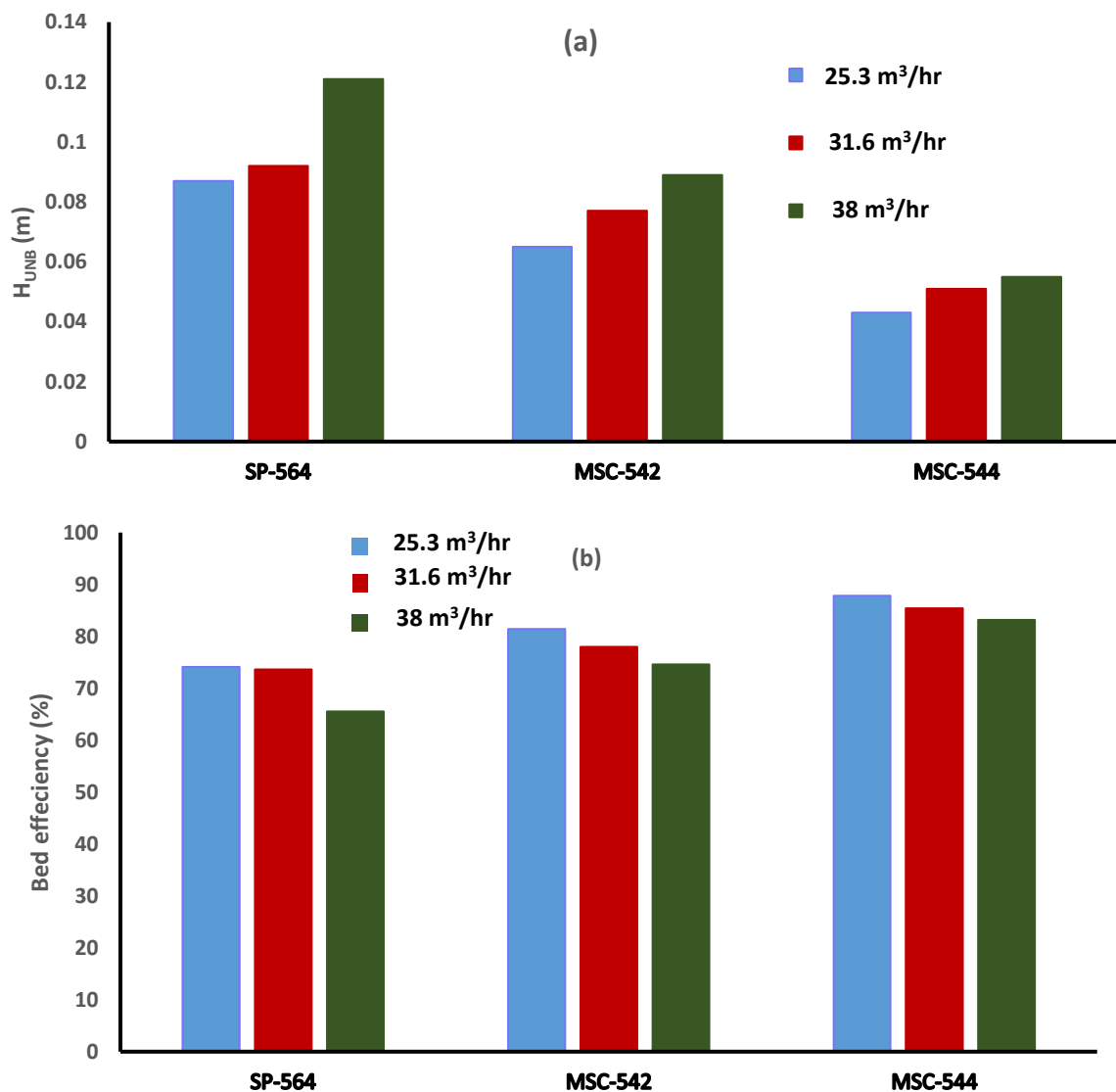
Figure 4.4 Effect of flowrate on (a) the unused bed length (b) bed efficiency

4.3   Optimizing the bed capacity by varying the flowrate

The purpose of this section is to find an optimized solution to reach the higher capacities of the adsorbents used at lower flowrates (i.e., 31.6 and 25.3 m^3/hr) in a shorter time. In other words, it means that during the same experimental run the flowrate will be changed. At the beginning of the run, we will start with the highest flowrate of 38 m^3/hr in order to take the advantage of high diffusion (i.e., to use part of the bed capacity in short time). Prior to the breakthrough time of this flowrate, which is already known from table 4.1, the flowrate will be reduced either to 31.6 or 25.3 m^3/hr. This will allow the process to continue as the equilibrium will be shifted due to the increase in the time contact between the adsorbent and the adsorbate. This strategy was implemented for the three adsorbents employed in the project.

It should be noted that at each time the flowrate was changed 0.5 hour earlier prior to the breakthrough of the flowrate 38 m^3/hr, to avoid the effect of slight variations in the operating conditions during different runs on the breakthrough time.

For MSC-542 and MSC-544, it was chosen to vary the flowrate from 38 to 31.6 m^3/hr as the corresponding adsorption and breakthrough time for those adsorbents is relatively long. Also, there is no significant increase in the adsorption capacity when the flowrate decreases from 31.6 to 25.3 m^3/hr. For SP-564, it was chosen to vary the flowrate from 38 to 25.3 m^3/hr as the breakthrough time for this adsorbent is relatively low.
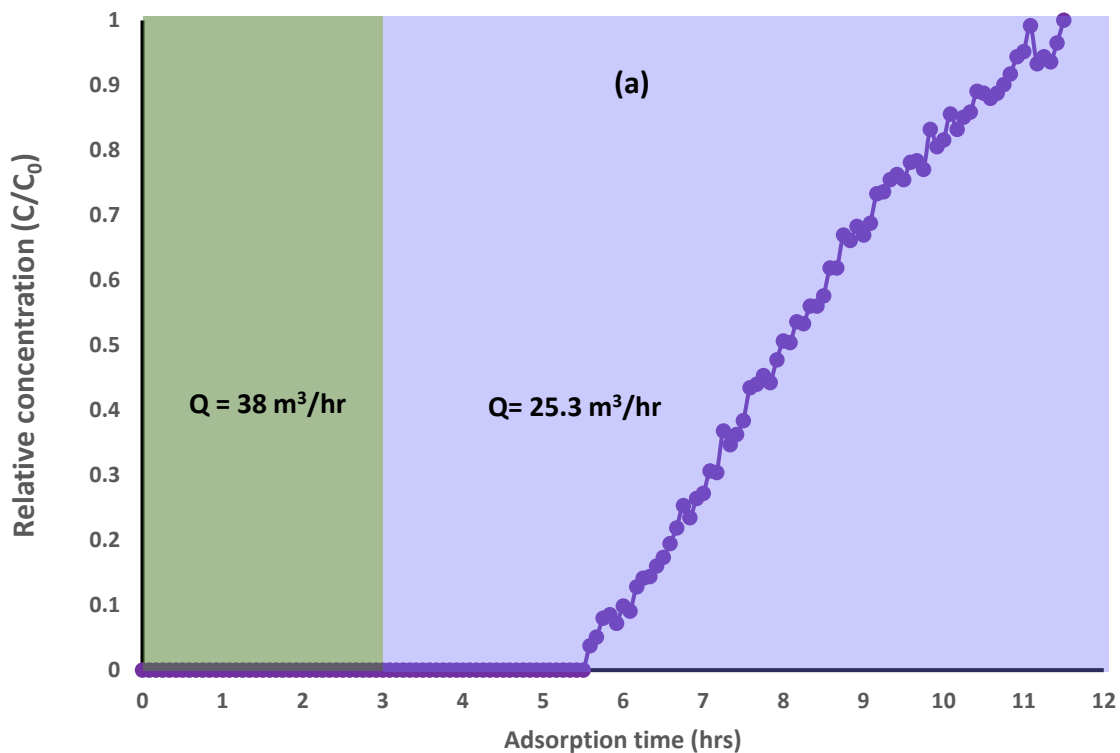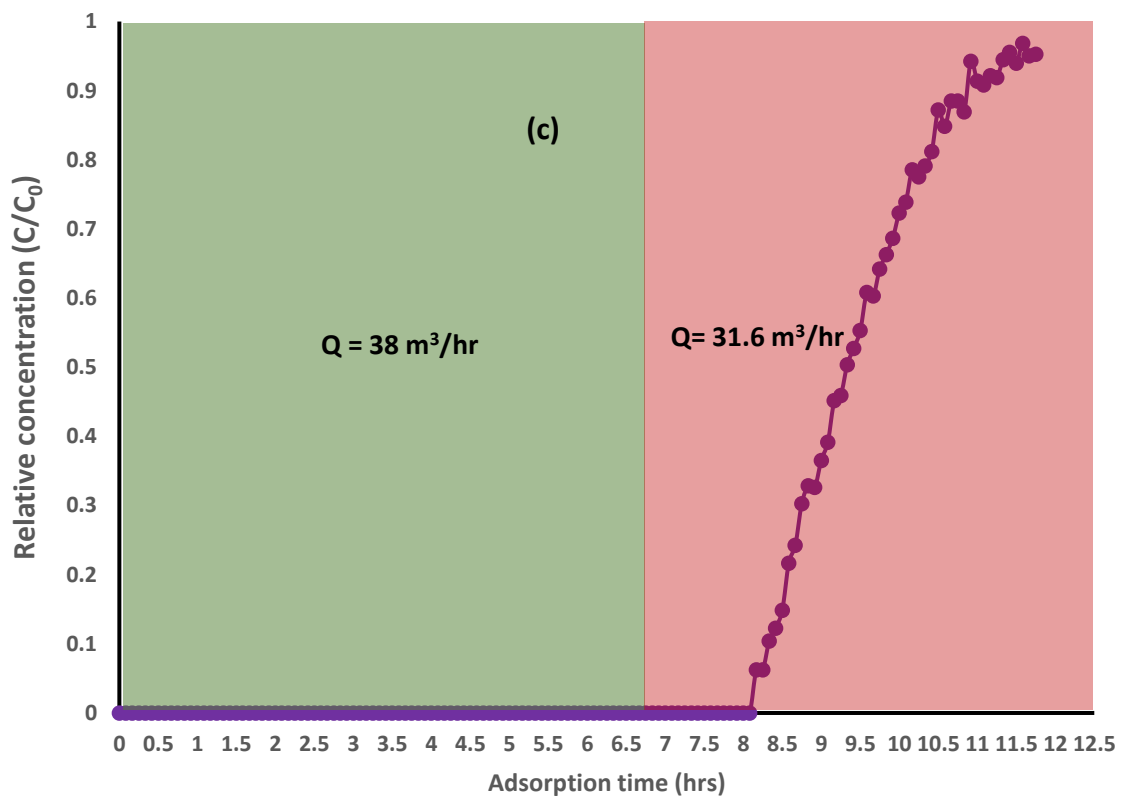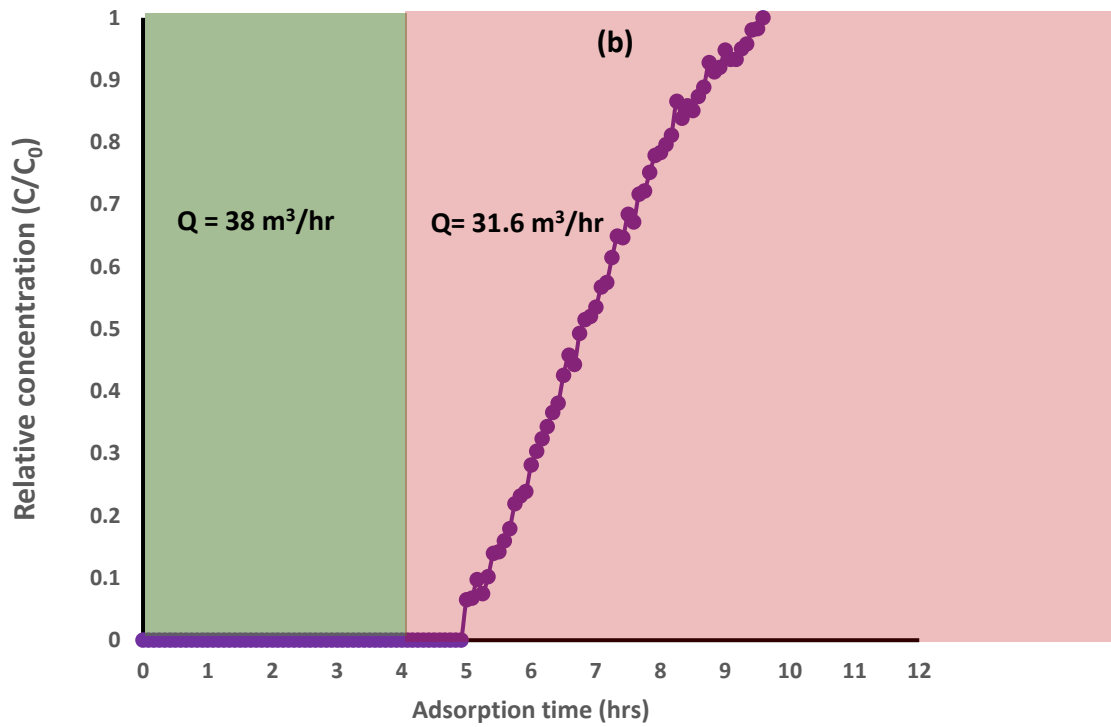
Figure 4.5 Optimizing the bed capacity by varying the flowrate (Co = 400 ppm, T = 19℃) (a) SP-564 (b) MSC-542 (c) MSC-544

For SP-564, the flowrate was changed from 38 to 25.3 m^3/hr after 3 hours as shown in Figure 4.5(a), because the breakthrough time corresponding to 38 m^3/hr was around 3.5 hrs. It was observed that the adsorption capacity at flowrate of 25.3 m^3/hr (23.7 g/kg) could be reached in shorter time, as the breakthrough time at this mixed flowrate strategy reduced to 5.6 hr instead of 7.3 hr, in case of running the adsorption cycle with constant flowrate of 25.3 m^3/hr. Therefore, it can be concluded that the high capacity corresponding to flowrate of 25.3 m^3/hr could be reached by saving the adsorption time by around 1.7 hr,

For MSC-542, the flowrate was changed from 38 to 31.6 m^3/hr after 4 hrs as shown in Figure 4.5(b). The adsorption capacity was found to be 22.6 g/kg which represents almost 98% of the adsorption capacity of MSC-542 at flowrate 31.6 m^3/hr (23.12 g/kg). The breakthrough time was reduced to 4.9 hrs instead of 6.16 hr in case of running the cycle with constant flowrate of 31.6 m^3/hr. It should be noted that theoretically, the adsorption capacity at flowrate 31.6 m^3/hr (23.12 g/kg) should be reached if the same operating conditions are maintained. However, this slight reduction in the capacity is contributed to slight variations in the operating conditions such as slight increase in temperature, relative humidity, or initial concentration.

while for MSC-544, the same procedure was carried out by varying the flowrate from 38 to 31.6 m^3/hr after 6.75 hrs as shown in Figure 4.5(c). Almost the same adsorption capacity at flowrate of 31.6 m^3/hr could be achieved with reduced breakthrough time after 8 hrs instead of 9 hrs (Table 4.2).

Consequently, varying the flowrate during the same run seems to be effective for optimizing the bed capacity and saving the adsorption cycle time, as summarized in Table 4.2. However, the effect of the pressure drop will play an important role in the optimization of the bed capacity, as the pressure drop increases by increasing the flowrate.

Table 4.2 Comparison between the adsorption time for varying the flowrate and keeping the flowrate constant

Adsorbent	Constant flowrate			Optimized flowrate			Time saved (hr)
	Q (m³/hr)	t_b (hr)	q (gm/kg)	Q (m³/hr)	t_b (hr)	q (gm/kg)	
SP-564	25.3	7.3	23.72	38 → 25.3	5.6	23.72	1.7
MSC-542	31.6	6.16	23.12	38 → 31.6	4.9	22.6	1.26
MSC-544	31.6	9	30.66	38 → 31.6	8	30.2	1

4.4   Breakthrough curve fitting by Thomas model

The verification of the breakthrough curves data was implemented by the application of dynamic Thomas model. The model parameters estimated from Eq. 3.9 and 3.10, as well as the values of R^2 by linear and nonlinear regression analysis are listed in Table 4.3 and 4.4, respectively.

It can be concluded from Table 4.3 and 4.4 that, as the flowrate increases the value of q_0 calculated from Thomas model decreases while the value of K_{TH} increases. This trend is the same for linear and nonlinear regression analysis methods.

Generally, both the linear and nonlinear regressive models can be considered as suitable for simulating the dynamic behavior of the fixed bed column of zeolite with respect to change in the flowrate. As the calculated adsorption capacity from Thomas model (q_0) was found to be in a close concurrence with that obtained from the experimental breakthrough data ($q_{experimental}$), as given in Table 4.3 and 4.4. Also, the value of R^2 obtained from nonlinear regressive model was higher than that from linear, which is indication for the effectiveness of the nonlinear regression analysis for predicting the dynamic behavior of CO_2 adsorption on zeolites 13X in response to variation of the flowrate. This conclusion is in accordance with previous work reported in the literature [121, 122].

Even though both models can predict well the adsorption capacity of the zeolite, the linear regressive model is not able to describe all the data for predicting the shape and the behavior of the breakthrough curve, especially the points before the breakthrough time which give undefined values on plotting the linearized form of Thomas model (i.e., Eq. 3.9), as shown in Figures 4.6. While the nonlinear model of Thomas model as given in Eq. 3.10 could predict the shape of the breakthrough curve as shown in Figures 4.7.

Moreover, it can be observed from Tables 4.3 and 4.4 that generally for both models, R^2 increases as the flowrate increases. This behavior could be related to the fact that, at higher flowrates the no. of the data points is less than that at lower flowrates as the adsorption cycle time decreases with increasing the flowrate. Therefore, the probability of fitting the experimental points to the predicted points by Thomas model will be higher.

Table 4.3 Model parameters by linear regression analysis with Thomas model

Adsorbent	Q (m³/hr)	C_o (gm/m³)	K_{TH} (m³/gm.hr)	q_0 calculated (gm CO_2/kg zeolite)	$q_{experimental}$ (gm CO_2/kg zeolite)	R^2
MSC-544	25.3	0.7839	1.427	31.498	31.5	0.9341
	31.6	0.7657	1.687	30.660	30.66	0.9666
	38	0.7292	2.396	29.260	29.2	0.9723
MSC-542	25.3	0.8203	1.621	24.259	24.28	0.9822
	31.6	0.7292	1.964	23.096	23.12	0.9607
	38	0.7292	2.141	21.512	21.21	0.9762
SP-564	25.3	0.7201	1.276	23.870	23.72	0.9694
	31.6	0.7930	2.003	21.590	21.61	0.9815
	38	0.7657	2.120	19.330	20.52	0.9867

Table 4.4 Model parameters by nonlinear regression analysis with Thomas model

Adsorbent	Q (m³/hr)	C_o (gm/m³)	K_{TH} (m³/gm.hr)	q_0 calculated (gm CO_2/kg zeolite)	$q_{experimental}$ (gm CO_2/kg zeolite)	R^2
MSC-544	25.3	0.7839	1.805	31.160	31.5	0.995132
	31.6	0.7657	2.047	30.358	30.66	0.996584
	38	0.7292	4.975	27.712	29.2	0.999828
MSC-542	25.3	0.8203	1.619	24.170	24.28	0.99565
	31.6	0.7292	1.816	23.040	23.12	0.99629
	38	0.7292	2.084	21.100	21.21	0.9947
SP-564	25.3	0.7201	1.282	23.526	23.72	0.993472
	31.6	0.7930	1.933	21.548	21.61	0.9954
	38	0.7657	1.950	20.420	20.52	0.996237

4.4.1 Linear regression analysis of Thomas model

(a)

Legend:
- ■ 25.3 m³/hr
- ◆ 31.6 m³/hr
- ● 38 m³/hr
- – – – Linear regression analysis

$y = -1.747x + 15.346$
$R^2 = 0.9723$

$y = -1.2917x + 13.616$
$R^2 = 0.9666$

$y = -1.1187x + 14.779$
$R^2 = 0.9341$

Y-axis: $\ln(C_0/C - 1)$
X-axis: Time (hr)

(b)

Legend:
- ■ 25.3 m³/hr
- ◆ 31.6 m³/hr
- ● 38 m³/hr
- – – – Linear regression analysis

$y = -1.5614x + 9.4334$
$R^2 = 0.9762$

$y = -1.4319x + 11.298$
$R^2 = 0.9607$

$y = -1.3299x + 12.237$
$R^2 = 0.9822$

Y-axis: $\ln(C_0/C - 1)$
X-axis: Time (hr)
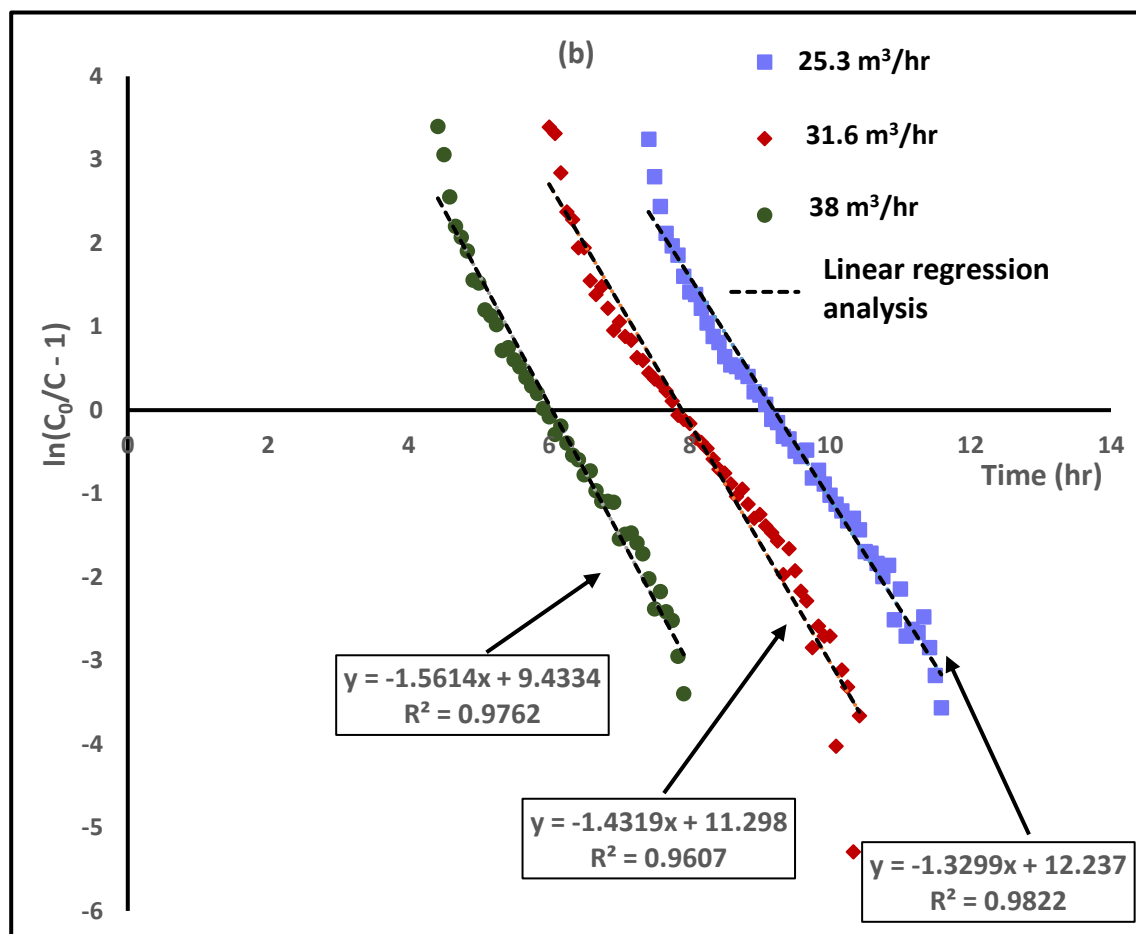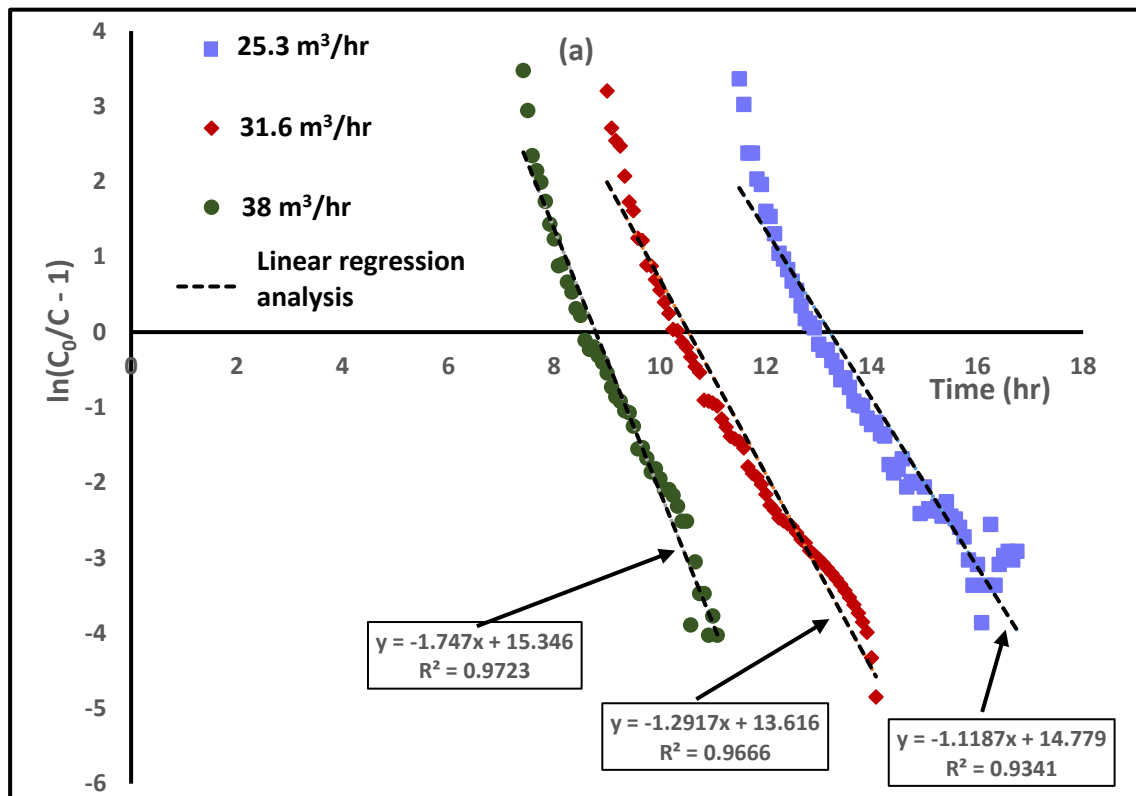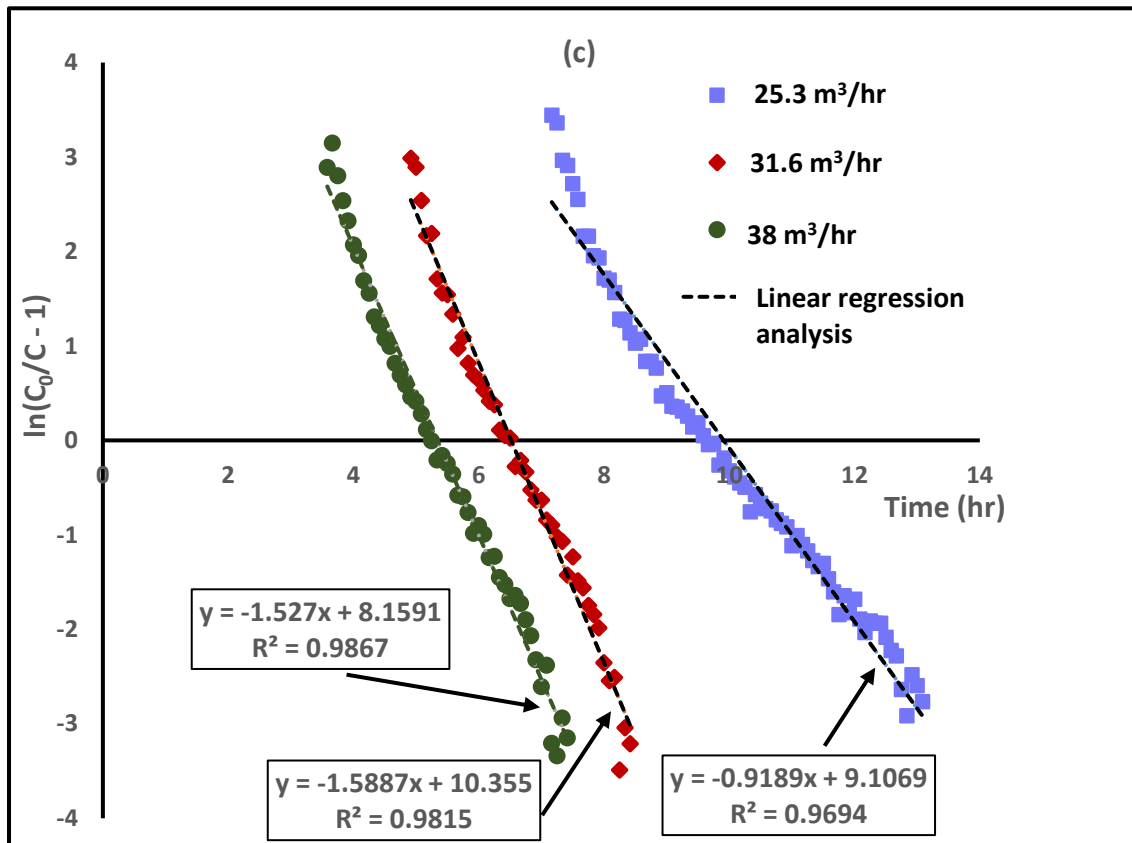
Figure 4.6 Linearized form of Thomas model plots for the adsorption of CO_2 on (a) MSC-544 (b) MSC-542 (c) SP-564

The equations shown in plot (c):

$$y = -1.527x + 8.1591 \quad R^2 = 0.9867$$

$$y = -1.5887x + 10.355 \quad R^2 = 0.9815$$

$$y = -0.9189x + 9.1069 \quad R^2 = 0.9694$$

4.4.2 Nonlinear regression analysis of Thomas model

Figure 4.7 Breakthrough curves of CO₂ adsorption associated with Thomas model nonlinear fitting (a) MSC-544 (b)MSC-542 (c) SP-564

4.4.3   Error estimation of regression analysis

Tables 4.5 and 4.6 consider the error estimation for both linear and nonlinear regression methods respectively, using the least square method. Basically, a good fitting between the experimental breakthrough curves data and Thomas model has a low SAE, and low ratio of SSE/SRS (i.e., high R^2 value).

Table 4.5 Error analysis for linear regression method

Adsorbent	Q (m³/hr)	C_0 (gm/m³)	SAE	SSE	SRS	R^2
	25.3	0.7839	22.89616	13.38111	203.0518	0.9341
MSC-544	31.6	0.7657	18.2386	7.959048	238.2949	0.9666
	38	0.7292	10.88416	4.589767	165.6956	0.9723
	25.3	0.8203	8.42325	2.46039	138.376	0.9822
MSC-542	31.6	0.7292	13.70443	7.6463	194.068	0.9607
	38	0.7292	8.23368	2.7288	114.656	0.9762
	25.3	0.7201	15.74629	5.757634	188.158	0.9694
SP-564	31.6	0.7930	7.52294	2.19166	118.468	0.9815
	38	0.7657	7.555237	1.891479	142.2165	0.9867

Table 4.6 Error analysis for nonlinear regression method

Adsorbent	Q (m³/hr)	C_0 (gm/m³)	SAE	SSE	SRS	R^2
	25.3	0.7839	2.91375	0.126502	25.98904	0.995132
MSC-544	31.6	0.7657	2.341209	0.086256	25.24784	0.996584
	38	0.7292	5.52775	0.002866	16.643388	0.999828
	25.3	0.8203	1.94669	0.07002	16.0982	0.99565
MSC-542	31.6	0.7292	1.95167	0.065832	17.7634	0.99629
	38	0.7292	1.65766	0.05846	11.17911	0.9947
	25.3	0.7201	3.152206	0.120196	18.41163	0.993472
SP-564	31.6	0.7930	1.562145	0.0531	11.5555	0.9954
	38	0.7657	1.459326	0.041288	10.9733	0.996237

4.5 Pressure drop across the zeolite column

Table 4.7 summarizes the operational parameters used for calculating the pressure drop by substitution in Eq. 3.17 based on the given void fraction value ($\varepsilon = 0.4$). Without making correction to this value, the percentage of error between the measured and the predicted values was found to be high as shown in Table 4.7.

Table 4.7 Operational parameters used for calculating the pressure drop without correcting the given void fraction (ε)

Adsorbent	V (m/sec)	D_p (m)	H (m)	η_{air} (kg/sec.m)	ρ_{air} (kg/m³)	Re	ε	ψ	$\Delta P_{calculated}$ (KPa)	$\Delta P_{measured}$ (KPa)	% Of error $\left\lceil \dfrac{d(\Delta P)}{\Delta P} \right\rceil$	Average % of error
	0.2					27.33		11.12	0.427	0.276	-54.71%	
MSC-544	0.25	0.00205	0.35	1.8 x 10⁻⁵	1.2	34.17	0.4	9.62	0.578	0.355	-62.82%	-61.65%
	0.3					41		8.62	0.745	0.445	-67.42%	
	0.2					50		7.67	0.162	0.125	-29.6%	
MSC-542	0.25	0.00375	0.35	1.8 x 10⁻⁵	1.2	62.5	0.4	6.84	0.225	0.175	-28.29	-29.43%
	0.3					75		6.26	0.296	0.227	-30.40	
	0.2					80		6.08	0.079	0.054	-46.3%	
SP-564	0.25	0.006	0.35	1.8 x 10⁻⁵	1.2	100	0.4	5.52	0.113	0.072	-56.94%	-50.27%
	0.3					120		5.13	0.152	0.103	-47.57%	

4.5.1 Sensitivity of the pressure drop due to variations in the void fraction

It can be observed from Table 4.7, that there is a large deviation between the measured and the calculated pressure drop values. This behavior is due to inaccurate estimation of the void fraction (ε), which is one of the common problems that causes a severe departure of the predicted ΔP values from the experimental results. By looking into Eq. 3.17 it can be deduced that a small variation in (ε) can lead to very large effect on ΔP, which makes it difficult to predict the pressure drop accurately.

Also, it can be expected from the -ve sign of the % of error between the measured and predicted ΔP values, that the actual value (ε) is higher than the given value ($\varepsilon = 0.4$). As, when the given value of the void fraction is lower than the actual value, the predicted ΔP value will be overestimated and higher than the experimental ones and that will lead to -ve % of error $\left(\Delta P \propto \dfrac{1}{\varepsilon} \right)$.

So, positive variations in ε lead to negative variations in the pressure drop. Therefore, the given value of ε =0.4 was corrected and correlated by using Eq.3.20. That was carried out by substituting into Eq. 3.20 with n = 1 (asymptotic solution for laminar flow), and n = 0.1 (asymptotic solution of turbulent flow, as the flow falls in the transitional region, then taking the average value of ε in order to have accurate estimation for the void fraction value.

As shown in Table 4.8, the predicted values are in a good match with the experimental ones when the void fraction values are corrected, compared to the obtained results in Table 4.7. Moreover, this verifies the reliability and the accuracy of employing Eq.3.20 for correcting the value of (ε).

Table 4.8 Operational parameters used for calculating the pressure drop after correcting the given void fraction value

Adsorbent	V (m/sec)	D_p (m)	H (m)	η_{air} (kg/sec.m)	ρ_{air} (kg/m^3)	Re	ε	ψ	$\Delta P_{calculated}$ (KPa)	$\Delta P_{measured}$ (KPa)	% Of error $\left[\left\|\dfrac{d(\Delta P)}{\Delta P}\right\|\right]$	Average % of error
MSC-544	0.2	0.00205	0.35	1.8 x 10^{-5}	1.2	27.33	0.4543	10.45	0.294	0.276	+ 9.78%	+ 5.38%
	0.25					34.17		9.08	0.338	0.355	+ 4.79%	
	0.3					41		8.15	0.438	0.445	+ 1.57%	
MSC-542	0.2	0.00375	0.35	1.8 x 10^{-5}	1.2	50	0.4292	7.49	0.121	0.125	+ 3.2%	+ 2.79%
	0.25					62.5		6.67	0.169	0.175	+ 3.4%	
	0.3					75		6.12	0..223	0.227	+ 1.76%	
SP-564	0.2	0.006	0.35	1.8 x 10^{-5}	1.2	80	0.4459	5.87	0.051	0.054	+ 5.56%	+ 4.37%
	0.25					100		5.34	0.070	0.072	+ 2.78%	
	0.3					120		4.98	0.098	0.103	+ 4.76%	

Figure 4.8 illustrates the sensitivity of the pressure drop to the changes in ε by plotting the actual values of ε for the three adsorbents (0.4543, 0.4292, and 0.4459 for MSC-544, MSC-542, and SP-564 respectively) on the x-axis against the absolute ratio of the error in the pressure drop to the error in the void fraction $\left(\dfrac{d(\Delta p)/\Delta p}{d\varepsilon/\varepsilon}\right)$. Which gives an indication on how the pressure drop will vary and deviate due to inaccurate estimation for the void fraction (ε)

It can be concluded from Figure 4.8 that as the void fraction increases, the sensitivity of the pressure drop due to variations in the void fraction increases. The trend of the graph was in a accordance with the results from [92].

ε	$\dfrac{d(\Delta p)/\Delta p}{d\varepsilon/\varepsilon}$
0.4292	4.325
0.4459	4.88
0.4543	5.15
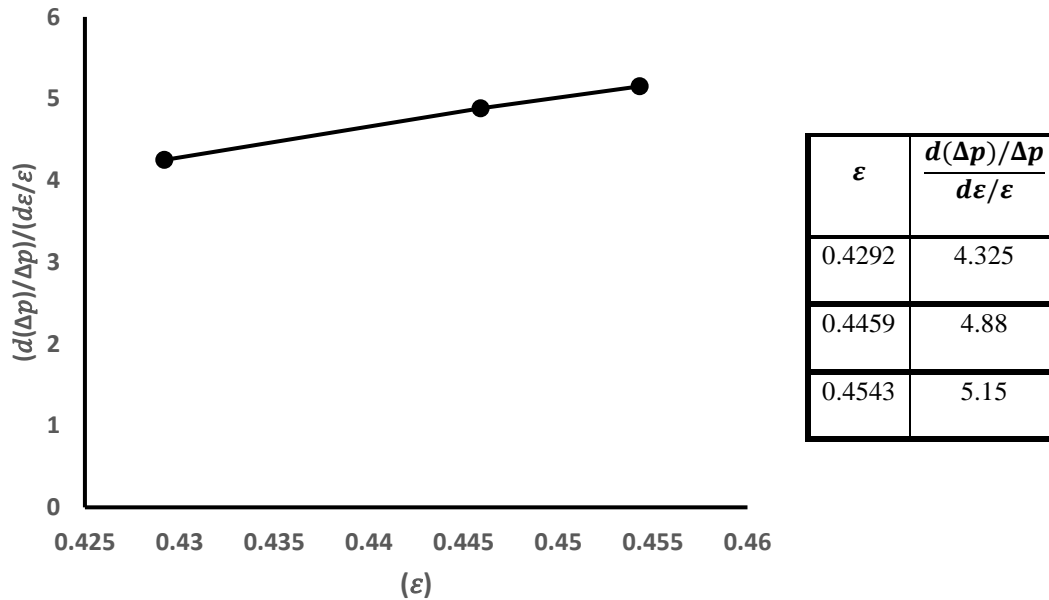
Figure 4.8 Sensitivity of the pressure drop due to variations in the void fractions for zeolite 13X ($\varepsilon_{MSC\text{-}544} = 0.4543$, $\varepsilon_{MSC\text{-}542} = 0.4292$, $\varepsilon_{SP\text{-}564} = 0.4459$)

4.5.2   Effect of flowrate on the flow regime

It is shown from Table 4.8, that the flow regime for all the experimental runs at flowrates of 25.3, 31.6, and 38 m^3/hr falls in the transitional region, as the Reynolds no. for all the experimental runs falls in the range of 1< Re <1000. Thus, the flow has both characteristics of laminar and turbulent flow. Which indicates that the pressure loss is due to both viscous loss and kinetic energy loss (inertial effects). The kinetic energy loss is essentially caused by the changes in channel cross section and flow direction, as most of the kinetic energy of the fluid is lost in the form of expansion loss.[60]

4.5.3   Effect of the flowrate on the pressure drop

It can be deduced from Table 4.8, that the pressure drop for the same adsorbent increases as the flowrate increases. This is due to the fact that, as the flowrate increases, the superficial velocity increases and the drag forces (i.e., resistance to the flow) increases, thus separation occurs [123].Therefore, by increasing the superficial velocity, the inertial effects increase, and the pressure drop increases.

By increasing the superficial velocity from 0.2 to 0.3 m/sec, the pressure drop for MSC-544 increased from 0.276 to 0.445 KPa (i.e., 61.2% increase). While for MSC-542, the ΔP increases from 0.125 to 0.227 KPa (i.e., 81.6% increase), and for SP-564, the pressure drop increases from 0.054 to 0.103 KPa (i.e., 90.7% increase). The effect of the flowrate on the pressure drop is represented graphically in Figure 4.9.
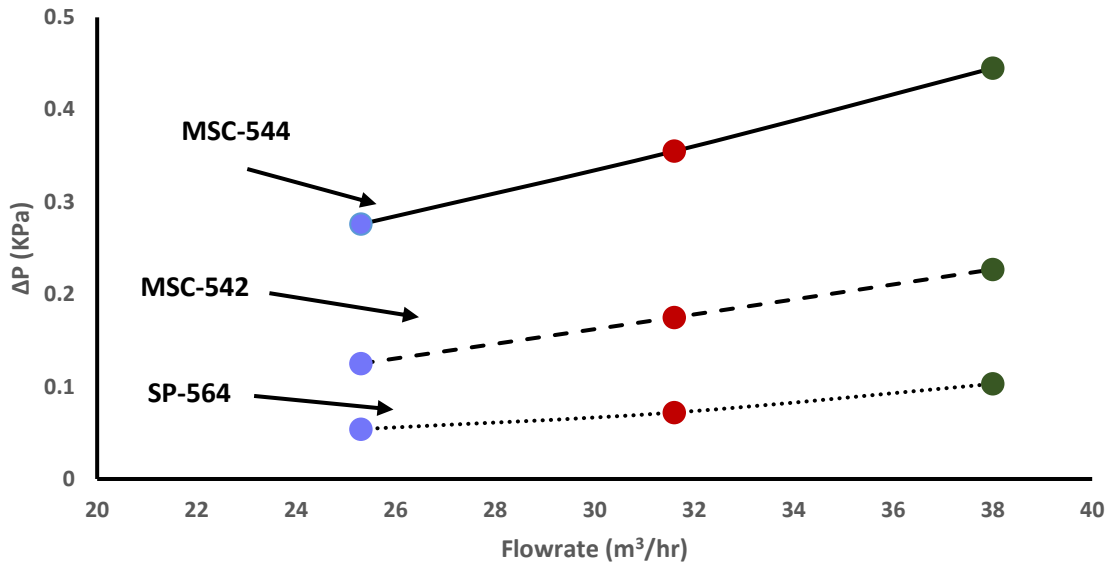
Figure 4.9 Effect of flowrate (superficial velocity) on the pressure drop

4.5.4 Effect of the particle diameter on the pressure drop

Table 4.8 indicates that for the same superficial velocity, a decrease in the particle diameter causes an increase in pressure drop. This is due to the fact that when the particle diameter decreases, the specific surface area increases, so the resistance to the flow of the fluid increases, which consequently increases the pressure drop [124].

If the flowrate of 25.3 m^3/hr is considered, a reduction in the particle diameter from 0.006 m (i.e., SP-564) to 0.00205 m (i.e., MSC-544) causes an increase in the pressure drop from 0.054 to 0.276 KPa which represents 411% increase in the pressure drop. While if a flowrate of 31.6 m^3/hr is considered, the pressure drop increases from 0.072 to 0.355 KPa (393% increases). At a flowrate of 38 m^3/hr under the same conditions, the pressure drop increases from 0.103 to 0.445 KPa (i.e., 332% increase in ΔP).

Therefore, it can be deduced that the effect of decreasing the particle diameter on the pressure drop is more significant than the effect of increasing the flowrate. Figure 4.10 represents the effect of changing the particle diameter on the pressure drop.
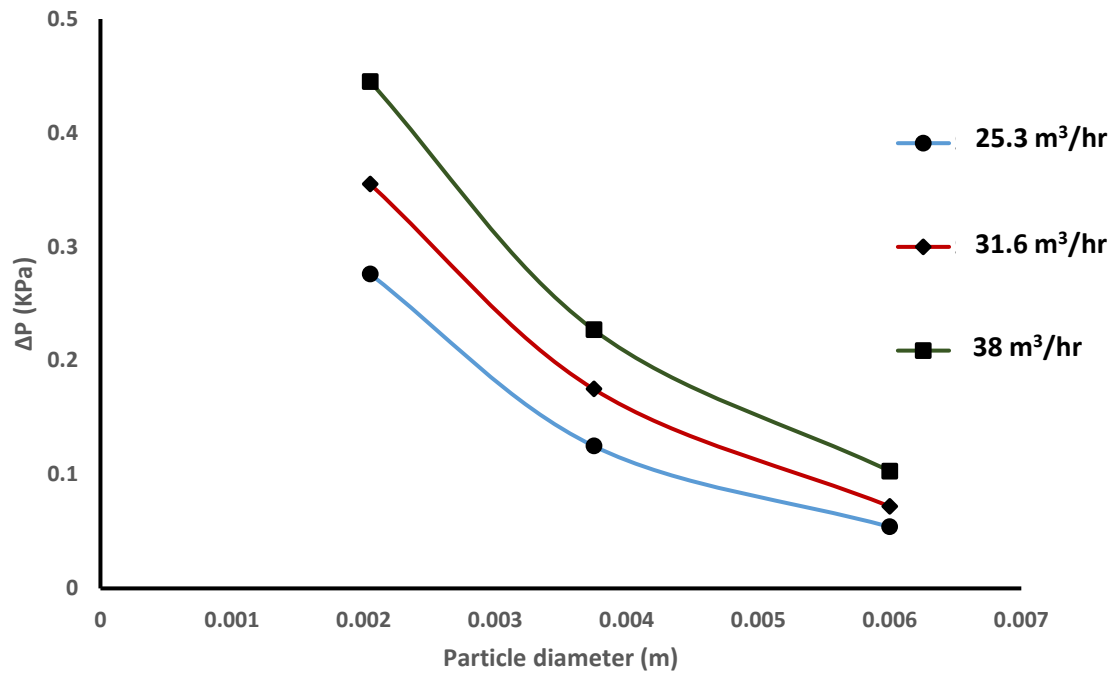
Figure 4.10 Effect of the particle diameter on the pressure drop

5   Conclusion and future work

The objective from this chapter is to sum up the observations concluded from the results of the previous chapter to identify the most effective parameters that could be applied for optimizing the adsorption process of CO_2 on zeolite 13X. In addition, some recommendations, and proposals to be implemented in the future will be emphasized for enhancing the efficiency of the adsorption process.

5.1   Conclusion

Varying the flowrate has two competing effects on the adsorption process. Increasing the flowrate reduces the breakthrough time and saturation occurs faster due to high diffusion. However, that causes a reduction or loss in the adsorption capacity of the adsorbent due to insufficient contact time between the adsorbate/adsorbent, which consequently reduces the bed efficiency, due to wider mass transfer zone and increased portion of the unused bed length. It was observed that the breakthrough time reduces significantly with increasing the flowrate, associated with slight decrease in the adsorption capacity. For instance, increasing the flowrate from 25.3 to 38 m^3/hr for MSC-544 lowers the breakthrough time from 11.6 to 7.6 hrs and reduces the adsorption capacity from 31.5 to 29.2 (g CO_2/Kg adsorbent). This implies a slight reduction in the bed efficiency from 87.81% to 83.15%. Therefore, it can be deduced that the advantage of saving the adsorption time was more significant than disadvantage of the slight reduction in the capacity and the efficiency. However, higher flowrates have higher pressure drop. The same behavior was observed for both of MSC-542 and SP-564. So, higher flowrates (i.e., 38 m^3/hr) seems to be a better choice for optimizing the bed capacity and saving the adsorption cycle time (i.e., high uptake rate), without considering the effect of the increased pressure drop at higher flowrates.

On the other hand, the effect of the particle diameter was of more significance on the adsorption capacity and the bed efficiency. Decreasing the particle diameter causes increase in the adsorption capacity and the bed efficiency, as the surface area and the number of the adsorbent sites increase with decreasing the particle diameter. The column efficiency was enhanced from 65.54% to 83.15% at flowrate 38 m^3/hr by decreasing the particle diameter from 0.006 m (i.e., SP-564) to 0.00205 m (i.e., MSC-544). In that case the width of the mass transfer zone decreased almost by 60% from 0.146 m to 0.059 m.

Varying the flowrate during the same experimental run was studied and seemed to be highly effective if the decision is made to carry out the adsorption process at lower flowrates. In this manner, the relatively higher adsorption capacities at the lower flowrates (i.e., 31.6 and 25.3 m^3/hr) are reached in shorter time.

Thomas model was very commensurate for predicting the adsorption capacity and the shape of the breakthrough curve by nonlinear regression analysis. The high goodness of fitting for the experimental data with Thomas model is a verification that the adsorption of CO_2 on zeolite13X follows the Langmuir kinetics, since Thomas model is based on the Langmuir assumptions.

Accurate estimation of the void fraction is crucial for predicting the pressure drop precisely. Moreover, it was concluded that as the void fraction value increases, the sensitivity of the predicted ΔP to variations in (ε) value increases, and the percentage of error between the measured and the predicted ΔP values becomes higher. Increasing the flowrate leads to higher ΔP, due to increase in the drag forces and inertial effects. Also, decreasing the particle diameter arises to increase in the pressure drop, as the surface area increases, and consequently the resistance to fluid flow increases. The effect of decreasing the particle diameter on the pressure drop had more influence than increasing the flowrate.

In light of the above, the adsorption of CO_2 on zeolites 13X seems to be complicated and dependent on various parameters. Therefore, optimization between the bed capacity, adsorption time, and the pressure drop should be implemented thoroughly, for enhancing the efficiency of the process, based on the required outputs determined by the decision makers.

5.2   Recommendations for future work

It is recommended to study the effect of temperature on the adsorption capacity and the breakthrough behavior. As the adsorption capacity is enhanced by lowering the temperature due to the exothermic nature of the adsorption process. Hence, it will be of great importance to perform a comparison between the effect of varying the temperature and the effect of varying the flowrate on the adsorption capacity and the efficiency of the column, in order to investigate which effect is of more significance for enhancing the process. However, that requires an appropriate insulation system around the piping and the columns, in order to maintain the temperature of the air stream at the desired temperatures. It should be mentioned that the lack of good insulation was the main problem during the experimental work, that hindered investigating the temperature effect on the process.

The simultaneous adsorption of water vapor with CO_2 is one of the common operational problems of adsorption processes of vapor from air on zeolites. That causes a reduction in the adsorption capacity of the zeolites, owing to their high selectivity towards the water vapor as well as the CO_2 [125]. Therefore, it is highly recommended to study that effect of relative humidity on the bed capacity. By plotting the relative humidity at different values versus the adsorption capacity, a correction factor for the reduction in capacity with increasing the relative humidity could be obtained, which might be effective in predicting the variations in the bed capacity due to variations in the relative humidity of air.

Adsorption isotherm of CO_2 on zeolite 13X shall be reported and implemented by changing the initial concentration of CO_2. That could be done by mixing the air with pure CO_2 and adjusting the concentration required by means of mass flow controller. Then the experimental data obtained should be compared with one of the well-known adsorption isotherms, to check the validity of the obtained experimental data. Toth isotherm is highly recommended in predicting and describing the adsorption of CO_2 onto zeolites.

Significant reduction in the energy consumption of CO_2 capture system always remains the main challenge which essentially controls the profitability and the overall efficiency of the project. The source and the type of energy utilized will play an important role for the estimation of the overall operating cost. Therefore, it might be of great importance to consider using the desorbed CO_2 product itself as the regeneration purge gas. This consequently reduces the electrical energy consumption of the electric heaters for heating the air used for regeneration. In addition, this ensures that the obtained CO_2 purity at the given operating conditions of adsorption/desorption process is maintained constant [82].

Bibliography

1. Houghton, J.J.R.o.P.i.P., *Global warming*. 2005. **68**(6): p. 1343.
2. Knutti, R. and G.C.J.N.G. Hegerl, *The equilibrium sensitivity of the Earth's temperature to radiation changes*. 2008. **1**(11): p. 735-743.
3. Kweku, D.W., et al., *Greenhouse effect: greenhouse gases and their impact on global warming*. 2017: p. 1-9.
4. Anderson, T.R., E. Hawkins, and P.D.J.E. Jones, *CO2, the greenhouse effect and global warming: from the pioneering work of Arrhenius and Callendar to today's Earth System Models*. 2016. **40**(3): p. 178-187.
5. Shahbazi, A. and B.R.J.J.P.E.B. Nasab, *Carbon capture and storage (CCS) and its impacts on climate change and global warming*. 2016. **7**(9).
6. Edenhofer, O., *Climate change 2014: mitigation of climate change*. Vol. 3. 2015: Cambridge University Press.
7. Fischedick, M., et al., *Industry*. 2014.
8. Giri, A., D.J.R.m.i.m.s. Pant, and m.e.E.h.d. org/10./b978-0-12-803581-8.11041-0, *Carbon management and greenhouse gas mitigation*. 2018.
9. Boot-Handford, M.E., et al., *Carbon capture and storage update*. 2014. **7**(1): p. 130-189.
10. Baena-Moreno, F.M., et al., *Carbon capture and utilization technologies: a literature review and recent advances*. 2019. **41**(12): p. 1403-1433.
11. Berge, U., et al., *Carbon capture and storage*. Zero Emission Resource Organization. Retrieved from https://zero. no/wp ….
12. Leung, D.Y., et al., *An overview of current status of carbon dioxide capture and storage technologies*. 2014. **39**: p. 426-443.
13. Chao, C., et al., *Post-combustion carbon capture*. 2020: p. 110490.
14. De Visser, E., et al., *Dynamis CO2 quality recommendations*. 2008. **2**(4): p. 478-484.
15. Olajire, A.A.J.E., *CO2 capture and separation technologies for end-of-pipe applications–a review*. 2010. **35**(6): p. 2610-2628.
16. Cuéllar-Franca, R.M. and A.J.J.o.C.u. Azapagic, *Carbon capture, storage and utilisation technologies: A critical analysis and comparison of their life cycle environmental impacts*. 2015. **9**: p. 82-102.
17. Buhre, B.J., et al., *Oxy-fuel combustion technology for coal-fired power generation*. 2005. **31**(4): p. 283-307.
18. Pfaff, I. and A.J.E.P. Kather, *Comparative thermodynamic analysis and integration issues of CCS steam power plants based on oxy-combustion with cryogenic or membrane based air separation*. 2009. **1**(1): p. 495-502.
19. Lackner, K., H.-J. Ziock, and P. Grimes, *Carbon dioxide extraction from air: is it an option?* 1999, Los Alamos National Lab., NM (US).
20. Jones, C.W.J.A.r.o.c. and b. engineering, *CO2 capture from dilute gases as a component of modern global carbon management*. 2011. **2**: p. 31-52.
21. Goeppert, A., et al., *Air as the renewable carbon source of the future: an overview of CO 2 capture from the atmosphere*. 2012. **5**(7): p. 7833-7853.
22. Samanta, A., et al., *Post-combustion CO2 capture using solid sorbents: a review*. 2012. **51**(4): p. 1438-1463.
23. Choi, S., et al., *Adsorbent materials for carbon dioxide capture from large anthropogenic point sources*. 2009. **2**(9): p. 796-854.

24. Hornbostel, M.D., et al., *Characteristics of an advanced carbon sorbent for CO2 capture.* 2013. **56**: p. 77-85.

25. Nugent, P., et al., *Porous materials with optimal adsorption thermodynamics and kinetics for CO 2 separation.* 2013. **495**(7439): p. 80-84.

26. Grajciar, L., et al., *Controlling the adsorption enthalpy of CO2 in zeolites by framework topology and composition.* 2012. **5**(10): p. 2011-2022.

27. Sayari, A., Y. Belmabkhout, and R.J.C.E.J. Serna-Guerrero, *Flue gas treatment via CO2 adsorption.* 2011. **171**(3): p. 760-774.

28. Dong, X., et al., *Effect of water vapor from power station flue gas on CO2 capture by vacuum swing adsorption with activated carbon.* 2011. **39**(3): p. 169-174.

29. Krungleviciute, V., et al., *Kinetics and equilibrium of gas adsorption on RPM1‐Co and Cu‐BTC metal‐organic frameworks: Potential for gas separation applications.* 2008. **54**(4): p. 918-923.

30. Sjostrom, S. and H.J.F. Krutka, *Evaluation of solid sorbents as a retrofit technology for CO2 capture.* 2010. **89**(6): p. 1298-1306.

31. Socolow, R., et al., *Direct air capture of CO2 with chemicals: a technology assessment for the APS Panel on Public Affairs.* 2011, American Physical Society.

32. Choi, S., et al., *Application of amine-tethered solid sorbents for direct CO2 capture from the ambient air.* 2011. **45**(6): p. 2420-2427.

33. Goeppert, A., et al., *Easily regenerable solid adsorbents based on polyamines for carbon dioxide capture from the air.* 2014. **7**(5): p. 1386-1397.

34. Belmabkhout, Y., V. Guillerm, and M.J.C.E.J. Eddaoudi, *Low concentration CO2 capture using physical adsorbents: Are metal–organic frameworks becoming the new benchmark materials?* 2016. **296**: p. 386-397.

35. Yu, C.-H., et al., *A review of CO2 capture by absorption and adsorption.* 2012. **12**(5): p. 745-769.

36. Ruthven, D.M., *Principles of adsorption and adsorption processes.* 1984: John Wiley & Sons.

37. Plaza, M.G., et al., *Different approaches for the development of low-cost CO 2 adsorbents.* 2009. **135**(6): p. 426-432.

38. Kumar, A., et al., *Direct air capture of CO2 by physisorbent materials.* 2015. **54**(48): p. 14372-14377.

39. Wang, Q., et al., *CO2 capture by solid adsorbents and their applications: current status and new trends.* 2011. **4**(1): p. 42-55.

40. Zhao, D., et al., *Characteristics of the synthetic heulandite-clinoptilolite family of zeolites.* 1998. **21**(4-6): p. 371-379.

41. Jacobs, P.A., et al., *Surface probing of synthetic faujasites by adsorption of carbon dioxide. Part 1.—Infra-red study of carbon dioxide adsorbed on Na-Ca-Y and Na-Mg-Y zeolites.* 1973. **69**: p. 1056-1068.

42. Miliani, C., et al., *CO2 entrapment in natural ultramarine blue.* 2008. **466**(4-6): p. 148-151.

43. Hernández-Huesca, R., et al., *Adsorption equilibria and kinetics of CO2, CH4 and N2 in natural zeolites.* 1999. **15**(2): p. 163-173.

44. Xiao, P., et al., *Capture of CO 2 from flue gas streams with zeolite 13X by vacuum-pressure swing adsorption.* 2008. **14**(4): p. 575-582.

45. Liu, Y., et al., *Effect of functionalized linker on CO2 binding in zeolitic imidazolate frameworks: density functional theory study.* 2012. **116**(32): p. 16985-16991.

46. Bonelli, B., et al., *Experimental and quantum chemical studies on the adsorption of carbon dioxide on alkali-metal-exchanged ZSM-5 zeolites.* 2000. **104**(47): p. 10978-10988.

47. Lee, C.H., et al., *Effects of pore structure and PEI impregnation on carbon dioxide adsorption by ZSM-5 zeolites.* 2015. **23**: p. 251-256.

48. Kongnoo, A., et al., *Surface characteristics and CO2 adsorption capacities of acid-activated zeolite 13X prepared from palm oil mill fly ash.* 2017. **193**: p. 385-394.

49. Herawan, S., et al., *Characterization of activated carbons from oil-palm shell by CO2 activation with no holding carbonization temperature.* 2013. **2013**.

50. McDougall, G.J.J.o.t.S.A.I.o.M. and Metallurgy, *The physical nature and manufacture of activated carbon.* 1991. **91**(4): p. 109-120.

51. Rashidi, N.A. and S.J.J.o.C.u. Yusup, *An overview of activated carbons utilization for the post-combustion carbon dioxide capture.* 2016. **13**: p. 1-16.

52. Do, D.D., *Adsorption Analysis: Equilibria and Kinetics (With CD Containing Computer Matlab Programs).* Vol. 2. 1998: World Scientific.

53. Brandani, F., D.M.J.I. Ruthven, and e.c. research, *The effect of water on the adsorption of CO2 and C3H8 on type X zeolites.* 2004. **43**(26): p. 8339-8344.

54. Sultan, M., et al., *An overview of solid desiccant dehumidification and air conditioning systems.* 2015. **46**: p. 16-29.

55. Srivastava, N. and I.J.A.t.e. Eames, *A review of adsorbents and adsorbates in solid–vapour adsorption heat pump systems.* 1998. **18**(9-10): p. 707-714.

56. Suzuki, M. and M. Suzuki, *Adsorption engineering.* Vol. 14. 1990: Kodansha Tokyo.

57. Jia, C., et al., *Experimental comparison of two honeycombed desiccant wheels fabricated with silica gel and composite desiccant material.* 2006. **47**(15-16): p. 2523-2534.

58. Ponec, V., Z. Knor, and S. Cerny, *Adsorption on solids.* 2018: Butterworth.

59. Harker, J., J. Backhurst, and J. Richardson, *Chemical Engineering Volume 2.* Vol. 2. 2013: Elsevier.

60. McCabe, W.L., J.C. Smith, and P. Harriott, *Unit operations of chemical engineering.* Vol. 5. 1993: McGraw-hill New York.

61. Tarafder, A., A. Bonilla-Petrociolet, and G.J.M.-O.O.i.C.E. Rangaiah, *Modeling and multi-objective optimization of a chromatographic system.* 2013: p. 369-398.

62. Fahien, R.W. and J.J.A.j. Smith, *Mass transfer in packed beds.* 1955. **1**(1): p. 28-37.

63. Lukchis, G.M. and L. GM, *ADSORPTION SYSTEMS. I. DESIGN BY MASS-TRANSFER ZONE CONCEPT.* 1973.

64. Gabelman, A.J.C.E.P., *Adsorption basics: part 1.* 2017. **113**(7): p. 48-53.

65. Geankoplis, C.J., *Transport processes and separation process principles:(includes unit operations).* 2003: Prentice Hall Professional Technical Reference.

66. Seader, J.D., E.J. Henley, and D.K. Roper, *Separation process principles.* Vol. 25. 1998: wiley New York.

67. Adamson, A.W. and A.P. Gast, *Physical chemistry of surfaces.* Vol. 15. 1967: Interscience publishers New York.

68. Yang, R.T., *Gas separation by adsorption processes.* Vol. 1. 1997: World Scientific.

69. Langmuir, I.J.J.o.t.A.c.s., *The constitution and fundamental properties of solids and liquids. Part I. Solids.* 1916. **38**(11): p. 2221-2295.

70. Langmuir, I.J.P.R., *The evaporation, condensation and reflection of molecules and the mechanism of adsorption.* 1916. **8**(2): p. 149.

71. Langmuir, I.J.J.o.t.A.C.s., *The adsorption of gases on plane surfaces of glass, mica and platinum.* 1918. **40**(9): p. 1361-1403.

72.   Swenson, H. and N.P.J.L. Stadie, *Langmuir's theory of adsorption: A centennial review.* 2019. **35**(16): p. 5409-5426.

73.   Kumar, K.V., et al., *A site energy distribution function from Toth isotherm for adsorption of gases on heterogeneous surfaces.* 2011. **13**(13): p. 5753-5759.

74.   Tóth, J.J.A.i.C. and I. Science, *Uniform interpretation of gas/solid adsorption.* 1995. **55**: p. 1-239.

75.   Wang, Y., M.D.J.J.o.C. LeVan, and E. Data, *Adsorption equilibrium of carbon dioxide and water vapor on zeolites 5A and 13X and silica gel: pure components.* 2009. **54**(10): p. 2839-2844.

76.   Tun, H. and C.-C.J.A. Chen, *Isosteric heat of adsorption from thermodynamic Langmuir isotherm.* 2021: p. 1-11.

77.   Sundaram, N., R.T.J.J.o.c. Yang, and i. science, *Isosteric heats of adsorption from gas mixtures.* 1998. **198**(2): p. 378-388.

78.   Dunne, J., et al., *Calorimetric heats of adsorption and adsorption isotherms. 1. O2, N2, Ar, CO2, CH4, C2H6, and SF6 on silicalite.* 1996. **12**(24): p. 5888-5895.

79.   Shen, D., et al., *Comparison of experimental techniques for measuring isosteric heat of adsorption.* 2000. **6**(4): p. 275-286.

80.   Builes, S., S.I. Sandler, and R.J.L. Xiong, *Isosteric heats of gas and liquid adsorption.* 2013. **29**(33): p. 10416-10422.

81.   Pan, H., J.A. Ritter, and P.B.J.L. Balbuena, *Examination of the approximations used in determining the isosteric heat of adsorption from the Clausius-Clapeyron equation.* 1998. **14**(21): p. 6323-6327.

82.   Ntiamoah, A., et al., *CO2 capture by temperature swing adsorption: use of hot CO2-rich gas for regeneration.* 2016. **55**(3): p. 703-713.

83.   Broom, D.J.C.E.P., *Characterizing adsorbents for gas separations.* 2018. **114**: p. 30-37.

84.   Tlili, N., G. Grévillot, and C.J.I.J.o.G.G.C. Vallières, *Carbon dioxide capture and recovery by means of TSA and/or VSA.* 2009. **3**(5): p. 519-527.

85.   Wang, L., et al., *Experimental and modeling investigation on post-combustion carbon dioxide capture using zeolite 13X-APG by hybrid VTSA process.* 2012. **197**: p. 151-161.

86.   Merel, J., et al., *Experimental investigation on CO2 post− combustion capture by indirect thermal swing adsorption using 13X and 5A zeolites.* 2008. **47**(1): p. 209-215.

87.   Kikkinides, E.S., et al., *Concentration and recovery of carbon dioxide from flue gas by pressure swing adsorption.* 1993. **32**(11): p. 2714-2720.

88.   Chue, K., et al., *Comparison of activated carbon and zeolite 13X for CO2 recovery from flue gas by pressure swing adsorption.* 1995. **34**(2): p. 591-598.

89.   Choi, W.-K., et al., *Optimal operation of the pressure swing adsorption (PSA) process for CO 2 recovery.* 2003. **20**(4): p. 617-623.

90.   Ko, D., et al., *Optimization of pressure swing adsorption and fractionated vacuum pressure swing adsorption processes for CO2 capture.* 2005. **44**(21): p. 8084-8094.

91.   Zhang, J., et al., *Effect of process parameters on power requirements of vacuum swing adsorption technology for CO2 capture from flue gas.* 2008. **49**(2): p. 346-356.

92.   Achenbach, E.J.E.t. and f. science, *Heat and flow characteristics of packed beds.* 1995. **10**(1): p. 17-27.

93.   Kruczek, B.J.E.o.m., *Carman–kozeny equation.* 2014: p. 1-3.

94.   Chilton, T.H., A.P.J.I. Colburn, and E. Chemistry, *II—pressure drop in packed tubes1.* 1931. **23**(8): p. 913-919.

95.   Ergun, S.J.C.E.P., *Fluid flow through packed columns.* 1952. **48**: p. 89-94.

96.   Nemec, D. and J.J.C.E.S. Levec, *Flow through packed bed reactors: 1. Single-phase flow.* 2005. **60**(24): p. 6947-6957.

97.   Niven, R.K.J.C.E.S., *Physical insight into the Ergun and Wen & Yu equations for fluid flow in packed and fluidised beds.* 2002. **57**(3): p. 527-534.

98.   Leva, M.J.C.E.P., *Pressure drop through packed tubes. III. Prediction of voids in packed tubes.* 1947. **43**: p. 713-718.

99.   Ouchiyama, N., T.J.I. Tanaka, and e.c. fundamentals, *Porosity estimation for random packings of spherical particles.* 1984. **23**(4): p. 490-493.

100.   Benenati, R. and C.J.A.J. Brosilow, *Void fraction distribution in beds of spheres.* 1962. **8**(3): p. 359-361.

101.   Goodling, J., et al., *Radial porosity distribution in cylindrical beds packed with spheres.* 1983. **35**(1): p. 23-29.

102.   Daszkowski, T. and S.-u.W. Str6mung, *irmetransport in schiittungsgefiillten Rohrreaktoren.* 1991, Dissertation, Techn. Univ. Stuttgart.

103.   Ziółkowska, I., D.J.C.E. Ziółkowski, and P.P. Intensification, *Fluid flow inside packed beds.* 1988. **23**(3): p. 137-164.

104.   Carman, P.C.J.T.I.C.E., *Fluid flow through granular beds.* 1937. **15**: p. 150-166.

105.   Couper, J.R., et al., *Chemical process equipment: selection and design.* 2005: Gulf Professional Publishing.

106.   Bahadori, A., *essentials of Oil and Gas utilities: Process Design, equipment, and Operations.* 2016: Gulf Professional Publishing.

107.   Al-Janabi, N., et al., *Velocity variation effect in fixed bed columns: A case study of CO2 capture using porous solid adsorbents.* 2018. **64**(6): p. 2189-2197.

108.   Mesfer, M.K.A., et al., *Continuous Fixed Bed CO2 Adsorption: Breakthrough, Column Efficiency, Mass Transfer Zone.* 2020. **8**(10): p. 1233.

109.   Chu, K.H.J.J.o.H.M., *Fixed bed sorption: setting the record straight on the Bohart–Adams and Thomas models.* 2010. **177**(1-3): p. 1006-1012.

110.   Thomas, H.C.J.A.o.t.N.Y.A.o.S., *Chromatography: a problem in kinetics.* 1948. **49**(2): p. 161-182.

111.   Goel, J., et al., *Removal of lead (II) by adsorption using treated granular activated carbon: batch and column studies.* 2005. **125**(1-3): p. 211-220.

112.   Han, R., et al., *Copper (II) and lead (II) removal from aqueous solution in fixed-bed columns by manganese oxide coated zeolite.* 2006. **137**(2): p. 934-942.

113.   Aksu, Z. and F.J.P.b. Gönen, *Biosorption of phenol by immobilized activated sludge in a continuous packed bed: prediction of breakthrough curves.* 2004. **39**(5): p. 599-613.

114.   Negrea, A., et al., *Estimation on Fixed-Bed Column Parameters of Breakthrough Behaviors for Gold Recovery by Adsorption onto Modified/Functionalized Amberlite XAD7.* 2020. **17**(18): p. 6868.

115.   Lazaridis, N., T. Karapantsios, and D.J.W.R. Georgantas, *Kinetic analysis for the removal of a reactive dye from aqueous solution onto hydrotalcite by adsorption.* 2003. **37**(12): p. 3023-3033.

116.   Leyva-Ramos, R., et al., *Adsorption of cadmium (II) from aqueous solution on natural and oxidized corncob.* 2005. **45**(1): p. 41-49.

117.   Aksu, Z. and İ.A.J.P.b. İşoğlu, *Removal of copper (II) ions from aqueous solution by biosorption onto agricultural waste sugar beet pulp.* 2005. **40**(9): p. 3031-3044.

118.   Kundu, S. and A.J.C.E.J. Gupta, *Arsenic adsorption onto iron oxide-coated cement (IOCC): regression analysis of equilibrium data with several isotherm models and their optimization.* 2006. **122**(1-2): p. 93-106.

119.   López-Cervantes, J., et al., *Study of a fixed-bed column in the adsorption of an azo dye from an aqueous medium using a chitosan–glutaraldehyde biosorbent.* 2018. **36**(1-2): p. 215-232.

120.   Ahmad, A. and B.J.J.o.h.m. Hameed, *Fixed-bed adsorption of reactive azo dye onto granular activated carbon prepared from waste.* 2010. **175**(1-3): p. 298-303.

121.   Han, R., et al., *Study of equilibrium, kinetic and thermodynamic parameters about methylene blue adsorption onto natural zeolite.* 2009. **145**(3): p. 496-504.

122.   Han, R., et al., *Comparison of linear and nonlinear analysis in estimating the Thomas model parameters for methylene blue adsorption onto natural zeolite in fixed-bed column.* 2007. **145**(1-2): p. 331-335.

123.   Ludwig, E.E., *Applied Process Design for Chemical and Petrochemical Plants: Volume 2.* Vol. 2. 1997: Gulf Professional Publishing.

124.   Scheidegger, A.E., *The physics of flow through porous media.* 2020: University of Toronto press.

125.   Li, G., et al., *Competition of CO2/H2O in adsorption based CO2 capture.* 2009. **1**(1): p. 1123-1130.